STATE OF THE CLIMATE
IN 2010

J. Blunden, D. S. Arndt, and M. O. Baringer, Eds.

Associate Eds. K. M. Willett, A. J. Dolman, B. D. Hall, P. W. Thorne, J. M. Levy, H. J. Diamond,
J. Richter-Menge, M. Jeffries, R. L. Fogt, L. A. Vincent, and J. M. Renwick

Special Supplement to the
Bulletin of the American Meteorological Society
Vol. 92, No. 6, June 2011

2. GLOBAL CLIMATE—K. M. Willett, A. J. Dolman, B. D. Hall, and P. W. Thorne, Eds.

a. Introduction—P. W. Thorne

The year 2010 was among the two warmest years globally since the start of the surface instrumental record in the late 19th century, although the range makes it impossible to call the ranking definitively. It was also the second warmest year in tropospheric records since the mid-20th century. Glaciers very likely experienced the 20th consecutive year of negative mass balance. The hydrological cycle experienced many extremes and global land precipitation was anomalously high. Greenhouse gases continued to increase and ozone depleting substances continued to decrease. The stratosphere continued to be anomalously cold. This chapter describes these and other indicators of ongoing changes in the Earth's climate system including atmospheric composition and terrestrial and cryospheric variables.

Climate is not just about decadal-scale externally forced variability, thus substantial attention is given to the major modes of natural variability (see Sidebar 1.1 for a general overview). Globally, 2010 was dominated by two modes of natural climate variability–the El Niño-Southern Oscillation (ENSO) and the Arctic Oscillation (AO). ENSO transitioned from a strong El Niño in early 2010 to a moderate-to-strong La Niña by the end of the year. Global temperatures typically lag ENSO by a few months, thus the warm El Niño phase had the larger impact upon 2010 temperatures. The AO reached its most negative value on record over the winter of 2009/10 and was negative again in the early winter of 2010/11. This led to extreme cold winter conditions and snow cover through much of the Northern Hemisphere midlatitudes and above-normal winter temperatures in the high northern latitudes.
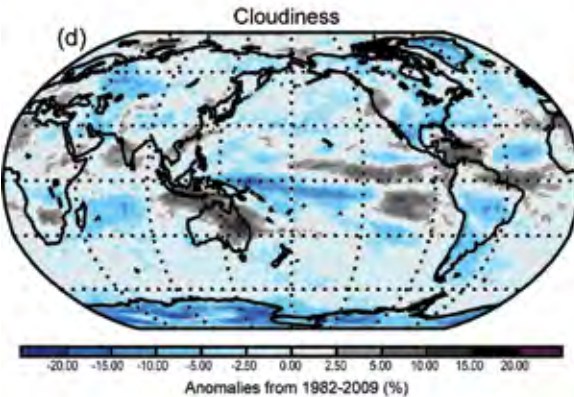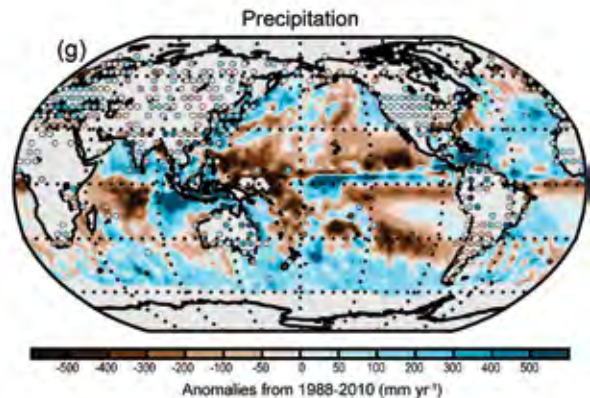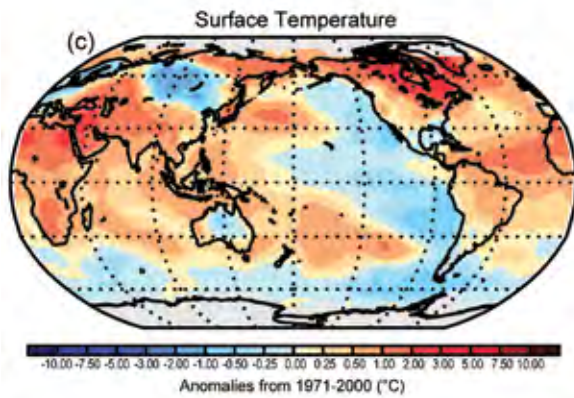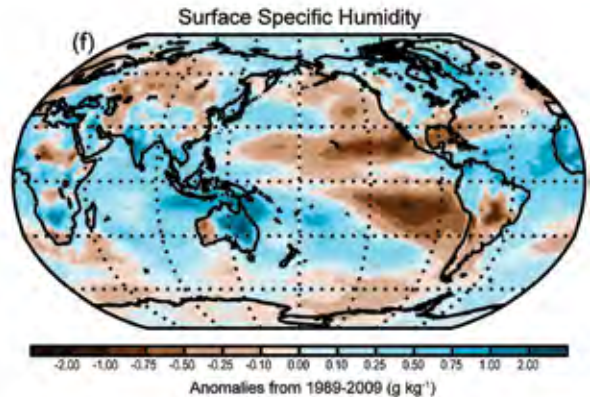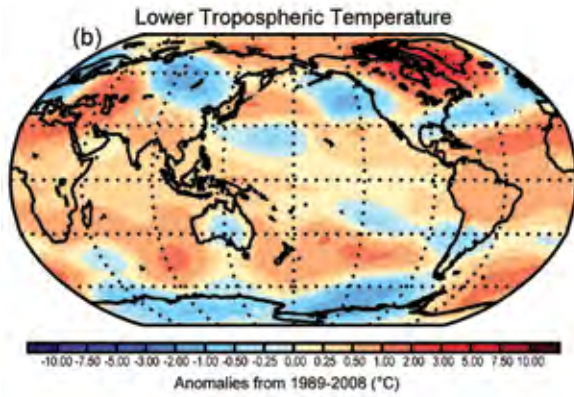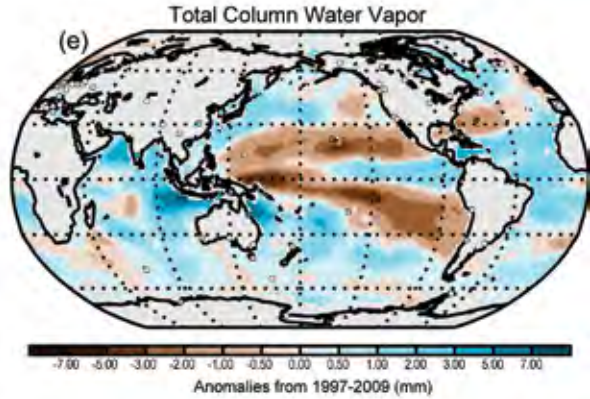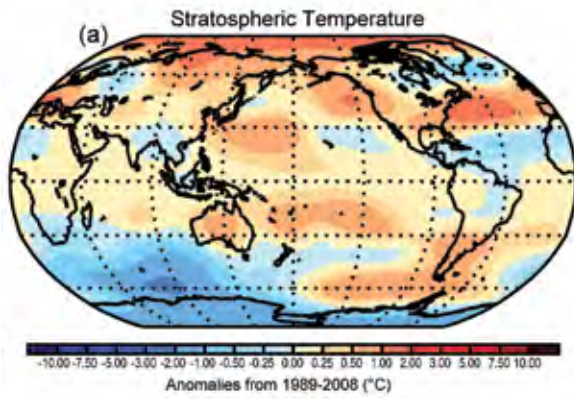
A number of new variables are included in this year's report. There is a renewed focus on composition changes and changes in terrestrial variables, providing a greater reach into these areas than ever before. As discussed below, global lake temperatures have increased since 1985 and show similar spatiotemporal evolution to available land surface records. Global groundwater fluctuations show a combination of climate effects and direct human influences. Biomass inventories show general decreases in the tropics and increases in midlatitudes, reflecting deforestation and afforestation, respectively. However, these are uncertain and may have country-specific errors. The reader will find many further new insights into ongoing changes in the Earth and its climate.

Several issues of general interest are highlighted in sidebars within the chapter to illustrate both the complexities of global climate monitoring and the opportunities that new technologies and approaches afford the community. Building upon the introduction of ERA reanalyses last year, several alternative reanalysis products are included for temperature, humidity, wind speed, and global aerosols. Reanalysis products are also used to estimate global river discharge patterns. To aid interpretation, Sidebar 2.1 provides a high-level exposition of reanalyses outlining recent developments along with potential caveats. This is the first time that many of these products have been shown together with more traditional climate datasets, enabling simple broad-brush comparisons. Satellite data from GRACE satellites are shown to be hugely important for characterizing changes in ice sheet mass balance, groundwater, and deep ocean mass. Land surface winds are immensely challenging to analyze for long-term behavior but indicate likely weakening ('stilling') over time. Stratospheric water vapor is very important for radiative balance, with effects potentially felt at the surface, but it is extremely challenging to monitor and several mysteries remain regarding both mechanisms and trends.
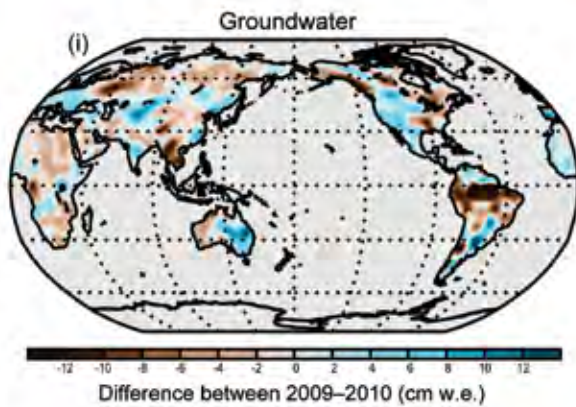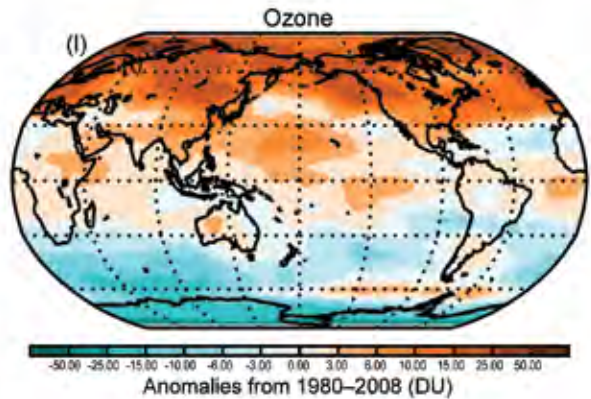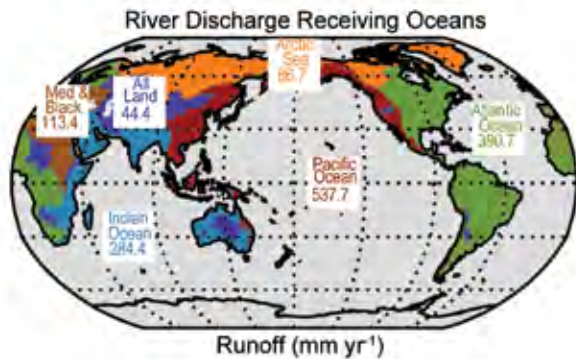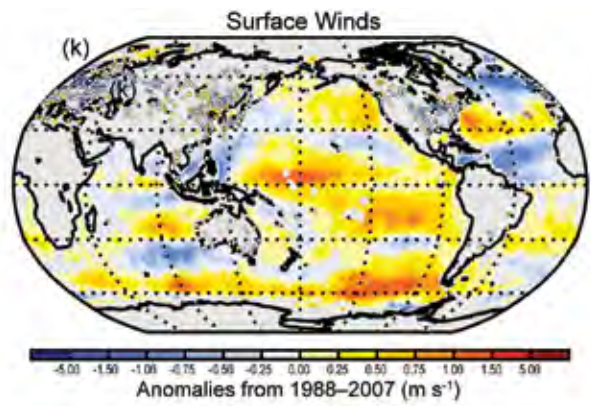
Publicly available datasets used in this chapter are detailed in Table 2.1. Anomalies for 2010 for all those variables that could be calculated are given in Plate 2.1 and all available time series compiled into Plate 2.2, allowing ease of comparison.

PLATE 2.1. Global annual anomaly maps for those variables for which it is possible to create a meaningful 2010 anomaly estimate. Reference base periods differ among variables, but spatial patterns should largely dominate over choices of base period. Dataset sources/names are as follows: lower stratospheric temperature (ERA-Interim); lower tropospheric temperature (ERA-Interim); surface temperature (NOAA/NCDC); cloudiness (PATMOS-x); total column water vapor (AMSR-E over ocean, ground-based GPS over land); surface specific humidity (ERA-Interim); precipitation (RSS over ocean, GHCN (gridded) over land); groundwater 2010–2009 differences (the sum of groundwater, soil water, surface water, snow, and ice, as an equivalent height of water in cm) (GRACE); river discharge absolute values (authors); mean sea level pressure (HadSLP2r); surface wind speed (AMSR-E over ocean, authors in situ over land); ozone (SBUVs/OMI/TOMS/GOME1/SCIAMACHY/GOME2, base period data from the multi-sensor reanalysis, MSR); FAPAR [SeaWiFS (NASA) and MERIS (ESA) sensors]; biomass burning (GFAS). See relevant section text and figures for more details.

(a) Stratospheric Temperature
Anomalies from 1989-2008 (°C)
-10.00 -7.50 -5.00 -3.00 -2.00 -1.00 -0.50 -0.25 0.00 0.25 0.50 1.00 2.00 3.00 5.00 7.50 10.00

(b) Lower Tropospheric Temperature
Anomalies from 1989-2008 (°C)
-10.00 -7.50 -5.00 -3.00 -2.00 -1.00 -0.50 -0.25 0.00 0.25 0.50 1.00 2.00 3.00 5.00 7.50 10.00

(c) Surface Temperature
Anomalies from 1971-2000 (°C)
-10.00 -7.50 -5.00 -3.00 -2.00 -1.00 -0.50 -0.25 0.00 0.25 0.50 1.00 2.00 3.00 5.00 7.50 10.00

(d) Cloudiness
Anomalies from 1982-2009 (%)
-20.00 -15.00 -10.00 -5.00 -2.50 0.00 2.50 5.00 10.00 15.00 20.00

(e) Total Column Water Vapor
Anomalies from 1997-2009 (mm)
-7.00 -5.00 -3.00 -2.00 -1.00 -0.50 0.00 0.50 1.00 2.00 3.00 5.00 7.00

(f) Surface Specific Humidity
Anomalies from 1989-2009 (g kg^{-1})
-2.00 -1.00 -0.75 -0.50 -0.25 -0.10 0.00 0.10 0.25 0.50 0.75 1.00 2.00

(g) Precipitation
Anomalies from 1988-2010 (mm yr^{-1})
-500 -400 -300 -200 -100 -50 0 50 100 200 300 400 500

River Discharge Continent Runoff

(h)

Europe
218.7

Asia
265.4

North
America
215.0

Africa
160.8

Austra-
lasia
332.2

South
America
628.5

River Discharge Receiving Oceans

Arctic
Sea
86.7

Med &
Black
113.4

All
Land
44.4

Atlantic
Ocean
390.7

Pacific
Ocean
537.7

Indian
Ocean
284.4

Runoff (mm yr^{-1})

Groundwater

(i)

-12 -10 -8 -6 -4 -2 0 2 4 6 8 10 12

Difference between 2009–2010 (cm w.e.)

Sea Level Pressure

(j)

-15.00 -10.00 -7.50 -5.00 -2.50 -1.00 0.00 1.00 2.50 5.00 7.50 10.00 15.00

Anomalies from 1961–1990 (hPa)

Surface Winds

(k)

-5.00 -1.50 -1.00 -0.75 -0.50 -0.25 0.00 0.25 0.50 0.75 1.00 1.50 5.00

Anomalies from 1988–2007 (m s^{-1})

Ozone

(l)

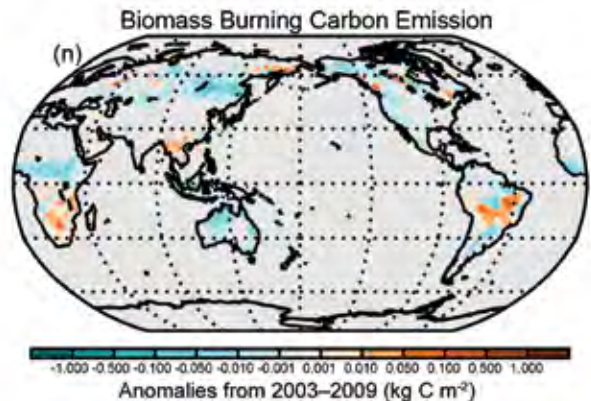-50.00 -25.00 -15.00 -10.00 -6.00 -3.00 0.00 3.00 6.00 10.00 15.00 25.00 50.00

Anomalies from 1980–2008 (DU)

Fraction of Absorbed Photosynthetically Active Radiation

(m)

-0.15 -0.10 -0.05 -0.03 -0.02 -0.01 0.00 0.01 0.02 0.03 0.05 0.10 0.15

Anomalies from 1998–2010 (FAPAR)

Biomass Burning Carbon Emission

(n)

-1.000 -0.500 -0.100 -0.050 -0.010 -0.001 0.001 0.010 0.050 0.100 0.500 1.000

Anomalies from 2003–2009 (kg C m^{-2})
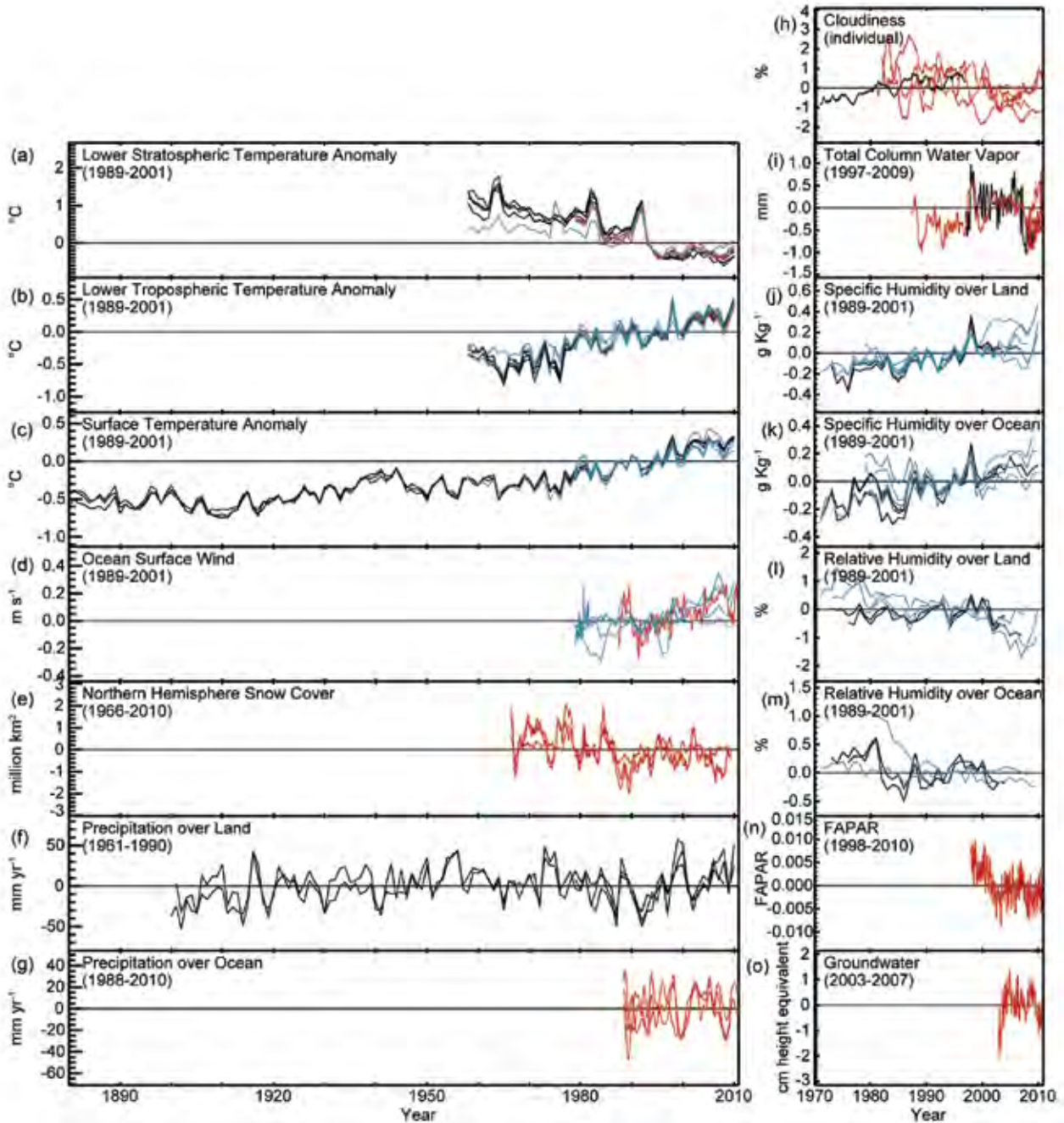
Table 2.1. Sources of those datasets used in this chapter that are publicly available.

Source	Datasets	Section
http://nomads.ncdc.noaa.gov/	NCEP CFSR	Sidebar 2.1, b1, c1, d2
http://gmao.gsfc.nasa.gov/merra/	MERRA	Sidebar 2.1, b1, b2, b3, c1, d2
http://www.esrl.noaa.gov/psd/data/20thC_Rean/	20CR	Sidebar 2.1, b2, b3, c1, d2
http://www.ecmwf.int/research/era	ERA-Interim	Sidebar 2.1, b1, b2, b3, c1, d2, Sidebar 2.3
http://www.ecmwf.int/research/era	ERA-40	Sidebar 2.1, b1, b2, b3, c1, d2, Sidebar 2.3
http://jra.kishou.go.jp/	JRA-25	Sidebar 2.1, b1, b2, c1, d2
Observations – Atmospheric Dynamics		
http://www.metoffice.gov.uk/hadobs	HadCRUT3; HadSLP2r; HadAT2; Had-CRUH	b1, b2, b3, c1, d1
http://www.ncdc.noaa.gov/cmb-faq/anomalies.html	NOAA/NCDC	b1
http://data.giss.nasa.gov/gistemp/	NASA GISS	b1, b4
http://www.ncdc.noaa.gov/oa/climate/ratpac	RATPAC	b2, b3
http://www.univie.ac.at/theoret-met/research	Raobcore 1.4, RICH	b2, b3
http://vortex.nsstc.uah.edu/public/msu/	UAH v5.4	b2, b3
http://www.remss.com	RSS v3.3, SSM/I, AMSR-E, TMI	b2, b3, c2, c3, d2
http://www.star.nesdis.noaa.gov/smcd/emb/mscat/mscat-main.htm	STAR 2.0	b2, b3
http://www.noc.soton.ac.uk/noc_flux/noc2.php, http://dss.ucar.edu/datasets/ds260.3/	NOCS 2.0	c1
by mail to adai@ucar.edu	Dai	c1
http://cosmic-io.cosmic.ucar.edu/cdaac/index.html	COSMIC	c2
http://www.eol.ucar.edu/deployment/field-deployments/field-projects/gpspw	GPS	c2
http://precip.gsfc.nasa.gov	GPCP	c3
http://www.ncdc.noaa.gov/oa/climate/ghcn-monthly/indes.php	GHCN	c3
http://www.esrl.noaa.gov/psd/data/gridded/data.gpcc.html	GPCC	c3
http://www.esrl.noaa.gov/psd	CMAP	c3
http://www.ncdc.noaa.gov/cdr/operationalcdrs.html	PATMOS-X	c5
http://www.ncdc.noaa.gov/HObS/	HIRS	c5
http://ladsweb.nascom.nasa.gov	MODIS	c5
http://eosweb.larc.nasa.gov/PRODOCS/misr/level3/overview.html	MISR	c5, f2
http://www.atmos.washington.edu/~ignatius/CloudMap	SOBS	c5
http://isccp.giss.nasa.gov	ISCCP D2	c5
http://www.ncdc.noaa.gov/oa/climate.isd.index.php?name=isdlite	ISD-LITE	Sidebar 2.3
http://ceres.larc.nasa.gov/sitemap_ceres.php	CERES	e

Terrestrial		
http://largelakes.jpl.nasa.gov/2010-result	Lake Temperature Data	b4
http://climate.rutgers.edu/snowcover	Snow Cover	c4
http://grdc.bafg.de http://www.gtn-h.net	River Discharge	c6
http://nsidc.org/data/g02190.html	Permafrost Data	c7
http://gracetellus.jpl.nasa.gov/relatedSites/ http://www.csr.utexas.edu/grace/science_links.html	GRACE	c 8 Sidebar 2.2
http://www.ipf.tuwien.ac.at/insitu http://gcmd.nasa.gov/records/GCMD_GES_DISC_LPRM_AM-SRE_SOILM2_V001.html	Soil Moisture	c9
http://tethys.eaprs.cse.dmu.ac.uk/RiverLake/shared/main http://www.legos.obs-mip.fr/soa/hydrologie/hydroweb/ http://www.pecad.fas.usda.gov/cropexplorer/global_reservoir/index.cfm	Altimetric Lake Level products	c10
http://gcmd.nasa.gov/records/GCMD_GLWD.html	The Global Lake and Wetland Database	c10
http://www.geo.unizh.ch/wgms/	Glaciers	g1
http://fapar.jrc.ec.europa.eu/	FAPAR	g2
http://www.globalfiredata.org/	Biomass Burning	g3
http://gmes-atmosphere.eu/fire	GFAS/GFED	g3
Atmospheric Composition		
http://www.esrl.noaa.gov/gmd/dv/iadv/	CO_2, CH_4, CO	f1
http://www.cmdl.noaa.gov/odgi/	ODGI	f1
http://www.esrl.noaa.gov/gmd/hats/combined/N2O.html	N_2O	f1
http://www.esrl.noaa.gov/gmd/hats/combined/SF6.html	SF_6	f1
http://www.esrl.noaa.gov/gmd/hats/combined/CFC11.html	CFC-11	f1
http://www.esrl.noaa.gov/gmd/hats/combined/CFC12.html	CFC-12	f1
http://www.esrl.noaa.gov/gmd/aggi/	AGGI	f1
http://agage.eas.gatech.edu/	PFCs	f1
http://www.gmes-atmosphere.eu/data/	Aerosols	f2
http://acdb-ext.gsfc.nasa.gov/Data_services/merged/	SBUV/TOMS/OMI MOD V8 merged ozone dataset	f3
http://www.iup.uni-bremen.de/gome/wfdoas	GOME/SCIAMACHY/ GOMES2 total ozone datasets, GSG merged data	f3
ftp://ftp.tor.ec.gc.ca/Projects-Campaigns/ZonalMeans/	WOUDC groundbased ozone	f3
http://mirador.gsfc.nasa.gov/cgi-bin/mirador/presentNavigation.pl?tree=projectandproject=OMI	OMI total ozone (OMTO3)	f3
http://www.temis.nl/protocols/O3global.html	Multi sensor reanalysis (MSR) of total ozone	f3
http://www.cpc.ncep.noaa.gov/products/precip/CWlink/daily_ao_index/ao.shtml	Arctic Oscillation (AO)	f3
ftp://ftp.cmdl.noaa.gov/ozwv/water_vapor/Boulder_New/	Boulder water vapor balloon	Sidebar 2.4
http://disc.sci.gsfc.nasa.gov/Aura/data-holdings/MLS/index.shtm	MLS data	Sidebar 2.4
http://haloe.gats-inc.com/home/index.php	HALOE data	Sidebar 2.4

PLATE 2.2. Global average anomaly time series for those variables for which it is possible to create a meaningful estimate. Reference base periods differ among variables, even within panels. For comparison, all time series for each variable have been adjusted to have a mean of zero over a common period which is labeled. Dataset types are as follows: lower stratospheric temperature (a; 4 radiosondes - black, 3 satellites - red, 3 reanalyses - blue); lower tropospheric temperature (b; 4 radiosondes - black, 2 satellites - red, 5 reanalyses - blue); sur-face temperature (c; 3 in situ – black, 5 reanalyses - blue); surface wind speed over ocean (d; 1 satellite - red, 6 reanalyses - blue); Northern Hemisphere snow cover (e; 3 satellite regions - red); precipitation over land (f; 3 in situ - black); precipitation over ocean (g; 3 satellites - red); cloudiness (h; 1 in situ – black, 5 satellites - red); total column water vapor (i; 3 satellites - red, 1 GPS - black); surface specific humidity over land (j; 2 in situ - black, 6 reanalyses - blue); surface specific humidity over ocean (k; 3 in situ - black, 3 reanalyses - blue); surface relative humidity over land (l; 2 in situ - black, 5 reanalyses - blue); surface relative humidity over ocean (m; 2 in situ - black, 2 reanalyses - blue);. Fraction of Absorbed Photosynthetically Active Radiation (FAPAR) (n; 1 satellite – red); groundwater (o; 1 satellite – red). See relevant section text and figures for more details including data sources.

Table 2.2. Reanalyses products included in the Global Chapter.		
Reanalyses Product and Reference	**Data Assimilated**	**Variables shown in the Global Chapter**
NCEP CFSR, Saha et al. 2010	Atmospheric data: wind, temperature, humidity from radiosonde / dropsonde /pilot balloons/ profilers / aircraft; Surface pressure, temperature, humidity, wind, from ship/buoy reports; Surface land pressure from SYNOP/METAR; Retrieved ozone from satellites; Retrieved winds and radiances from geostationary satellites, Ocean surface wind from scatterometers; Radiances from temperature and humidity sounders: AIRS, HIRS, MSU, SSU, AMSU-A/B, MHS; Radiances from passive microwave imagers over ocean: SSM/I, AMSR-E; GPSRO bending angles from CHAMP, COSMIC (from 2001); Multi-sensor retrieved snow cover from NOAA/NESDIS (from 2003) Precipitation data: Pentad data set of CPC Merged Analysis of Precipitation and the CPC unified global daily gauge analysis. Ocean data: Temperature profiles from mobile platforms: expendable bathy thermographs and Argo drifting floats; and fixed platforms: TAO, TRITON, PIRATA, RAM; Salinity profiles synthesized from temperature profiles and climatological temperature correlations and observed by Argo drifting floats. SST: Two daily SST analysis products were developed using optimum interpolation (OI).	2m temperature; 2m specific humidity; 10m ocean windspeed
MERRA, Rienecker et al. 2011	Atmospheric data: Winds, temperature and humidity profiles from radiosondes, dropsondes, pilot balloons and profilers; NEXRAD radar winds (1998–present); Surface pressure from land SYNOP reports; surface pressure, winds, temperature and humidity from ships and buoys; synthetic surface pressure observations (PAOBS); Temperature- and humidity-sensitive infrared radiances from HIRS and SSU (1979–2006); Temperature-sensitive microwave radiances from MSU (1979–2007) and AMSU-A (1998–present); Wind and temperature reports from aircraft; Cloud-track winds from geostationary satellites and from MODIS (2002–present); Moisture-sensitive radiances from SSM/I (1987–2009) and AMSU-B (1998–present), precipitation, and surface wind-speed over the ocean from SSM/I; Marine surface winds from ERS-1 (1991–1996), ERS-2 (1996–2001) and QuikScat (1999–2009); Temperature and moisture sensitive radiances from GOES sounders; TRMM rain rate; Temperature- and humidity-sensitive IR radiances from AIRS	2m temperature; MSU 2LT equivalent lower tropospheric temperature; MSU 4 equivalent lower stratospheric temperature; 2m specific humidity; 10m ocean windspeed
JRA-25, Onogi et al. 2007	Atmospheric data: Surface pressure, Radiosondes, Wind profiler, Aircraft wind, PAOBS, Tropical cyclone wind retrieval, AMV (including reprocessed wind), Infrared radiances from HIRS/SSU, Microwave radiances from MSU/AMSU/MHS, Precipitable water retrieval from microwave imagers, Scatterometer wind Surface data: Surface temperature, humidity and wind; Snow depth (including digitized data over China), Snow cover retrieval from microwave imagers	2m temperature; MSU 2LT equivalent lower tropospheric temperature; 2m specific humidity; 2m relative humidity; 10m ocean windspeed
ERA-Interim, Dee et al. 2011	Atmospheric data: Upper-air wind, temperature and humidity from radiosondes; dropsondes; pilot balloons and profilers; aircraft; Surface pressure, temperature and humidity from land SYNOP reports; surface pressure, temperature, humidity and wind from SHIP reports; surface pressure, temperature and wind from buoys; surface pressure from METAR; snow depth from SYNOP reports; Retrieved ozone from satellites; Retrieved winds from geostationary satellites; Radiances from temperature and humidity sounders: HIRS, SSU, MSU, AMSU-A/B, MHS; Radiances from passive microwave imagers over ocean: SSM/I, SSMI/S, AMSR-E; Ocean surface wind from scatterometers on ERS-1, ERS-2, QuikSCAT (from 1992); Radiances from geostationary infrared imagers on GOES, Meteosat and MTSAT (from 2001); GPSRO bending angles from CHAMP, COSMIC, GRAS (from 2001); Radiances from high-spectral resolution sounder: AIRS (from 2003); Retrieved winds from polar orbiting satellites: MODIS (from 2007) Surface data: Multisensor retrieved snow cover from NOAA/NESDIS (from 2003)	2m temperature; MSU 2LT equivalent lower tropospheric temperature; MSU 4 equivalent lower stratospheric temperature; 2m specific humidity; 2m relative humidity; 10m ocean windspeed; 10m land windspeed
ERA-40, Uppala et al. 2005	Atmospheric data: Upper-air wind, temperature and humidity from radiosondes, dropsondes, pilot balloons, TWERLE balloons (1975–1976) and US profilers (from 1996); Surface pressure, temperature and humidity from land SYNOP reports; surface pressure, temperature, humidity and wind from SHIP reports; snow depth from SYNOP reports and specialised datasets; Temperature- and humidity-sensitive infrared radiances from VTPR (1973–1978) and HIRS/SSU (from 1979); Flight-level wind and temperature from aircraft (from 1973); Temperature-sensitive microwave radiances from MSU and AMSU-A (from 1979); Retrieved winds from geostationary satellites (from 1979); Surface pressure, temperature and wind from buoys (from 1979); Total ozone from TOMS and ozone profiles from SBUV (from 1979); Total column water vapour and surface wind-speed over ocean from SSM/I (from 1987) Surface data: Synthetic surface-pressure obs from satellite imagery (from 1973); Oceanic wave height and surface wind from ERS 1&2 (from 1992)	2m temperature; MSU 2LT equivalent lower tropospheric temperature; MSU 4 equivalent lower stratospheric temperature; 2m specific humidity (not ocean); 2m relative humidity (not ocean); 10m ocean windspeed
20CR, Compo et al. 2011	Surface and Sea Level Pressure only	MSU 2LT equivalent lower tropospheric temperature; 2m specific humidity; 2m relative humidity; 10m ocean windspeed

SIDEBAR 2.1: THE USE OF REANALYSIS DATA FOR MONITORING THE STATE OF THE CLIMATE—D. DEE, P. BERRISFORD, M. G. BOSILOVICH, M. CHELLIAH, G. COMPO, A. EBITA, P. D. JONES, S. KOBAYASHI, A. KUMAR, G. RUTLEDGE, S. SAHA, H. SATO, A. SIMMONS, C. SMITH, AND R. VOSE

Estimates of atmospheric temperature, humidity, and wind from several reanalyses have been included among the many datasets used in this issue of *BAMS State of the Climate in 2010* (Table 2.2). A global atmospheric reanalysis is a coherent, multivariate reconstruction to determine the state of the atmosphere using observations and a consistent technique to combine them objectively (Fig. 2.1). The reconstructions are created with model-based data assimilation methods similar to those employed for numerical weather prediction. Reanalyses rely on a forecast model to propagate information in space and time, and to impose physically meaningful constraints on the estimates produced. In this way it is possible, for example, to extract useful information about rainfall from satellite observations of temperature and humidity, or to infer large-scale features of the global circulation in the early 20th century from only surface pressure observations available at the time (e.g., Compo et al. 2011).

Several centers now routinely extend their latest reanalyses close to real time and provide product updates to users at a short delay. Timely, comprehensive estimates of global climate

variables, consistently produced with an unchanged data assimilation system, can be useful for climate monitoring. It is clearly necessary, however, to evaluate uncertainties before drawing conclusions from assessments of year-to-year changes in climate based on reanalysis data. The accuracy of estimated trends and variability for any given variable depends on the strength of the observational constraint. This constraint varies throughout the reanalysis period as the input observations change in quality, quantity, and platform type. The contribution of observations also depends on the biases, errors, and uncertainties in the forecast models. Intercomparison of different reanalyses can be useful when considering trends over longer periods. Where possible, estimates from reanalysis data should also be compared with independent estimates based on observations alone. This is especially important for variables (such as precipitation) that are only indirectly constrained by the assimilated observations and hence depend crucially on the quality of the assimilating forecast model (Fig. 2.2).

Since first produced in the 1980s, reanalysis data have been widely used for research in the atmospheric sciences. Reanalysis is a rapidly evolving field; successive generations of products have improved in quality and diversity, reflecting major advances in modeling and data assimilation in recent decades. New reanalysis products additionally benefit from improvements in the observations and other required input datasets, such as specifications of sea surface temperature and sea ice concentration. These are the result of ongoing efforts in data reprocessing and recalibration by satellite agencies and other data providers, as well as recovery and digitization of early instrumental data that have not previously been used. The value and appeal of reanalyses arise from the accumulation of these benefits and their encapsulation in a comprehensive dataset conveniently provided on global grids. As reanalyses proliferate, metadata about the assimilated observations and forecast model become essential components for any assessment. A forum for sharing such information among producers and users of reanalysis data has recently been established at http://www.reanalyses.org.

Evaluation of the quality of reanalysis products is often provided by users, based on many different measures. Applications vary greatly, ranging from predictability and process studies to the validation of ecological models of biodiversity. Producers of reanalysis datasets closely monitor the quality of fit to observations used, the ability of the assimilating model to predict those observations, and the adjustments made to
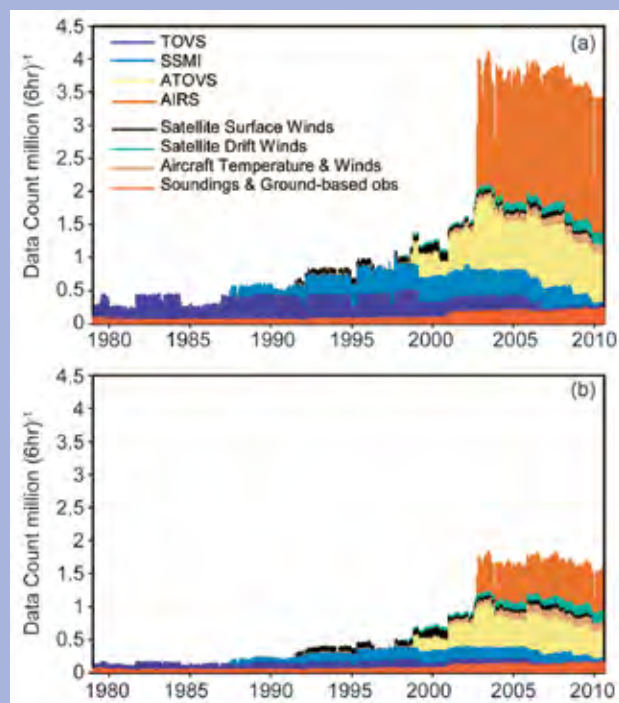

Fig. 2.1. Time series of (a) the number (millions) and types of observations considered for assimilation during a six-hour window and (b) those observations actually assimilated. (Source: Rienecker et al. 2011)
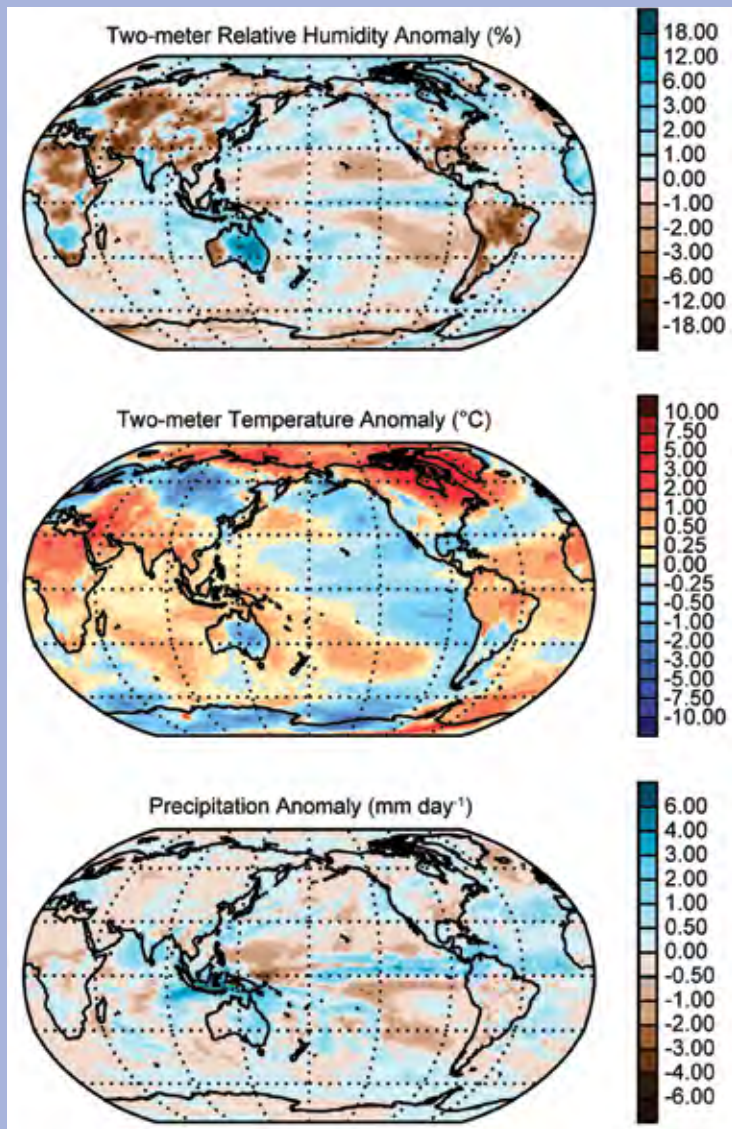
Fɪɢ. 2.2. ERA-Interim 2010 anomaly maps for 2 m relative humidity, 2 m temperature, and precipitation (accumulated in the 12 hr–24 hr range from twice-daily forecasts initiated at 00 UTC and 12 UTC), all relative to 1989–2008 base period averages. Note effects of the Russian dry heat wave and extreme rainfall in Australia. There is higher confidence in temperature and humidity where these are well constrained by observations and independently verified (Simmons et al. 2010). Uncertainties are largest in polar areas and central Africa. There is less confidence in precipitation, which is only indirectly constrained by observations—anomalies are likely excessive over tropical oceans but reasonable over most land points (Dee et al. 2011).

the predictions by the data assimilation procedure. These so-called analysis increments represent the net impact of the observations on the reanalyzed atmospheric fields. Systematic increments may be due to residual biases in observations, in the forecast model, or both. They can introduce artificial sources and sinks of heat, energy, and water in the reanalysis, and hence affect the global budgets for these quantities. Changes in the mean increments (e.g., associated with changes in the observing system) can affect trend estimates for basic climate variables derived from reanalysis data.

Reanalyses are used in the analysis of several variables in this chapter. Like more traditional observational datasets, individual reanalysis datasets have strengths and weaknesses. Although there have been a limited number of peer-reviewed comparisons [e.g., Simmons et al. (2010) for surface temperature and humidity; Dessler and Davis (2010) for free tropospheric humidity], in general, the performance of individual reanalysis products for specific parameters has not been rigorously quantified. The construction of reanalysis is a complex endeavor, and it is not unexpected that there will be a degree of spread among the reanalyses. Contemporary reanalysis products show considerably smaller spread than earlier generations, reflecting substantial advances in analysis methods, especially in the area of satellite data assimilation and in the ability to deal with biases in observations. These advances are expected to continue with coming generations of new reanalysis products.
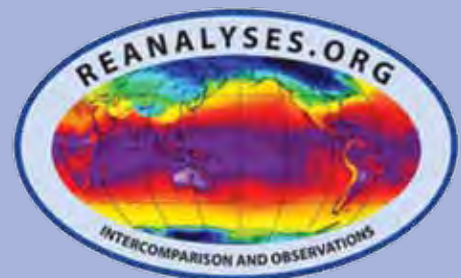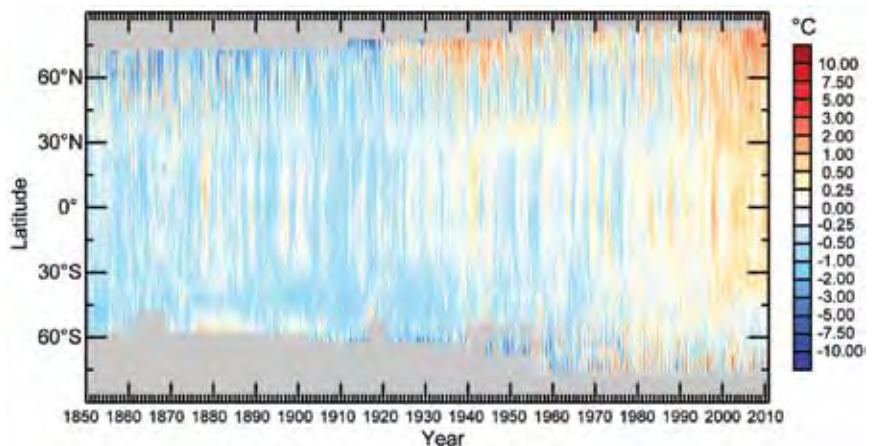
b. Temperatures

1) Surface temperatures—A. Sánchez-Lugo, J. J. Kennedy, and P. Berrisford

Global mean surface temperature in 2010 ranked as either the warmest or second warmest year in the instrumental record. The rank depends on which of the three methodologically independent analyses presented in this section are considered (NASA/GISS, Hansen et al. 2010; HadCRUT3, Brohan et al. 2006; and NOAA/NCDC, Smith et al. 2008). The year was 0.50°C above the 1961–90 average annual value in HadCRUT3 (second warmest after 1998), 0.52°C in the NOAA/NCDC analysis (tied warmest with 2005), and 0.56°C in the NASA/GISS analysis (tied warmest with 2005). The analyses use air temperatures over land and sea surface temperatures observed from ships and buoys. While they differ in their methods, which can lead to differences in the annual ranks, all three analyses are in close agreement (Fig. 2.3) that the global average surface temperature increased at a rate of 0.7°C per century since 1900 and approximately 0.16°C per decade since 1970.

Global average temperature can also be estimated from reanalyses (see Sidebar 2.1). These all indicate 2005 as the warmest year on record. Two of the


Fig. 2.4. HadCRUT3 monthly mean anomalies of surface temperature by latitude based on the 1961–90 base period. Gray areas indicate regions where data are unavailable.

reanalyses (ERA-Interim and JRA) give 2010 as the second warmest year (Fig. 2.3).

The year 2010 was characterized by two large-scale modes of variability that affected weather conditions across the globe—the El Niño-Southern Oscillation (ENSO) and the Arctic Oscillation (AO). The strong El Niño in the tropical Pacific Ocean during the first half of 2010 contributed to the exceptional warmth observed globally, resulting in one of the top two warmest January–June periods on record. El Niño persisted through April, but sea surface temperatures then declined rapidly across the tropical Pacific Ocean, giving way to La Niña conditions. By July La Niña was well established and by the end of the year it had intensified to a moderate-to-strong La Niña.

Despite the rapid development and strength of the La Niña, global average sea surface temperatures remained relatively high throughout the year. Above-average sea surface temperatures were present during the year across the Atlantic and Indian Oceans, with the most prominent warmth across the tropical Atlantic (Plate 2.1c).

A strong negative phase AO influenced temperature patterns across the Northern Hemisphere during most of 2010, contributing to unusually low temperatures over much of northern Eurasia and parts of the United States. Abnormal warmth affected much of Africa and southern Asia, with notable warm anomalies also across Canada and northern South America. Overall,
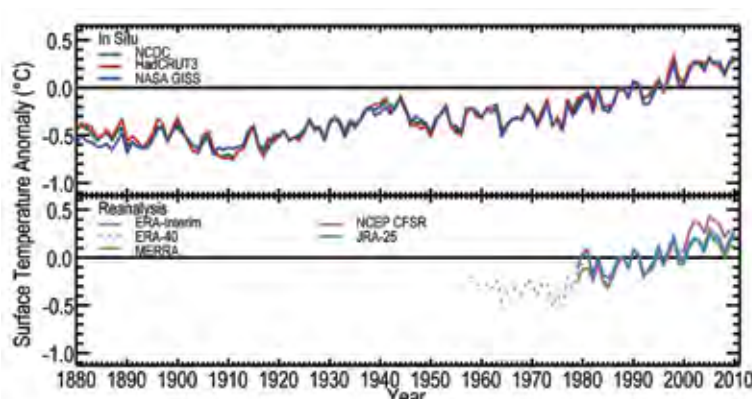
Fig. 2.3.Global average surface temperature annual anomalies. For the in situ datasets 2 m surface temperature is used over land and sea surface temperature over the oceans. For the reanalyses, a 2 m temperature is used over the whole globe. In situ datasets and the ERA-40 reanalysis use the 1961–90 base period whereas all other reanalysis datasets use the 1989–2008 base period. However, to aid comparison, all time series have been adjusted such that they give a mean of zero over the common period 1989–2001.
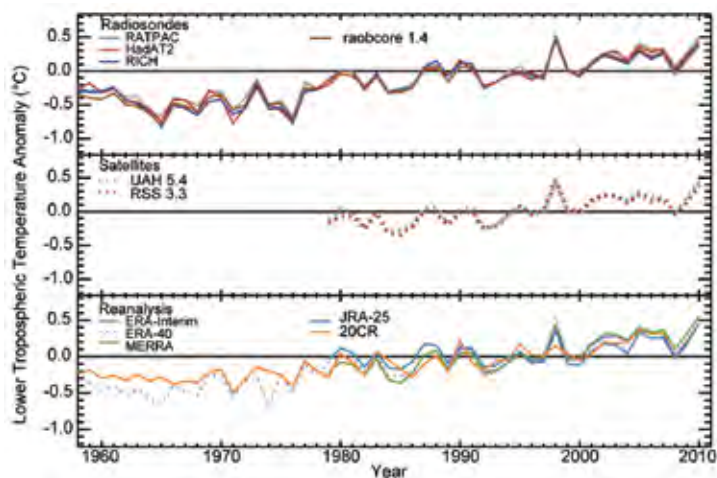
FIG. 2.5. Global average lower tropospheric temperature annual anomalies for the MSU 2LT (or equivalent) layer. Radiosonde [HadAT2 (Thorne et al. 2005–465 day, 384 night stations), RATPAC (Free et al. 2005–85 stations), RAOBCORE 1.4 (Haimberger 2007–1184 stations) and RICH (Haimberger et al. 2008–1184 stations)] and Satellite [UAHv5.4 (Christy and Norris 2009) and RSSv3.3 (Mears and Wentz 2009)] datasets use the 1981–2010 base period. ERA-40 uses the 1961–90 base period whereas all other reanalysis datasets use the 1989–2008 base period. However, to aid comparison, all time series have been adjusted such that they give a mean of zero over the common period 1989–2001.

the Northern Hemisphere land temperature was well above average throughout the year (Fig. 2.4).
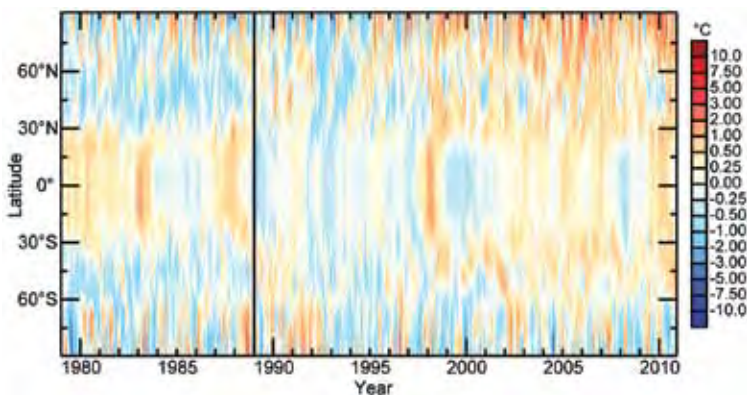
2) LOWER TROPOSPHERIC TEMPERATURES—J. Christy

Based on several sources of processed observations, the global lower tropospheric layer (TLT, surface to ~8 km) was approximately +0.4°C warmer than the 1981–2010 period average (Fig. 2.5, shown using a different base period). The year began in a strong warm-phase ENSO (El Niño) with individual monthly anomalies for January–April in some datasets being the warmest observed. When the tropical Pacific Ocean experiences large ENSO temperature anomalies, global TLT responds with similar temperature changes which, for the global average, lag the surface fluctuations by two to four months (Christy and McNider 1994). The 2010 warm phase switched rapidly to a cool phase (La Niña) as the year progressed. Given the lagged response, global TLT anomalies remained above average and cooled slowly while those of the tropical Pacific Ocean fell below aver-

age in the second half of the year (Fig. 2.6).

For the previous 32 (satellite) and 53 (radiosonde) years of records, 2010 ranked as warmest in RATPAC and second warmest year to 1998 in most of the datasets, though the difference is sufficiently small as to not be considered significant (Fig. 2.5). Global average anomalies were constructed using three systems: balloon-based radiosondes; satellite-based microwave sensors; and reanalyses (see Sidebar 2.1 for general information about reanalysis).

In the zonal mean, the evolution from a clear La Niña signal of cool tropics in the first half of 2008 to warm El Niño conditions through most of 2010 is marked (Fig. 2.6). Other longer-lived cool tropical events occurred around 1985, 1989, and 2000. Warmth similar to 2010 is seen in warm El Niños of 1982/83 and 1997/98. The cooling seen in 1992 is related to the volcanic eruption of Mount Pinatubo. Since the very warm 1998 El Niño, there appears to be a prevalence of warmer temperatures in the northern latitudes, tropics, and southern midlatitudes relative to prior years. In high southern latitudes, there appears to be no long-term trend.

The estimated linear trend for the entire time series (Fig. 2.5) beginning in 1958 (radiosonde era) and also beginning in 1979 (satellite era) is +0.15 ± 0.02°C per decade where the "±0.02" represents the range of the values calculated from the various data products listed. There is no indication of acceleration of the

FIG. 2.6. Combined ERA-40 (1979–88) and ERA-interim (1989–2010) monthly mean anomalies of lower tropospheric temperature by latitude. ERA-40 uses the 1961–90 base period whereas ERA-interim uses the 1989–2008 base period. Both datasets have been adjusted to have a mean of zero over the common period 1989–98 so that they can be shown together with the changeover indicated by the vertical black line.
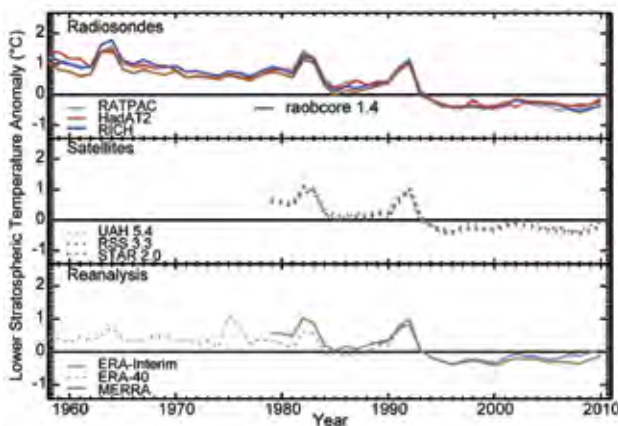
FIG. 2.7. Global average lower stratospheric tempera-ture annual anomalies for the MSU 4 (or equivalent) layer. Radiosonde [HadAT2 (Thorne et al. 2005–465 day, 384 night stations), RATPAC (Free et al. 2005–85 stations), RAOBCORE 1.4 (Haimberger 2007–1184 stations) and RICH (Haimberger et al. 2008–1184 stations)] and Satellite [UAHv5.4 (Christy and Norris 2009), RSSv3.3 (Mears and Wentz 2009) and STAR 2.0 (Zou et al. 2009)] datasets use the 1981–2010 base period. ERA-40 uses the 1961–90 base period and all other reanalysis datasets use the 1989–2008 base period. All time series have been adjusted such that they give a mean of zero over the common period 1989–2001 to aid comparison.

trend, though the relatively large excursions from the trend line make possible other interpretations than a single straight line (Seidel and Lanzante 2004).

The teleconnection patterns related to El Niño are somewhat muted in the 2010 annual average as the opposing effects of La Niña appeared late in the period. The El Niño impact is seen in the geo-graphical distribution of anomalies in Plate 2.1b with widespread warmer-than-average tropical values and cooler-than-average anomalies in the northeast and southeast Pacific. Significant warm anomalies are seen from Hudson Bay to Greenland, the tropi-cal North Atlantic eastward to Russia, and in much of the midlatitude Southern Hemisphere. Regions of cooler-than-average anomalies oc-curred in the southeastern U.S. northeastward to Europe, northern Asia, Australia, southern South America, and western Antarctica.
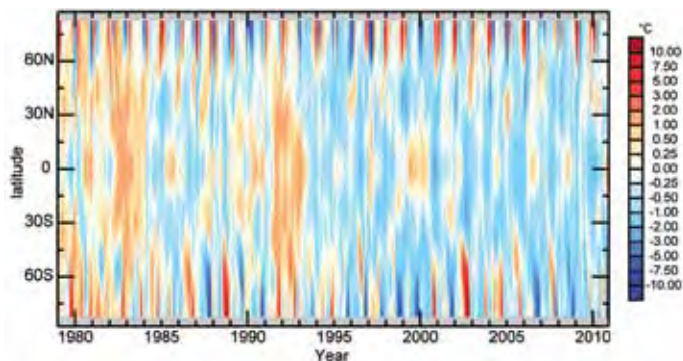
3) LOWER STRATOSPHERIC TEMPERATURES—M. Free

Efforts are underway to produce improved climate data records from the Stratospheric Sounding Unit (SSU) data and ultimately to merge them with the ongoing Advanced Micro-wave Sounding Unit (AMSU) data (Randel et al. 2009a). However, this work does not yet enable

reliable assessment of recent changes in temperature in the upper stratosphere and therefore the scope of this section is limited to the lower stratosphere.

The average temperature of the global lower stratosphere in 2010, for the layer measured by the MSU satellite data, was warmer than the mean of the previous 10 years in most datasets (Plate 2.1a; Figs. 2.7 and 2.8) but more than 1°C cooler than the early 1960s. It was ~0.1°C–0.2°C warmer than 2009 and ranked roughly 14th coolest since 1979—the exact ranking depends on the dataset. The global mean trends for 1958–2010 in radiosonde datasets (weighted to approximate the MSU retrieval) range from -0.29°C to -0.36°C per decade, and the trends for radiosonde and MSU datasets for 1979–2010 are -0.31°C to -0.54°C per decade. The MSU data show smaller cooling trends than the radiosonde datasets. Most reanalyses show generally similar evolution of the global mean stratospheric temperature to that shown by the other datasets. In the tropics, cooling trends for 1979–2010 are strongest in boreal winter months and minimal in March–April, while trends in Arctic temperatures have a roughly opposite sea-sonality. Trends in the Antarctic stratosphere show the strongest cooling from November to February (Free 2011), and November and December 2010 were unusually cool in that region.

Figures 2.7 and 2.8 show an overall cooling trend through the mid-1990s, interrupted by volcanic warming, with little change in temperature since 1995. Interannual variability in global mean tem-peratures in the lower stratosphere is dominated by warming resulting from the major volcanic erup-tions of Mount Agung (1963), El Chichón (1982) and MountPinatubo (1991). This effect is largest in the tropics and tends to be accompanied by a strength-ening of the Arctic polar vortex and cooling near the North Pole. In the tropical stratosphere, the Quasi-

FIG. 2.8. RSS monthly mean anomalies of lower stratospheric temperature by latitude. A 1989–98 base period is used. Gray areas indicate regions where data are unavailable.

Biennial Oscillation (QBO) is the strongest source of interannual temperature variation (Baldwin et al. 2001; Fig. 2.8). This oscillation in temperature and zonal wind direction propagates from the upper to the lower stratosphere with a time period of about 24–30 months for a complete cycle. The QBO response in the deep tropics is out of phase with its counterparts at higher latitudes (Fig. 2.8), and so the QBO effect on stratospheric temperature is much smaller in the global mean than in the tropics. Similarly, although El Niño tends to cool the lower stratosphere in the tropics and warm it in the Arctic (Free and Seidel 2009; Randel et al. 2009b), especially in boreal winter, its effects are not obvious when layer-mean stratospheric temperatures are averaged globally. The lower stratosphere also tends to be warmer when the 11-year solar cycle is at its maximum and cooler at its minimum. The observed global time series of lower stratospheric temperature reflects the combination of these natural sources of interannual variability with long-term anthropogenic cooling effects from ozone depletion and greenhouse gases.

In 2010, the QBO began in an easterly phase and then shifted to the westerly phase in the second half of the year, and this plus the shift to La Niña conditions caused the tropical stratosphere to warm in the fall (Fig. 2.8). Although the Arctic stratosphere warmed in February, this warming was not as unusually large as that of 2009. The Antarctic polar vortex was larger than average during 2010 and was relatively undisturbed after two warming events in July and August. The behavior of the Antarctic ozone hole is discussed in section 6g.

4) LAKE TEMPERATURE—P. Schneider and S. J. Hook

The temperatures of lakes and other inland water bodies are excellent indicators of climate change (Austin and Colman 2008; Livingstone 2003; Williamson et al. 2009). Previously, in situ temperature data have been used to measure the impact of climate change on lakes (Coats 2010; Quayle et al. 2002; Verburg et al. 2003). While these data are usually quite accurate, their availability is restricted to a few sites and continuous, reliable, long-term in situ observations are rare. Satellite thermal infrared (TIR) data have also been used to measure lake surface temperature (Crosman and Horel 2009; Hook et al. 2003; Hook et al. 2007; Reinart and Reinhold 2008; Schneider et al. 2009), though these studies were still limited geographically.

To provide a more global scope, Schneider and Hook (2010) utilized 25 years of TIR satellite data
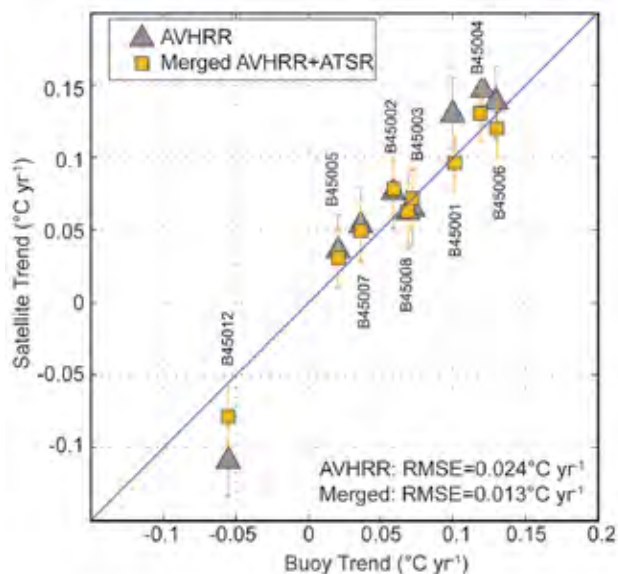

FIG. 2.9. Comparison of 1985–2009 Jul–Sep nighttime lake surface temperature trends derived from satellite data with those obtained from hourly measurements at nine buoys in the Great Lakes.

at 104 inland water bodies worldwide in order to determine possible trends in the seasonal nighttime surface water temperatures and to investigate if any spatial patterns in the trends would emerge. The study used seasonally averaged (July–September and January–March) nighttime data from the series of Advanced Very High Resolution Radiometers (AVHRR) and the series of Along-Track Scanning Radiometers (ATSR) obtained between 1985 and 2009. Satellite-based trends were found to closely match those derived from buoy data obtained from the National Data Buoy Center (NDBC), as validated over the American Great Lakes (Fig. 2.9). Using a merged dataset consisting of data from two sensors improves the agreement considerably.

Several consistent spatial patterns emerge from the mapped trends of the seasonal nighttime lake surface temperature (Fig. 2.10a). The area of the strongest and most consistent lake surface temperature increase is Northern Europe, where Lake Vänern, Lake Vättern, Lake Ladoga, and Lake Onega have warmed at an average rate of around 0.08°C yr^{-1}. The magnitude of the trends decreases slightly towards southeastern Europe and the Middle East. A more rapid decline in trend magnitude is visible towards central Asia. Lakes in North America have been warming at rates around 0.05°C yr^{-1}–0.06°C yr^{-1} on average. At lower latitudes, most inland water bodies showed much slower warming of 0.025°C yr^{-1} on average. A comparison with data from the GISTEMP (NASA GISS in section 2b1)
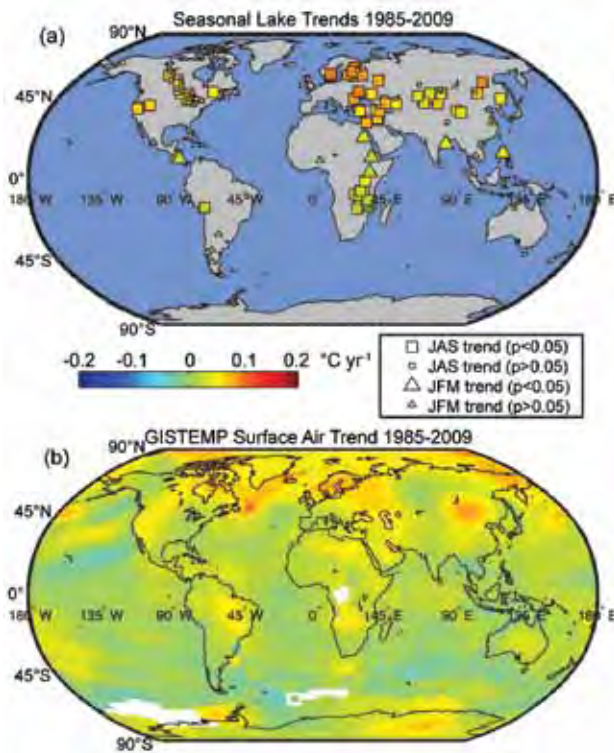
Fig. 2.10. Global (a) satellite-derived seasonal [Jul–Sep (JAS) and Jan–Mar (JFM)] nighttime lake surface temperature trends between 1985 and 2009, and (b) corresponding 1985 through 2009 JAS trends in surface air temperature obtained from GISTEMP (Hansen et al. 2006). JFM trends are not shown due to low number of JFM stations.

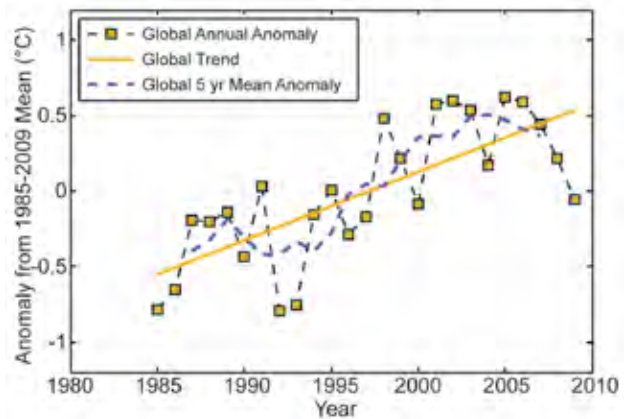Fig. 2.11. Global average nighttime lake surface temperature anomalies averaged over all study sites.

surface air temperature analysis (Hansen et al. 2006; Fig. 2.10b) shows qualitative agreement.

The average of all time series (Fig. 2.11) highlights features such as the cooling effect caused by the 1992 Mount Pinatubo eruption and the warm anomaly caused by the strong 1998 El Niño event. The mean trend over all sites is $0.045 \pm 0.011°C$ yr^{-1} (p < 0.001) and is dominated by the large number of water bodies in the midlatitudes of the Northern Hemisphere. When Northern and Southern Hemisphere are weighted equally, the global trend is $0.037 \pm 0.011°C$ yr^{-1}. The spaceborne TIR lake temperatures provide additional independent evidence on temperature change over land and for assessing the impacts of climate change throughout the world.

c. Hydrological cycle

1) SURFACE HUMIDITY—K. Willett, A. Dai, and D. Berry

Surface humidity has been monitored at some sites since the 19th century (e.g., Butler and García-Suárez 2011). Only during recent decades has the coverage become near-global, by weather stations over the land

and ship and buoy observations over the oceans. Historically, both specific humidity (q) and relative humidity (RH) have been derived from paired wet bulb and dry bulb thermometers. However, it is becoming increasingly common to use capacitance sensors to directly derive RH or dewpoint temperature.

There are three recent global-scale analyses of surface humidity: Dai (q and RH over land and ocean; Dai 2006); HadCRUH (q and RH over land and ocean; Willett et al. 2008); and the NOCS 2.0 (q only) ocean dataset (Berry 2009; Berry and Kent 2009). Only the NOCS 2.0 is updated to include 2010, but plans are underway to update HadCRUH over land on an annual basis, and to homogenize and update the Dai analysis. While all datasets use ship data over the ocean, HadCRUH and Dai include data from buoys, which are excluded from NOCS 2.0 owing to quality issues. All NOCS 2.0 data are then filtered by confidence in data quality and thus spatial coverage is far less than that of Dai and HadCRUH, especially over the Southern Hemisphere. NOCS 2.0 has also been bias adjusted for changes in ship height and instrument type over time and includes uncertainty estimates. Over land, Dai and HadCRUH contain many of the same station input data but methodologies are different. HadCRUH has been adjusted to remove gross inhomogeneities over land.

Recently, the ECMWF reanalysis product ERA-Interim and its predecessor ERA-40 were compared with land surface humidity from HadCRUH (Simmons et al. 2010) where good overall agreement was found. For this reason, ERA-Interim is considered suitable to monitor land surface humidity and so is used here to provide data for 2010. Other fourth generation reanalyses products are also shown where humidity fields are available for comparison.
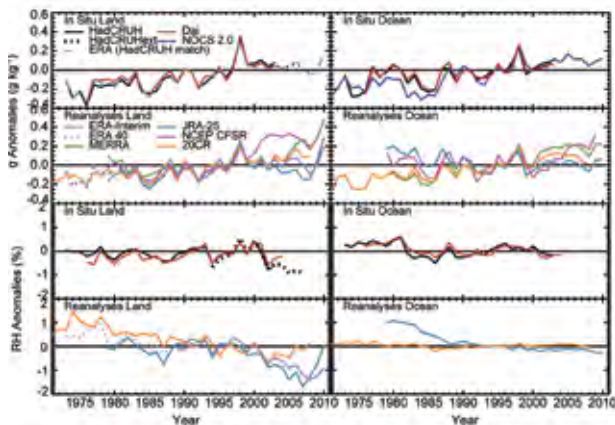
FIG. 2.12. Global average surface humidity annual anomalies. For the in situ datasets 2 m surface humidity is used over land and ~10 m over the oceans. For the reanalysis datasets, 2 m humidity is used over the whole globe. The specific humidity (q) and relative humidity (RH) are shown for land and ocean separately. HadCRUH, HadCRUHext, and ERA (HadCRUH match) use the 1974–2003 base period. Dai uses the 1976–2003 base period. NOCS 2.0 uses the 1971–2010 base period. The combined ERA-40 (1973–88) and ERA-Interim (1989–2010) use the 1989–2009 base period. All other reanalysis datasets use the 1989–2008 base period. All datasets are adjusted to have a mean of zero over the common period 1989–2001 to allow direct comparison. Differences in data ingestion and sea ice cover between reanalysis datasets, and in spatial coverage between reanalysis and in situ data, should be taken into account. For example, slight differences are shown between ERA spatially matched to the sampling of HadCRUH (see 'In situ Land' panel) compared to the full spatial coverage time series (see 'Reanalyses Land' panel).

Global surface moisture content, as shown by q, has been gradually increasing since the early 1970s, consistent with increasing global temperatures (Fig. 2.12). Trends are similar for both the land and oceans but with apparent peaks during strong El Niño events (1982/83, 1997/98). Since 1998 q over land has flattened somewhat but 2010 shows an increase from 2009. Although there is some spread across the datasets, there is good general agreement—less so for the reanalysis-generated ocean q.

Globally, specific humidity for 2010 (Plate 2.1f) strongly resembles a La Niña pattern, and is broadly consistent with that of precipitation (Plate 2.1g) and total column water vapor (Plate 2.1e). There are dry anomalies over the eastern tropical Pacific and moist anomalies over the western tropical Pacific.

ERA-Interim and HadCRUH-ext show a slight decline in global land RH from 1998 to present (Sim-

mons et al. 2010), also shown in MERRA, consistent with a steady q and coincident rising temperature over this period. However, 2010 appears to be a more humid year on average. Prior to 1982, Dai and HadCRUH show positive RH anomalies over oceans. While Willett et al. (2008) speculate non-climatic causes, more recent investigation by Berry (2009) appears to implicate the North Atlantic Oscillation (NAO). RH in the reanalyses oceans is inconclusive.

2) TOTAL COLUMN WATER VAPOR—C. Mears, J. Wang, S. Ho, L. Zhang, and X. Zhou

The map of total column water vapor (TCWV) anomalies for 2010 (Plate 2.1e) includes data both from the Advanced Microwave Scanning Radiometer EOS (AMSR-E; over the oceans; Wentz 1997; Wentz et al. 2007) and from a subset of the ground-based GPS stations with continuous data from 1997 through 2010 (J. Wang et al. 2007). This subset was chosen so that a meaningful anomaly estimate could be calculated—many more stations would be available if this
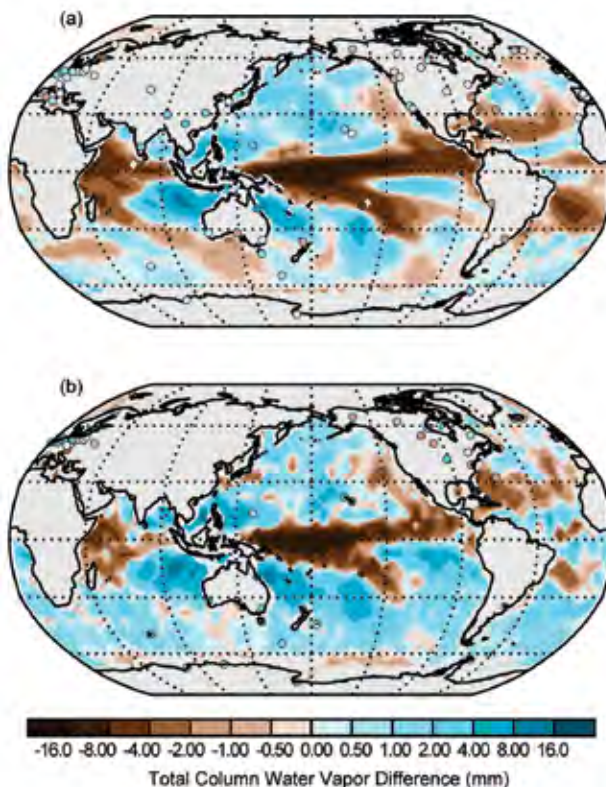
FIG. 2.13. Change in total column water vapor anomalies from Jan–Jun 2010 to Jul–Dec 2010. (a) Measurements from AMSR-E and ground based GPS stations. (b) Measurements from COSMIC, calculated using climatological data from SSM/I and AMSR-E over ocean and using climatological data from ground-based GPS over land.
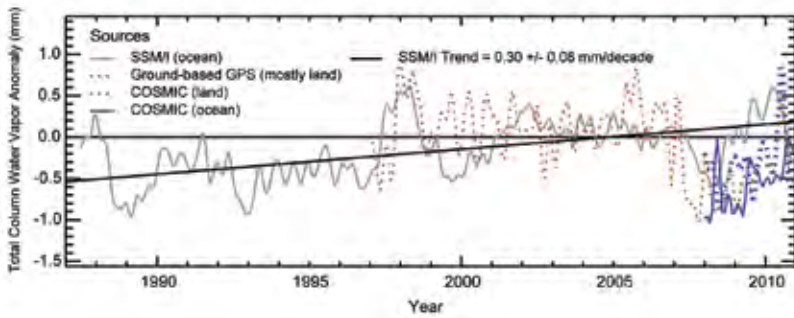
FIG. 2.14. Anomaly time series of total column water vapor both from SSM/I, ground-based GPS, and COSMIC (1997–2009 base period). The COSMIC ocean anomalies are calculated relative to an SSM/I climatology for 1997–2009. The COSMIC land anomalies are calculated only at the locations of GPS ground stations, and are relative to a 1997–2009 ground-based GPS climatology. The time series have been smoothed to remove variability on time scales shorter than six months.

requirement were relaxed since the size of the network is increasing rapidly with time. There is general agreement between the AMSR-E and ground-based GPS measurements at locations where overlaps occur with differences typically less than 0.5 mm. In the Pacific Ocean there is a large "C"-shaped dry anomaly, while in the oceans surrounding northern Australia, there is a very strong wet anomaly. Both features are associated with the onset of a moderate-to-strong La Niña event during the latter half of 2010. The onset of La Niña is depicted more clearly by plotting the TCWV difference between the July–December and January–June averages for 2010 (Fig. 2.13). The changes in TCWV from early to late 2010 measured by three different measurement systems [AMSR-E (ocean), GPS (land) and the Constellation Observing System for Meteorology, Ionosphere and Climate (COSMIC; land and ocean; Anthes et al. 2008; Ho et al. 2010]
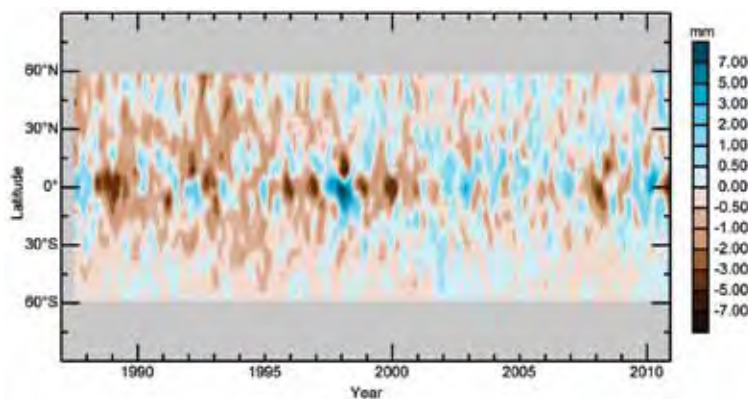
FIG. 2.15. SSM/I and AMSR-E measurements of monthly mean total column water vapor anomalies by latitude. The anomalies are relative to a base period of 1997–2009 smoothed in the time direction to remove variability on time scales shorter than four months. Gray areas indicate regions where data are unavailable.

show the dramatic drying of the tropical Pacific as the climate system shifted to moderate-to-strong La Niña conditions by fall 2010.

The combined Special Sensor Microwave Imager (SSM/I) AMSR-E TCWV, from the world's ice-free oceans, shows dramatic maxima in 1987/88, 1997/98, and 2009/10, associated with El Niño events (Fig. 2.14). Minima are apparent in Northern Hemisphere winters during the La Niña events of 1988/89, 1992/93 (also influenced by the eruption of Mount Pinatubo), 1999/2000, 2007/08, and late 2010. GPS data, only available since 1997, show similar features (Fig. 2.14). An exact match between SSM/I and AMSR-E and GPS is not expected since the two measurement systems sample different regions of the globe. The COSMIC data are in good agreement with the GPS data, but are biased slightly low relative to the SSM/I and AMSR-E data. A Hovmöller plot derived from SSM/I and AMSR-E (Fig. 2.15) shows that the changes associated with El Niño/ La Niña are largest in the tropics.

3) Precipitation—P. Hennon, M. Kruk, K. Hilburn, X. Yin, and A. Becker

Annual land precipitation anomalies (Fig. 2.16) were calculated from the Global Historical Climatology Network Monthly Version 2 (GHCN; Peterson and Vose 1997), the Global Precipitation Climatology (GPCC; Schneider et al. 2008), and the Global Precipitation Climatology Project Version 2.1 (GPCP; Adler et al. 2003) datasets, and were determined with respect to the 1961–90 mean using stations reporting a minimum of 25 years of data during the base period. The global anomaly for 2010 and percent change over time are shown using GHCN in Plate 2.1g and Fig. 2.17, respectively.

The year 2010 exhibited a large positive mean precipitation anomaly in GHCN and GPCC (no 2010 data is yet available for GPCP). The GHCN indicates the globally averaged annual precipitation over land was 1112.1 mm, or 50.4 mm above normal. According to GPCC, the anomaly was 938.5 mm or 21.5 mm above normal. While both positive, the difference in magnitude between
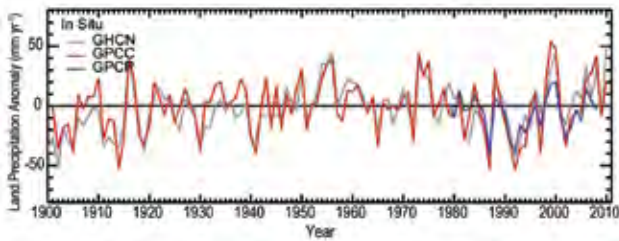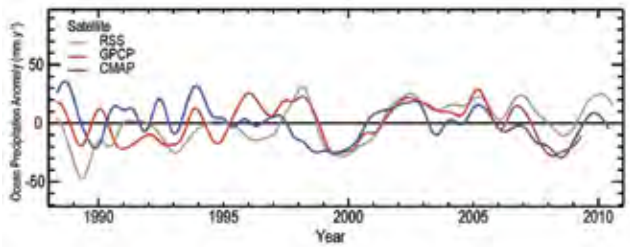
FIG. 2.16. Global average precipitation annual anomalies over land from in situ data. All data are shown relative to a 1961–90 base period.


FIG. 2.18. Global average precipitation annual smoothed anomalies over ocean from satellites. All datasets are shown relative to a 1988–2010 base period.

the GHCN and the GPCC time series is presumably tied to the number of available stations for use in the analysis, with GPCC incorporating at least an order of magnitude more stations than GHCN (NOAA, 7 January 2011: http://www.ncdc.noaa.gov/ghcnm/v2.php; Rudolf and Becker 2011).

Global ocean coverage is provided by satellite-based observations. Microwave sensors measure the total liquid in the column. The microwave era now spans 23 complete years, enabling the monitoring of climate variations. The global ocean precipitation climatology is produced using Remote Sensing Systems (RSS) intercalibrated passive microwave rain retrievals from a total of eight microwave imagers (Hilburn and Wentz 2008a). For 2010, data are available from the TRMM Microwave Imager (TMI) and the Advanced Microwave Scanning Radiometer-EOS (AMSR-E). Data from F13 Special Sensor Microwave Imager (SSM/I) stopped in November 2009; and while F15 is still producing data, contamination from a RADCAL beacon (Hilburn and Wentz 2008b) precludes their usage for climate monitoring.

Figure 2.18 shows global ocean time series for RSS as well as Version 2.1 GPCP (Adler et al. 2003) and V1101 CPC Merged Analysis of Precipitation (CMAP) data (Xie and Arkin 1997). Analysis of these satellite datasets shows a return to drier anomalies in 2010

after a wet year in 2009. The contrast between the global land and ocean precipitation is notable.

Precipitation anomalies in 2010, over both land and ocean reflected the transition from El Niño to La Niña during the boreal summer 2010. Over land there are drier conditions across the Southern Hemisphere and wetter-than-average conditions across the Northern Hemisphere midlatitudes (Fig. 2.17). Over the ocean, the time-latitude section (Fig. 2.19) shows a wet anomaly just north of the Equator, replaced by a dry anomaly midyear. The subtropical Southern Hemisphere was covered by an expansive but weak dry anomaly. Both the northern and southern midlatitudes had moist anomalies. The anomaly map for 2010 (Plate 2.1g) shows a complex mix of El Niño- and La Niña-related anomalies over the western tropical Pacific and wet anomalies over the southern Indian Ocean. Wet anomalies surrounded the Indian subcontinent and the Atlantic Ocean.

The seasonal analyses of global precipitation anomalies over land (Fig. 2.20) show patterns consistent with El Niño in December–February (a) and the transition to the developing La Niña in late-season [March–May, (b)], with classic La Niña patterns by June–August (c) continuing through September–November (d). During March–May the Northern Hemisphere exhibited wetter-than-average conditions. In
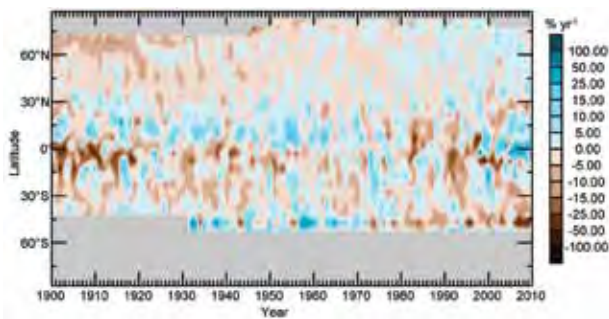
FIG. 2.17. GHCN measurements of annual mean precipitation anomalies over land by latitude. The anomalies are relative to a base period of 1961–90. Gray areas indicate regions where data are unavailable.
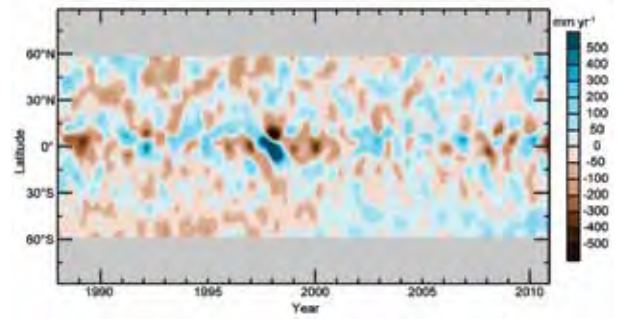
FIG. 2.19. RSS measurements of monthly mean precipitation anomalies over ocean by latitude. The anomalies are relative to a base period of 1988–2010. Gray areas indicate regions where data are unavailable.

Fig. 2.20. Seasonal global precipitation anomalies determined using the GHCN-monthly dataset for (a) Dec 2009–Feb 2010, (b) Mar–May 2010, (c) Jun–Aug 2010 and (d) Sep–Nov 2010. Seasonal anomalies are shown relative to a 1961–90 base period, where, for inclusion, at least 66% of years without missing data during the base period are required.
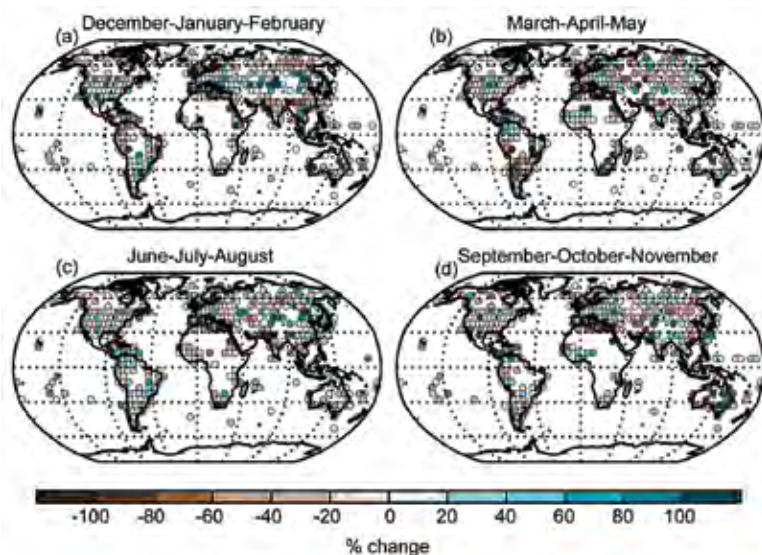
the Southern Hemisphere, dry conditions prevailed along the western continental margins consistent with a developing La Niña. In September–November, the Southern Hemisphere precipitation anomalies exhibited classic La Niña signals with predominantly dry conditions in South America and South Africa and wet conditions in central and eastern Australia.

### 4) Northern Hemisphere continental snow cover extent—D. A. Robinson

Annual snow cover extent (SCE) over Northern Hemisphere land averaged 24.6 million km^2 in 2010. This is 0.4 million km^2 less than the 41-year average and ranks 2010 as having the 13th least extensive cover on record (Table 2.3). This evaluation considers snow over the continents, including the Greenland ice sheet. The SCE in 2010 ranged from 48.4 million km^2 in February to 2.4 million km^2 in August. Monthly SCE is calculated at the Rutgers Global Snow Lab from daily SCE maps produced by meteorologists at the National Ice Center (a U.S. joint NOAA, Navy, and Coast Guard facility), who rely primarily on visible satellite imagery to construct the maps.

The year began with SCE in the highest quartile over Eurasia and North America. February had the third greatest SCE over North America and the Northern Hemisphere. Eurasia remained in the top quartile in

March while snow melted exceedingly quickly over North America, resulting in a decline to the lowest quartile. April SCE was the lowest on record across North America, with both North America and Eurasia ranking lowest in May and June. The 2010/11 snow season began with SCE a little above average in October and November, rising to the fourth highest value across Northern Hemisphere lands in December.

The expansive fall and winter SCE of the past two years has generally countered the low extents of spring and summer. Thus the 12-month running Northern Hemisphere SCE mean has recently been just below the long-term average (Fig. 2.21). Recent means are higher than throughout immediate preceding years.

The expansive winter cover appears to be associated with a strongly negative Arctic Oscillation during early and late 2010. This delivered enough cold air to midlatitude regions to result in significant snowfall and an expansion of SCE. This is apparent over the contiguous United States, where SCE ranked in the highest quartile during January and February 2010, before falling to the lowest quartile in April and May. New seasonal snow at year's end resulted in a top quartile ranking for November and December SCE. Alaskan snow melt was on the early side, with May and June SCE in the lower quartile. A slow start to the 2010/11 Alaskan snow season was followed by above-average SCE in November.
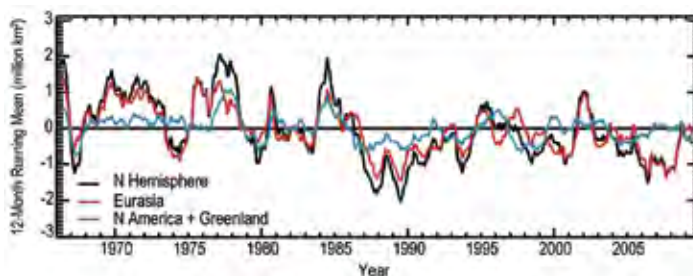
Fig. 2.21. Twelve-month running anomalies of monthly snow cover extent over Northern Hemisphere land (including Greenland) as a whole and Eurasia and North America separately between Nov 1966 and Dec 2010. Anomalies are calculated from NOAA snow maps. Mean hemispheric snow extent is 25.0 million km^2 for the full period of record. Monthly means for the period of record are used for nine missing months between 1968 and 1971 in order to create a continuous series of running means. Missing months fall between June and October; no winter months are missing.

Table 2.3. Monthly and annual climatological information on Northern Hemisphere and continental snow extent between November 1966 and December 2010. Included are the numbers of years with data used in the calculations, means, standard deviations, 2010 values, and rankings. Areas are in millions of square kilometers. 1968, 1969, and 1971 have 1, 5, and 3 missing months respectively, thus are not included in the annual (Ann) calculations. North America (N. Am.) includes Greenland. Ranks are from most extensive (1) to least (ranges from 41 to 45 depending on the month).

	Yrs	Mean	Std. Dev.	2010	2010 N.Hem. rank	Eurasia rank	N. Am. rank
Jan	44	46.7	1.5	48.3	6	11	6
Feb	44	45.6	1.8	48.4	3	10	3
Mar	44	40.3	1.8	40.6	18	10	37
Apr	44	30.5	1.7	28.3	41	21	44
May	44	19.5	1.8	15.2	44	44	44
Jun	43	10.1	2.1	6.0	43	43	43
Jul	41	4.2	1.2	2.6	40	40	40
Aug	42	3.1	0.7	2.4	36	38	32
Sep	42	5.3	0.9	5.3	19	20	20
Oct	43	17.9	2.5	18.8	15	13	17
Nov	45	33.6	2.0	34.0	20	25	13
Dec	45	43.3	1.8	45.7	4	6	7
Ann	41	25.0	0.9	24.6	29	21	33

Maps depicting daily, weekly (new), and monthly conditions, daily (new) and monthly anomalies, and monthly climatologies for the entire period of record may be viewed at the Rutgers Global Snow Lab website (see Table 2.1). Monthly SCE for the Northern Hemisphere, Eurasia, North America, the contiguous United States, Alaska, and Canada are also posted, along with information on how to ftp weekly areas and the weekly and monthly gridded products.

5) Global cloudiness—M. Foster, S. A. Ackerman, A. K. Heidinger, and B. Maddux

Global cloudiness in 2010 was characterized by a shift in the El Niño-Southern Oscillation, a negative phase of the Arctic Oscillation, and some continental cloudiness anomalies. During the early part of the year, sea surface temperature and wind field anomalies associated with El Niño drove enhancement of large-scale convection in the central Pacific and suppression of convective activity in the western Pacific near Indonesia, as shown by PATMOS-X cloudiness in Fig. 2.22a. During the boreal spring (Fig. 2.22b) a transition from El Niño to ENSO-neutral occurred, resulting in positive cloudiness anomalies around Indonesia and negative anomalies around the central equatorial Pacific by midyear (Fig. 2.22c). La Niña conditions emerged in July and persisted through the rest of the year. As a consequence of both phases of ENSO occurring in 2010, the annual global cloudiness anomaly map does not show a strong ENSO signature over much of the Pacific (Plate 2.1d), though the ~20% negative anomaly off the coast of Papua New Guinea is statistically significant at the 5% level, as is the dipole off the coast of Peru and Chile.

The Arctic Oscillation was negative for most of 2010. This may partially explain the 2010 cloud anomalies seen in the Northern Hemisphere winter, e.g., lower cloud amount over Eurasia, the North Atlantic, and northeast Pacific, and increased cloud amounts over eastern North America.
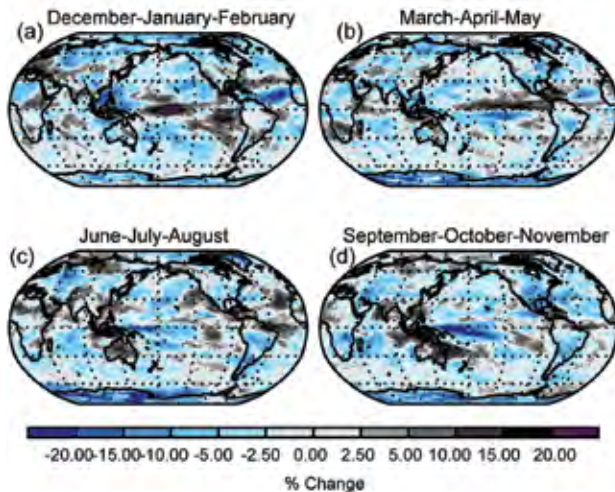
Fig. 2.22. Seasonal global cloudiness anomalies determined using the PATMOS-X dataset for (a) Dec 2009–Feb 2010, (b) Mar–May 2010, (c) Jun–Aug 2010, and (d) Sep–Nov 2010. Seasonal anomalies are calculated by subtracting the mean cloud fraction over the 1982–2010 base period from that of 2010.

Some annual cloudiness anomalies that are significant at the 5% level coincided with some continental extreme weather conditions. For example, positive annual cloudiness anomalies occurred over eastern Australia, which experienced one of its wettest years on record (see section 7h1). Significant negative annual anomalies occurred over Russia and northwestern Brazil, where severe drought conditions persisted for much of the year (see sections 7g1 and 7d2, respectively).

Figure 2.23 shows global mean monthly cloud anomalies from six cloud records. The HIRS cloud retrieval record works on the premise that synthesis of discrete carbon dioxide absorption bands in the IR spectrum can be used to detect the presence of cloud. In addition, an updated version of the PATMOS-x record (Version 5) is used, which includes a new Bayesian cloud masking algorithm and a diurnal correction to account for satellite drift. The monthly mean values from which the anomalies are derived are necessarily different for each record as the periods and lengths of the records vary, making a direct comparison challenging. The cloud record anomalies are smaller than the seasonal and diurnal variability within each data record. Relative differences between the records can in part be attributed to variations in how cloud-masking algorithms define cloud versus clear-sky thresholds. Artifacts within each record may also arise from factors such as satellite drift and sensor calibration. Relative to the entire PATMOS-x time series, 2010 was less cloudy than average. The

mean cloudiness for the year was 64.6%, which is 1.2% lower than the 29-year average, making 2010 the seventh least cloudy year of the record. All twelve months were less cloudy than their climatological monthly means over the entire record.

6) RIVER DISCHARGE—B. M. Fekete and A. Macdonald

The lack of a global, real-time reporting, discharge-monitoring network still hinders the accurate assessment of river flow. Although the monitoring infrastructure is largely in place (Hannah et al. 2011), continued difficulty in attracting funding and fostering international cooperation are major obstacles even though traditional in situ networks are much cheaper than satellite platforms. Remote sensing capabilities to estimate riverine water fluxes have been discussed by a number of authors (Alsdorf and Lettenmaier 2003; Alsdorf et al. 2007; Andreadis et al. 2007; Brakenridge et al. 2005). Recently, Syed et al. (2010) proposed calculation of fresh water fluxes from the continents, based on satellite-measured precipitation and evaporation over the ocean in conjunction with sea level measurement. The authors identified a weak overall increase in discharge to the oceans during the 1994–2006 period composed of a rapid increase between 1994 and 2000, followed by
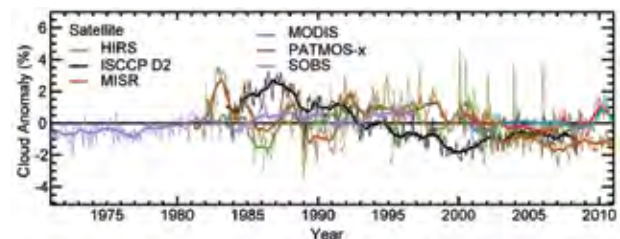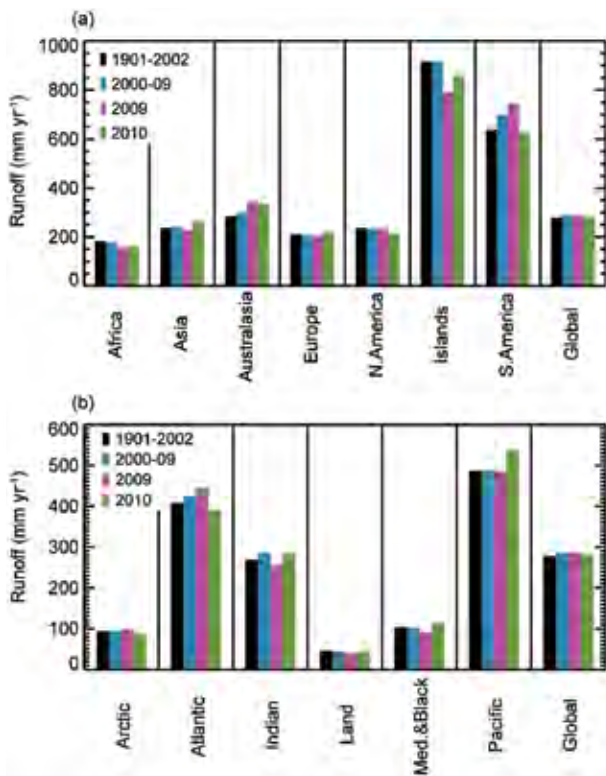

Fig. 2.23. Global average cloudiness monthly anomalies, defined as the current month minus the mean over the entire dataset for the corresponding month. The datasets include (a) surface weather observations (SOBS; Hahn and Warren 2007) spanning 1971–96; (b) Moderate Resolution Imaging Spectroradiometer (MODIS; Ackerman et al. 2008); (c) Multiangle Imaging Spectroradiometer (MISR; Di Girolamo et al. 2010) instruments, which are located on NASA's Terra satellite and span 2000–present (a MODIS instrument is also located on NASA's Aqua satellite and is included in the climatology); (d) International Satellite Cloud Climatology Project (ISCCP) data derived from the imaging radiometers on the operational weather satellites of several nations for the period 1983–2008; (e) High Resolution Infrared Sounder (HIRS; Wylie et al. 2005); and (f) PATMOS-x AVHRR (Heidinger and Pavolonis 2009), which are instruments located on the NOAA polar orbiting satellite series. Thick solid lines represent the time series of average cloudiness with a 12-month boxcar filter applied.
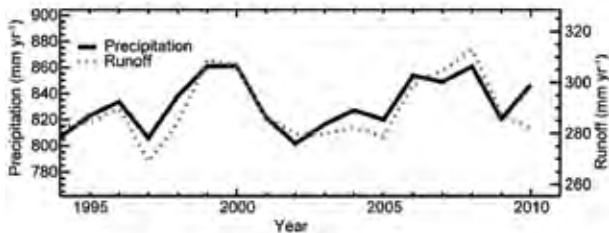
Fig. 2.24. Annual continental precipitation from GPCC full product extended with the monitoring product for 2010 and the corresponding water balance model-simulated continental runoff using NCEP air temperature forcing.

a slow decline during the next six years. The Syed et al. (2010) study is consistent with the water balance calculations presented here, that are forced by NCEP reanalysis (Kalnay et al. 1996; Kistler et al. 2001) air temperatures combined with monthly precipitation estimates from the Global Precipitation Climate Center (GPCC; Fig. 2.24). The error bars reported by Syed et al. (2010) are of similar magnitude to uncertainties in typical water balance calculations (Vörösmarty et al. 1998); however, the former approach lacks spatial

specificity within the continental land mass. Traditional hydrological model simulations appear to offer the best approximation of water resources when in situ observations are missing.

In 2010, GPCC revised its full product from V004 (covering 1901–2007) to V005 for the 20th century. They introduced a new monitoring product, V3, which addressed the bias between the full and monitoring products that were reported here last year. The improved consistency between the full and monitoring products allowed a continuous river discharge simulation from the historical past to the present. The historical simulation (1901–2002) combines the GPCC full product with gridded monthly air temperature (T_A) from the Climate Research Unit of University of East Anglia (CRU; New et al. 2000). Contemporary simulations (1948–present) use NCEP reanalysis daily air temperature as forcing and precipitation for downscaling monthly GPCC precipitation products to daily temporal frequency, while maintaining the monthly totals from GPCC.

Global runoff in 2010 decreased slightly compared to 2009 (Fig. 2.25; Plate 2.1h—absolute values) but it remained higher than the long-term 20th century average. In 2010, Asia experienced greater runoff compared to both the 20th century and the last decade (Fig. 2.25a). This can also be seen in the higher than long-term average runoff to the Indian and Pacific Oceans (Fig. 2.25b). In contrast, South America remained drier and the Atlantic Ocean received less runoff than the long-term average. These continental and ocean basin trends have significant spatial variations within continents, as shown in Fig. 2.26. Re-
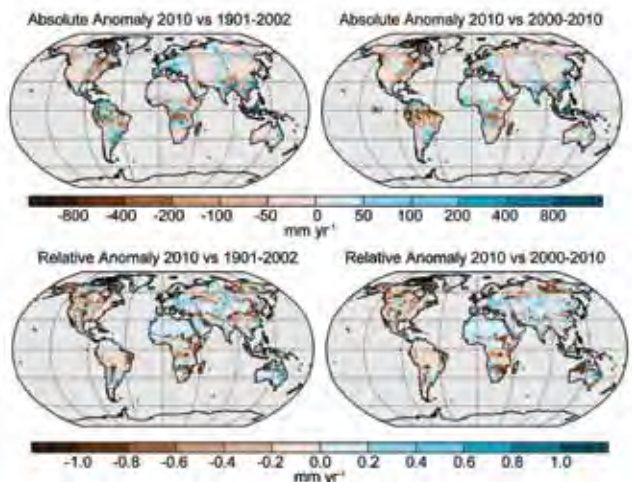

Fig. 2.25. River runoff by (a) continent and (b) receiving oceans, comparing average runoff over the 1901–2002 and 2000–09 periods to 2009 and 2010. "Islands" refers to the Pacific Islands, "Med.+Black" refers to the Mediterranean and Black Sea drainage regions and "Land" represents the mean of all internal (endorheic) basins found on every continent.

Fig. 2.26. Absolute and relative anomalies for river discharge in 2010 with respect to the long-term average over the 20th century and for the last decade.
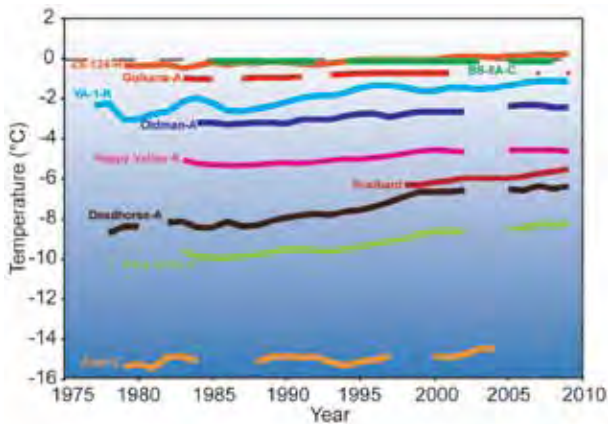
Fig. 2.27. Time series of mean annual ground temperatures at depths between 10 m and 20 m for boreholes throughout the circumpolar northern permafrost regions. Data sources: North American (Smith et al. 2010), Russian (Romanovsky et al. 2010b), and Nordic sites (Christiansen et al. 2010). 'C' denotes a Canadian site; 'A' denotes an Alaskan site; and 'R' denotes a Russian site. The Svalbard site is Janssonhaugen, which is also called PACE-10 (Isaksen et al. 2007). Measurement depth for Russian boreholes and 85-8A is 10 m; Gulkana, Oldman and Alert are 15 m; and all other boreholes are 20 m. Coordinates for borehole locations are: ZS-124: 67.4°N, 63.4°E; 85-8A: 61.6°N, 121.1°W; Gulkana: 62.2°N, 145.5°W; YA-1: 67.5°N, 64°E; Oldman: 66.4°N, 150.6°W; Happy Valley: 69.1°N, 148.8°W; Svalbard: 78.2°N, 16.5°E; Deadhorse: 70.2°N, 148.5°W; West Dock: 70.4°N, 148.5°W; Alert: 82.5°N, 62.4°W. [Source: Romanovsky et al. (2010b)]

gions with higher-than-average runoff were southern Spain, Central Europe, Pakistan, India, and China, while Brazil, the eastern United States, and Alaska were drier than average.

7) Permafrost thermal state—H. Lantuit, H. Christiansen, J. Noetzli, V. Romanovsky, N. Shiklomanov, S. Smith, G. Vieira, and L. Zhao

During the International Polar Year (IPY) in 2008 and 2009 there was substantial enhancement of the permafrost monitoring network in the polar regions (e.g., Christiansen et al. 2010; Romanovsky et al. 2010a; Smith et al. 2010; Vieira et al. 2010), and also in the high altitude regions of Europe, Scandinavia, and Asia (PERMOS 2010; Schoeneich et al. 2010; Isaksen et al. 2011; Zhao et al. 2010). Current permafrost thermal state data are now publicly avail-

able (see Table 2.1). Enhancement of the network has been aimed at areas with little recent information and to cover the range of climate, vegetation, geomorphologic, and geologic conditions in the global permafrost regions. Data from Russia and North America (see Table 2.1) indicate that permafrost temperatures within the discontinuous zone fall within a narrow range, generally 0°C to -2.5°C. In the continuous zone (e.g., high Arctic), permafrost can be as cold as -15°C (Fig. 2.27; Romanovsky et al. 2010a; Smith et al. 2010). New information on permafrost in Antarctica showed temperatures slightly below 0°C in the South Shetlands near sea level, decreasing southwards and eastwards in the Antarctic Peninsula region. In other regions of the Antarctic continent, temperatures are much lower, varying from -8°C at low-altitude coastal sites to below -17°C at the McMurdo Dry Valleys and higher elevation sites. Active layer depths range from over 1.6 m, especially at bedrock sites in the maritime Antarctic, to less than 0.1 m in some sites in continental Antarctica (Vieira et al. 2010). Here, temperatures are often taken from shallow boreholes and may not be representative of the mean annual ground temperature (MAGT). In Central Asia, much of the permafrost is currently close to 0°C (Zhao et al. 2010). In the European Alps and Scandinavian mountains, permafrost distribution is discontinuous and MAGT measured in boreholes are typically between 0°C and -3°C, with sites at very high elevation as well as in polar mountain regions being considerably colder (e.g., Haeberli et al. 2010; Fig. 2.28). Spatial variability of surface thermal conditions is high here and results from steep topography, heterogeneous surface characteristics, and snow cover.

Data records, some 30 years in length, are available for some sites in polar and mountain regions of
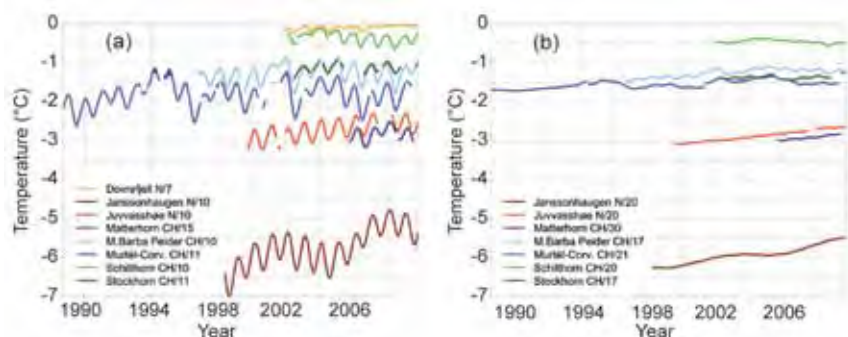
Fig. 2.28. Observed subsurface temperatures at (a) 10 m and (b) 20 m depth for selected boreholes in mountain permafrost: the sites of the PACE transect, the Matterhorn and M.d. Barba Peider sites in Switzerland, and Dovrefjell in Norway. Data for Swiss sites are provided by PERMOS, and for Norwegian sites by the Norwegian Meteorological Institute. [Modified from Haeberli et al. (2010, figure 4).]
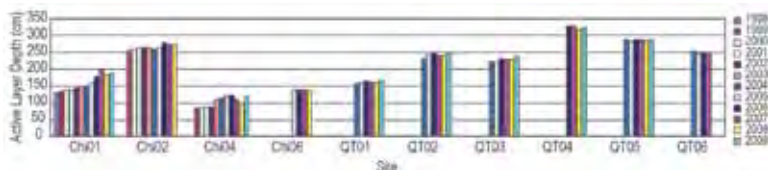
Fig. 2.29. Temporal trends in active layer depths along the Qinghai-Tibet Railway. [Modified from source: Zhao et al. (2010).]

the Northern Hemisphere for both permafrost temperatures and active layer depths. The latter respond to seasonal fluctuations in climate while changes of the deeper ground temperatures indicate long-term trends since shorter-term variations attenuate with depth. The deeper the temperatures are measured, the further back in time the surface temperature conditions they represent.

Permafrost generally warmed across the Northern Hemisphere during the past 20 to 25 years of the 20th century, and into the first few years of the 21st century (e.g., Romanovsky et al. 2007; Harris et al. 2003; Isaksen et al. 2007). Analyses of more recent data indicate that warming has generally continued. Permafrost temperatures are now up to 2°C warmer than they were 20 to 30 years ago although there are regional differences (Fig. 2.27). The overall range in permafrost temperature has decreased and is now about 1°C less than it was about 30 years ago in the polar Northern Hemisphere (Romanovsky et al. 2010b). Smaller warming rates are observed at temperatures close to 0°C compared to colder permafrost. This is especially true for ice-rich permafrost where latent heat effects dominate the ground thermal regime at temperatures close to 0°C (e.g., Romanovsky et al. 2010a; Smith et al. 2010), as well as for mountain regions in Europe where large permafrost areas are close to melting (PERMOS 2010; Haeberli et al. 2010; Isaksen et al. 2011). In European mountain permafrost, some 10-year records show a general warming trend (Isaksen et al. 2007; Haeberli et al. 2011) and permafrost temperature anomalies associated with extreme warm years (2003, 2009) have also been observed (Fig. 2.28; PERMOS 2010; Phillips et al. 2009; Zenklusen Mutter et al. 2010; Harris et al. 2003). However, trends are more pronounced in Scandinavia than in Central Europe, where only small changes or even cooling trends (Zenklusen Mutter et al. 2010) can be observed because of the strong influence of the snow cover and temperature ranges subject to latent heat effects. In the higher altitudes of Asia, ground temperatures have increased up to 0.5°C decade^{-1} since the early 1990s, accompanied by a general increase in active layer thickness (e.g., Zhao et al. 2010; Fig. 2.29). Although

the observed trends in permafrost temperatures are consistent with changes in air temperatures, other factors such as snow cover, soil properties (including ice and moisture content), and vegetation are important factors determining the magnitude of the changes in the ground thermal regime (e.g., Haeberli et al. 2010; Romanovsky et al. 2010b).

8) GROUNDWATER AND TERRESTRIAL WATER STORAGE—
    M. Rodell, D. P. Chambers, and J. S. Famiglietti
Most people think of groundwater as a resource, but it is also a useful indicator of climate variability and human impacts on the environment. Groundwater storage varies slowly relative to other non-frozen components of the water cycle, encapsulating long period variations and trends in surface meteorology. On seasonal to interannual timescales, groundwater is as dynamic as soil moisture (Rodell and Famiglietti 2001; Alley et al. 2002), and it has been shown that groundwater storage changes have contributed to sea-level variations (Milly et al. 2003; Wada et al. 2010).

Groundwater monitoring well measurements are too sporadic and poorly assembled outside of the United States and a few other nations to permit direct global assessment of groundwater variability. However, observational estimates of terrestrial water storage (TWS) variations from the GRACE satellites (see Sidebar 2.2) largely represent groundwater storage variations on an interannual basis, save for high latitude/altitude (dominated by snow and ice) and wet tropical (surface water) regions (Rodell and Famiglietti 2001).

Plate 2.1i maps changes in mean annual TWS from 2009 to 2010, based on GRACE, reflecting hydroclimatic conditions in 2010. Severe droughts impacted Russia and the Amazon, and drier-than-normal weather also affected the Indochinese peninsula, parts of central and southern Africa, and western Australia. Groundwater depletion continued in northern India (Rodell et al. 2009; Tiwari et al. 2009), while heavy rains in California helped to replenish aquifers that have been depleted by drought and withdrawals for irrigation, though they are still below normal levels (Famiglietti et al. 2011). Droughts in northern Argentina and western China similarly abated. Wet weather raised aquifer levels broadly across Western Europe. Rains in eastern Australia caused flooding to the north and helped to mitigate a decade-long drought in the south. Significant reductions in TWS seen in the coast of Alaska and the

The NASA/German Gravity Recovery and Climate Experiment (GRACE) was launched in March 2002. Rather than looking downward, GRACE continuously monitors the locations of and precise distance between twin satellites that orbit in tandem about 200 km apart. Variations in mass near Earth's surface cause heterogeneities in its gravity field, which in turn affect the orbits of satellites. Thus, scientists can use GRACE data to map Earth's gravity field with enough accuracy to discern month-to-month changes caused by ocean circulation and redistribution of water stored on and in the land (Tapley et al. 2004; Wahr et al. 2004). Sources of uncertainty include the inherent limitations of the measurement technique and instruments, issues associated with spatial resolution and mathematical representation of the gravity field, and inaccuracy in removing other gravitational influences, such as atmospheric circulation, post-glacial rebound, and solid earth movements, which are either independently modeled and removed or are assumed to be negligible on a monthly to sub-decadal timescales.

Despite its coarse spatial (> 150 000 km^2 at midlatitudes) and temporal (~monthly) resolutions, GRACE has enabled significant advances in oceanic, hydrologic, and cryospheric science, and has great potential for climate monitoring because it is the only global observing system able to measure ocean bottom pressures, total terrestrial water storage, and ice mass changes.

The best known GRACE results are estimates of Greenland and Antarctic ice sheet loss rates (Fig. 2.30). Previously, scientists had estimated ice mass losses using ground and satellite-based altimetry and surface mass balance estimates based on snowfall accumulation and glacier discharge. While such measurements are still very useful for their spatial detail, they are imperfectly correlated with large-scale ice mass changes, due to snow and ice compaction and incomplete spatial coverage. GRACE enables scientists to generate monthly time series of Greenland and Antarctic ice mass, which have confirmed the shrinking of the polar ice sheets, one of the most obvious and indisputable manifestations of climate change (e.g., Velicogna and Wahr 2006a, 2006b). Further, GRACE has located and quantified hot spots of ice loss in southeastern Greenland and western Antarctica (e.g., Luthcke et al. 2006). For 2002 to present, the mean annual rate of ice mass loss has been estimated between 200 Gt yr^{-1} and 300 Gt yr^{-1} in Greenland and between 70 Gt yr^{-1} and 210 Gt yr^{-1} in Antarctica, and some scientists are suggesting that the rates are accelerating (Velicogna 2009). Similarly, GRACE has been used to monitor mass changes in alpine glaciers. Tamisiea et al. (2005) first characterized glacier melt along the southern coast of Alaska, more recently estimated to be occurring at a rate of 84 ± 5 Gt yr^{-1} (Luthcke et al. 2008). Chen et al. (2007) estimated that Patagonian glaciers are melting at a rate of 28 ± 11 Gt yr^{-1}, and Matsuo and Heki (2010) estimated that the high mountains of central Asia lose ice at a rate of 47 ± 12 Gt yr^{-1}.

Tapley et al. (2004) and Wahr et al. (2004) presented the first GRACE-based estimates of changes in column-integrated terrestrial water storage (TWS; the sum of groundwater, soil moisture, surface waters, snow, ice, and water stored in vegetation) at continental scales. Since then, dozens of studies have shown that GRACE-based estimates of regional- to continental-scale TWS variations agree with independent information and some innovative uses of GRACE data have been developed. Rodell et al. (2004) and Swenson and Wahr (2006) demonstrated that by combining GRACE-derived terrestrial water storage changes with observations of precipitation and runoff in a river basin scale water budget, it was possible to produce new estimates of evapotranspiration and atmospheric moisture convergence, essential climate variables that are difficult to estimate accurately. Similarly, GRACE has been used to constrain estimates of global river discharge and the contribution of changes in TWS to sea-level rise (Seo et al. 2009; Syed et al. 2009, 2010). Crowley et al. (2006) observed a negative correlation between interannual TWS anomalies in the Amazon and the Congo River basin. Yeh et al. (2006) and Rodell et al. (2007) estimated regionally-
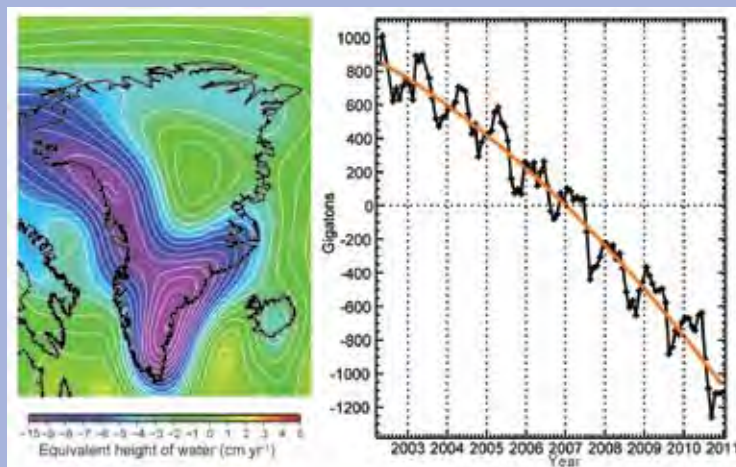
Fig. 2.30. (Left) Rate of ice sheet mass change (cm yr^{-1}, equivalent height of water) in Greenland from GRACE, April 2002–November 2010. (Right) Time series of Greenland total ice sheet mass (Gigatons) relative to the period mean.
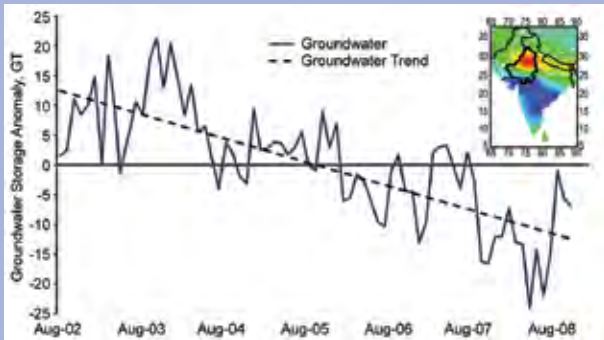
FIG. 2.31. Time series of groundwater storage in north-west India from August 2002 to October 2008 relative to the period mean. The inset panel shows areas of depletion in warm colors and areas of increase in cool colors, with the study region (the Indian states of Rajastan, Punjab, and Haryana) outlined in black. Based on data from Rodell et al. (2009).

averaged groundwater storage variations based on GRACE and auxiliary observations. Rodell et al. (2009) and Tiwari et al. (2009) applied that method to quantify massive ground-water depletion in northern India caused by over reliance on aquifers for irrigation (Fig. 2.31), and Famiglietti et al. (2011) found a similar situation in California's Central Valley. Zaitchik et al. (2008) and Lo et al. (2010) described approaches to use GRACE to constrain hydrological models, enabling integration of GRACE data with other observations and achieving much higher spatial and temporal resolutions than GRACE alone. Such approaches are now supporting applications including drought and water resources monitoring (Houborg and Rodell 2010; Bolten et al. 2010).

Oceanography has likewise benefitted from the inde-pendent nature of GRACE observations. One application is measurement of the mass component of sea-level rise, which complements radar altimetry and in situ measurements. GRACE also measures ocean bottom pressures (OBP), which help to refine understanding and modeling of ocean circulation and the ocean's fresh water budget, among other things (Fig. 2.32). Morison et al. (2007) used GRACE to describe impor-tant decadal-scale shifts in circulation and an ongoing trend of freshening of part of the Arctic Ocean, important indicators of climate variability. The research of Song and Zlotnicki (2008) and Chambers and Willis (2008) on GRACE-derived ocean bottom pressures in the subpolar gyre led to the discovery of an ENSO teleconnection and a long-term change in OBP in the North Pacific subpolar gyre that was not predicted by an ocean model. Further, Chambers and Willis (2009) were able to identify an interannual redistribution of mass between

oceans, which was not predicted by an ocean model and was the first direct evidence of sustained mass transport from one ocean basin to another on periods longer than a year. Boening et al. (2011) observed a record increase in OBP over part of the southeastern Pacific in late 2009 and early 2010, primarily caused by wind stress curl associated with a strong and persistent anticyclone and likely related to the concurrent central Pacific El Niño.

GRACE has far surpassed its five-year design lifetime, but it will likely succumb to the aging of batteries and instrument systems sometime in the next few years. NASA has begun initial development of a follow-on to GRACE with very similar design, which could launch as soon as 2016 and would provide con-tinuity in the data record while improving resolution slightly. Higher resolution time variable gravity missions are also on the drawing board (NRC 2007).
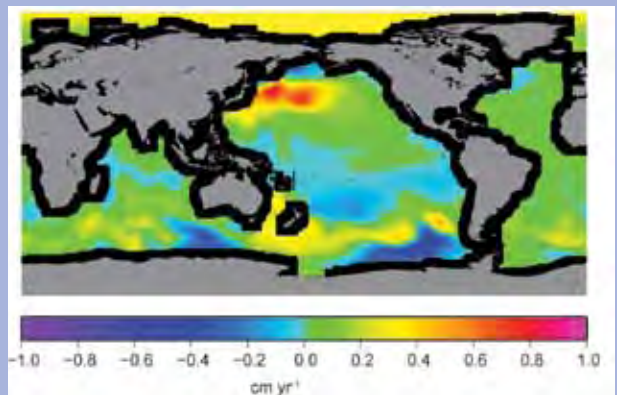
FIG. 2.32. Mean rate of change of ocean bottom pres-sure (cm yr^{-1} in equivalent sea level) from January 2003 to August 2010, computed from GRACE data projected onto empirical orthogonal functions (EOF) modes from a model (Chambers and Willis 2008). The large trends in the North Pacific, South Pacific, and Arctic are related to changing circulation and wind stress, and have been described by Chambers and Willis (2008), Boening et al. (2011), and Morison et al. (2007), respectively.
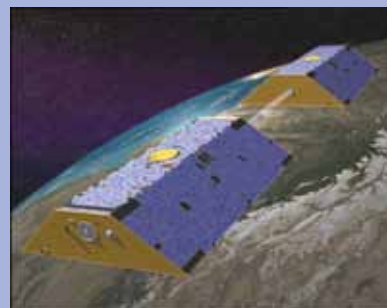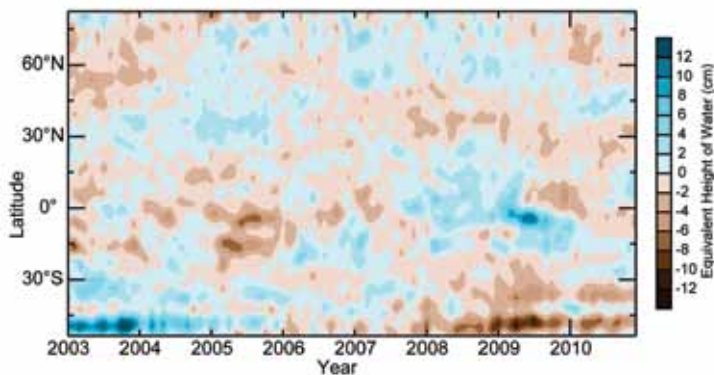

Image courtesy of NASA

FIG. 2.33. GRACE measurements of terrestrial water storage anomalies in cm equivalent height of water by latitude. The anomalies are relative to a base period of 2003–07. Gray areas indicate regions where data are unavailable.

Patagonian Andes represent ongoing glacier melt, not groundwater depletion.

Figures 2.33 and 2.34 plot time series of zonal mean and global GRACE derived non-seasonal TWS anomalies (deviation from the mean of each month of the year) excluding Greenland and Antarctica. The two figures show that terrestrial water storage in 2010 was the lowest since 2003, though it recovered in the second half of the year. The drought in the Amazon was largely responsible, but an excess of water in 2009 seems to have buffered that drought to some extent (Fig. 2.33). The drying trend in the 25°S–55°S zone is
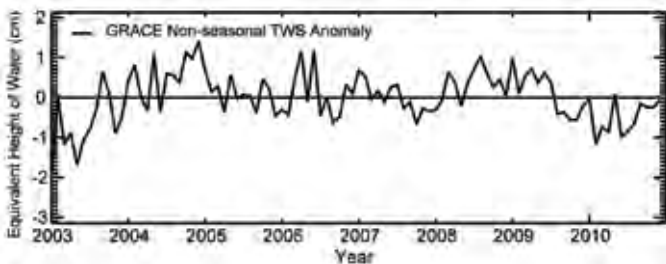
FIG. 2.34. Global average terrestrial water storage anomalies in cm equivalent height of water calculated using a 2003–07 base period.

a combination of Patagonian glacier melt and drought in parts of Australia.

9) Soil moisture—R. de Jeu, W. Dorigo, W. Wagner, and Y. Liu

In 2010, significant progress was made in consolidating globally available soil moisture datasets from a large number of ground-based stations and satellite platforms. Such harmonized datasets are essential for studying climate-related variability. Regarding the in situ component, the International

Soil Moisture Network (ISMN; Dorigo et al. 2011) was established as the successor of the renowned Global Soil Moisture Data Bank (Robock et al. 2000), which has been extensively used for climate studies. The ISMN offers a centralized system where historic and current in situ soil moisture measurements from around the world are collected, harmonized, and made available to users (see Table 2.1).

Satellite-based soil moisture estimates have significantly improved in recent years to the point where now several continental-to-global scale soil moisture products are available (e.g., Wagner et al. 2003; Njoku et al. 2003; Owe et al. 2008). These products represent moisture conditions in the top few centimeters and depend on observation wavelength and soil wetness (Schmugge 1985; Kuria et al. 2007). Due to different observation wavelengths and retrieval methods, the quality of these products varies. Scipal et al. (2008) and Dorigo et al. (2010), using a statistical method called triple collocation, quantified satellite-based soil moisture errors in the order of $0.01\ \mathrm{m^3\,m^{-3}}$–$0.04\ \mathrm{m^3\,m^{-3}}$ for the regions with a (semi) transparent vegetation cover, and $> 0.04\ \mathrm{m^3\,m^{-3}}$ for the more densely vegetated regions. Several studies have revealed that satellite-based products are highly correlated with in situ measurements (R between 0.6 and 0.8) with root mean square errors (RMSE) ranging between $0.03\ \mathrm{m^3\,m^{-3}}$ for semi arid regions (e.g., Africa and Australia) to $0.1\ \mathrm{m^3\,m^{-3}}$ in France (Gruhier et al. 2010; Draper et al. 2009; Rüdiger et al. 2009).

Satellite-based soil moisture products can provide reliable estimates over sparse to moderately vegetated regions. Current satellites are not yet able to monitor soil moisture variations over densely vegetated regions (e.g., tropical rainforests) because the signals received by satellites are severely disturbed by vegetation. Over regions with snow cover and frozen soils, satellite-based microwave instruments cannot provide reliable estimates either.

The historical microwave satellites have been used to compile a consistent 20-year record of global soil moisture (Liu et al. 2009, 2011; Su et al. 2010). Satellite-based soil moisture products from both passive and active instruments were collected and harmonized in one system, covering a period since January 1991, with a spatial resolution of 0.25° and a daily time step.
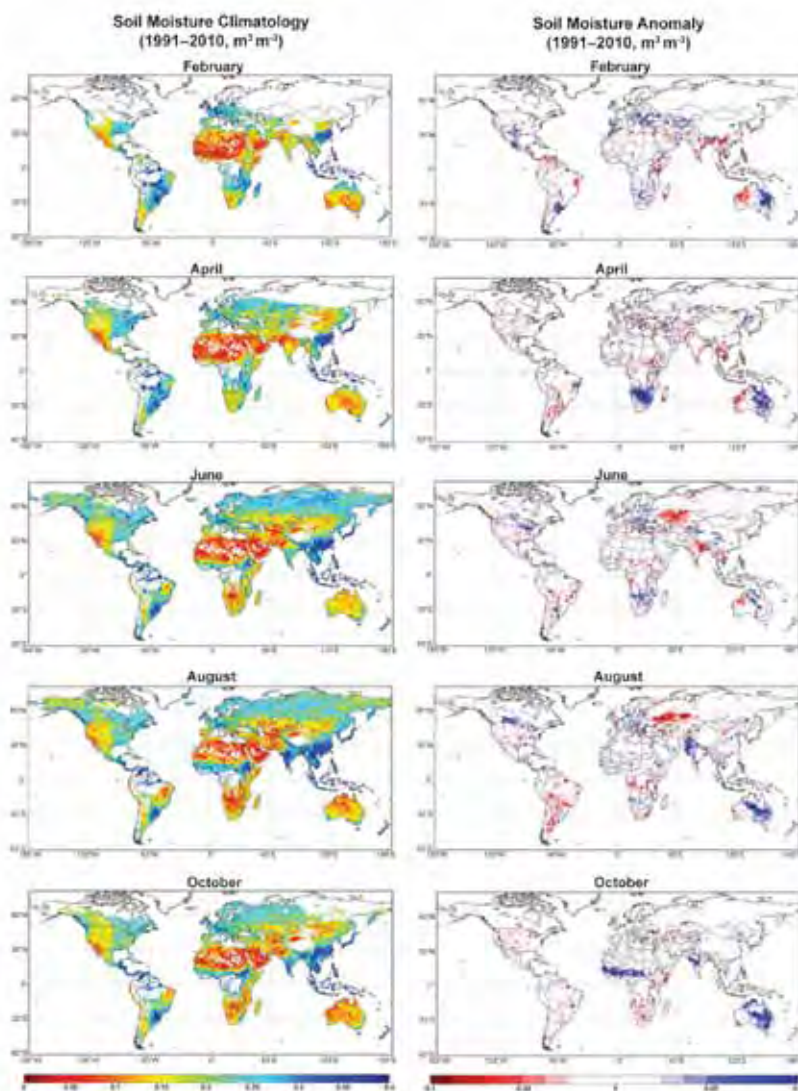
Fig. 2.35. Monthly soil moisture climatology (1991–2010) (left) and 2010 soil moisture anomaly (right) as derived from both passive and active microwave satellite sensors.

The monthly dynamics in global soil moisture are strongly driven by monsoonal circulations. During the winter phase of the monsoon, there is a low-level flow of dry, cool air from the cold continent to the warmer ocean, and precipitation over land is generally reduced. During the summer phase, there is a strong flow of atmospheric moisture from the cooler ocean to the warmer land, where the upward motion of the heated air produces the heavy rains of the monsoon season (Hastenrath 1985). These patterns are clearly visible in the soil moisture climatology (Fig. 2.35, left column). Over the Indian Peninsula, low soil moisture values between 0 m³ m⁻³ and 0.2 m³ m⁻³ are observed during February–April and high values between 0.2 m³ m⁻³ and 0.4 m³ m⁻³ are observed during August–

October. Over northern Australia, dry conditions are seen during June–August while wet conditions are seen during February–April. In Africa, the equatorial region near the Intertropical Convergence Zone is the wettest portion of the continent. Annually, the rain belt across the continent marches northward into Sub-Saharan Africa by August, then moves back southward into south-central Africa by March, resulting in wet soil moisture patterns in Sub-Saharan Africa in August and in south-central Africa in February–April.

A series of climatic events had a strong impact on the global distribution of precipitation and temperature in 2010, and these are reflected in the soil moisture anomalies (Fig. 2.35, right column). In February, both a wet (west) and dry (east) anomaly was detected over continental Australia. In April, south-central Africa was extremely wet due to excessive rainfall. In June, the first signs of the long, dry anomaly were detected over Russia and Kazakhstan. The anomaly lasted until the end of the summer. The hottest summer in Russia on record dried out a large area and led to several hundred wildfires in response (see Sidebar 7.8 for further details about this heat wave). In August, a wet anomaly was reflected over Pakistan, caused by extreme wet conditions and the additional flooding events (see section 7g3). The strong 2010 soil moisture anomalies from July onwards appear related to the oceanic phenomenon La Niña.

10) Lake levels—C. Birkett and J-F. Cretaux
Lake level as a climatic index was highlighted for the first time last year (Birkett 2010). Because lake volumes respond to changes in precipitation integrated over their catchment basins, they are indirect indicators of climatic change. The response can be seen in open lakes and reservoirs but is particularly marked for closed lakes, i.e., those having

no significant surface or subsurface outflow. Closed lakes can act as low-pass filters to variations in aridity, with a characteristic time constant of between 1 and 1000 years, depending largely on lake geomorphology (Birkett 2010). Deep lakes with steep shore topography are good proxies for high amplitude-low frequency changes, while shallow water basins are better indicators for rapid low-amplitude changes (Hostetler 1995).
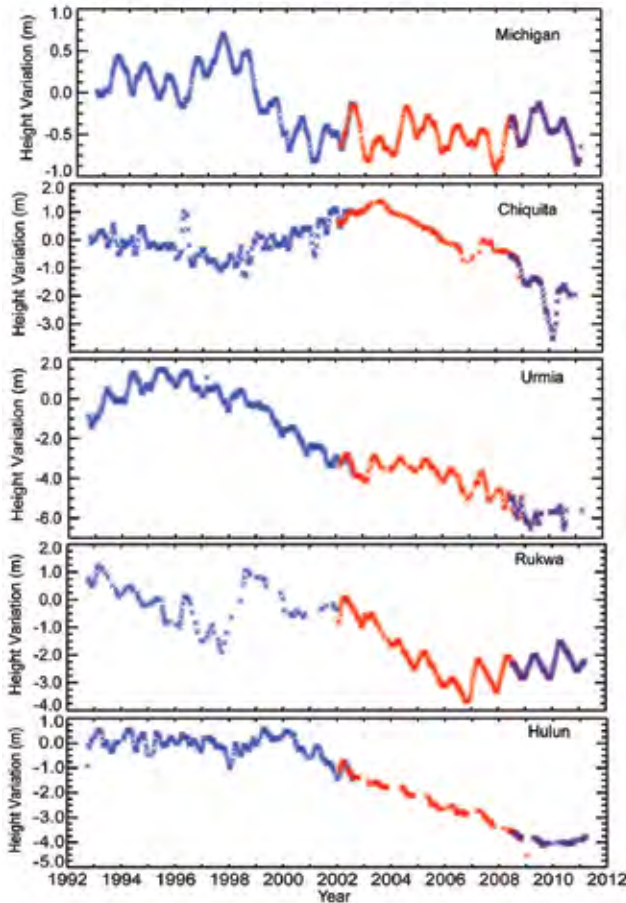
FIG. 2.36. (Top) Map showing the near real time lake level status of ~70 lakes with respect to a short-term mean (1992–2002). Red depicts low water drought and navy depicts high water. (Bottom) Examples of lake level time series for the United States (Michigan), Argentina (Chiquita), Iran (Urmia), Tanzania (Rukwa), and China (Hulun). (Courtesy of the USDA/FAS Crop-Explorer, http://www.pecad.fas.usda.gov/cropexplorer/global_reservoir/index.cfm.)

Lake variations can act as climate proxies with correlations to several modes of variability, e.g., ENSO, Indian Ocean, Pacific Decadal, or North Atlantic Oscillations (see Sidebar 1.1 for information about modes of variability). However, to date, studies have only been regional or individual in scope. Global analyses require the systematic monitoring of all global lake volumes. Satellite imagery could assist with the monitoring of changing lake surface area but currently no such products exist. Satellite-based radar altimetry does offer ~20-year lake level datasets which can stand alone or be combined with ground-based measurements (see Table 2.1). Satellite products have varying temporal/spatial resolutions and several centimeters accuracy at best (Fig. 2.36). Ground-based products can be found via local, state, or national agency web sites. Various lakes databases are also currently available that can assist with the identification of lake location and type (e.g., Lehner and Döll 2004; Fig. 2.37).

The NASA/USDA web site offers an indicative guide in terms of drought or high water (Fig. 2.36) but it is essential to build a global database that not only provides lake volume parameters (level, area) but includes or links to related, climatically sensitive measurements such as surface water temperature (section 2b4), air temperature (Smith et al. 2005; Liu et al. 2010), water salinity, ice cover duration and thickness (Karetnikov and Naumenko 2008; Mishra et al. 2011), and basin-scale water storage anomalies (e.g., Becker at al. 2010). The type of lake included should be challenged to encompass existing, emerging, and ephemeral high latitude lakes, including supraglacial (Box and Ski 2007; Bagshaw et al. 2010), and subglacial (Fricker et al. 2007; Smith et al. 2009) in the light of recent research.
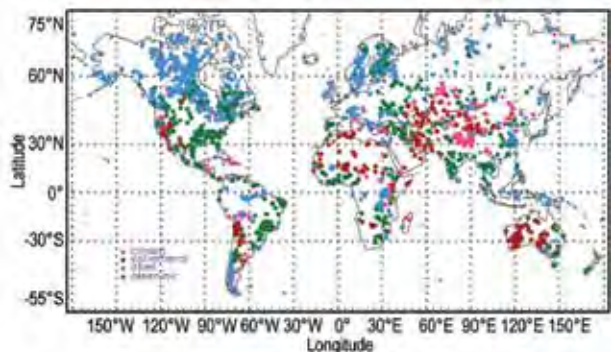
FIG. 2.37. Global location of large (≥ 100 km²) lakes; closed (pink), ephemeral (red), open (blue), and reservoirs (green). Based on Birkett and Mason (1995).
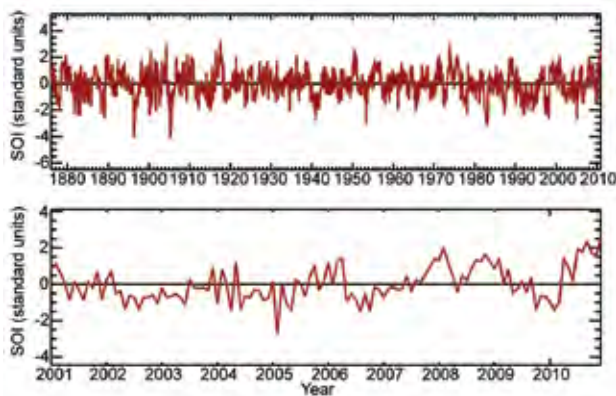
FIG. 2.38. The Australian Bureau of Meteorology Southern Oscillation Index time series for (top) 1876 to 2010 and (bottom) from 2001 to 2010 relative to the 1879–2010 average. Data for HadSLP2r (Allan and Ansell 2006) are shown.

d. Atmospheric Circulation

1) MEAN SEA LEVEL PRESSURE—R. Allan

In 2010, El Niño conditions gave way to La Niña, with a major event having developed by the latter part of the year. Indications are that it could be one of the strongest La Niña events in the historical instrumental record, with major precipitation and temperature impacts across the Indo-Pacific region and at higher latitudes in both hemispheres. Record positive Southern Oscillation Index (SOI) measurements were reached for March (since records began in 1876) and April (since 1971) according to the Australian Bureau of Meteorology (http://www.bom.gov.au/climate/enso/).

El Niño and La Niña can be quantified by the SOI—the normalized mean sea level pressure (MSLP) difference between Tahiti and Darwin (Allan et al. 1996). Other indices, using sea surface temperatures, are also commonly utilized (see Sidebar 1.1). El Niños (negative SOI) and La Niñas (positive SOI) vary in magnitude, duration, and evolution, with no two events or episodes exactly the same. The SOI since 1900 is dominated by interannual to multidecadal vacillations, but longer-term trends are not evident (Fig. 2.38, top). The SOI trace since 2000 highlights the shift from the La Niña of 2007/08 through the El Niño of 2009/10 to the moderate-to-strong La Niña of 2010/11 (Fig. 2.38, bottom). Major El Niño and La Niña events can be near-global in their influence on world weather patterns, owing to ocean-atmosphere interactions across the Indo-Pacific region with teleconnections to higher latitudes in both hemispheres.
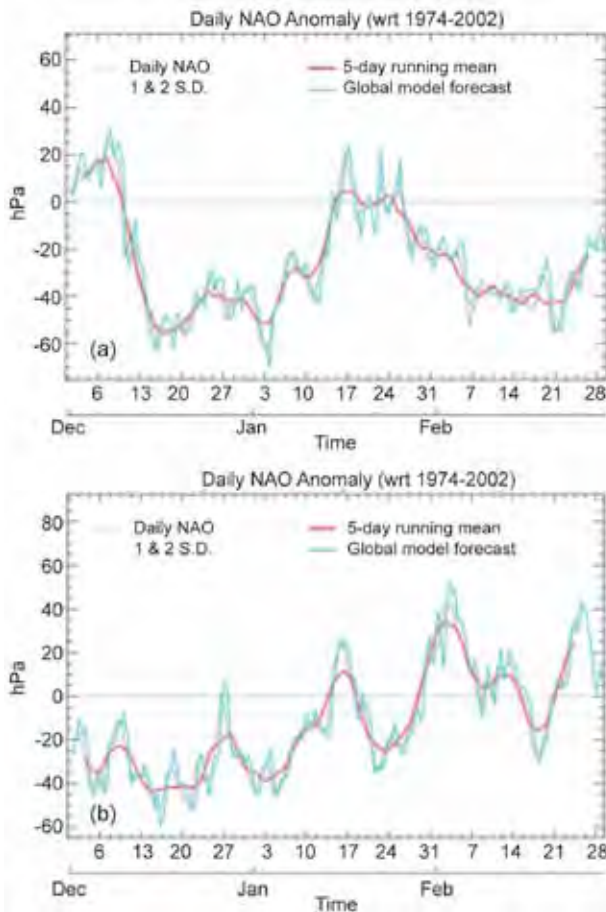
The Northern Hemisphere winters of 2009/10 and 2010/11 were dominated by long periods of extremely negative North Atlantic Oscillation (NAO)/Arctic Os-
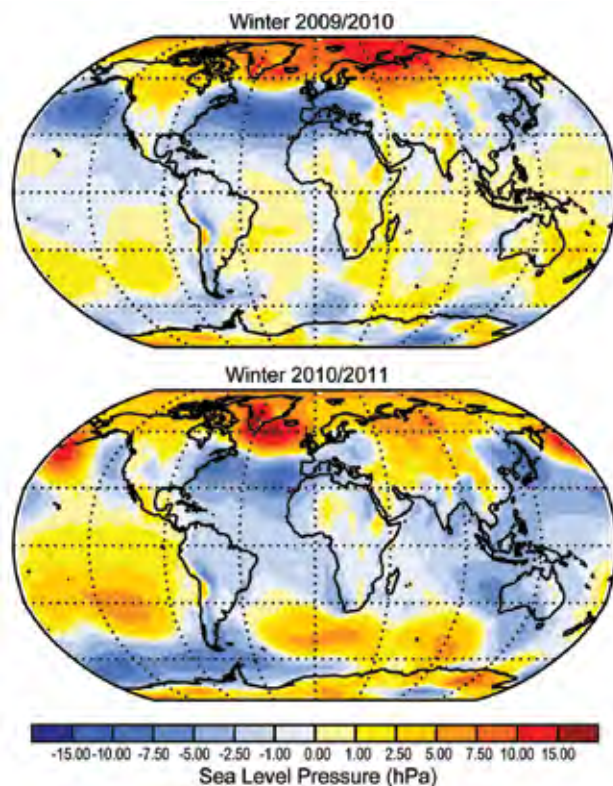
FIG. 2.39. Winter sea level pressure anomalies (1961–90 base period) averaged over Dec–Feb for (top) 2009/10 and (bottom) 2010/11. The data shown are from Had-SLP2r.

cillation (AO) conditions (Fig. 2.39, top and bottom). There were positive pressure anomalies over higher latitudes and negative anomalies over the midlatitudes and an associated reduction in westerlies. This is further evident in Fig. 2.40 (top and bottom), where periods of negative observed and modeled daily and five-day northern NAO/AO values for December 2009–February 2010 and December 2010–January 2011, respectively, highlight the major snow and cold temperature events across parts of Europe in the last two boreal winters.

In the Southern Hemisphere, the latter half of 2010 experienced one of the strongest periods of positive values of the Antarctic Oscillation (AAO)/Southern Annual Mode (SAM; the Antarctic counterpart to the AO) observed in the historical record (see Sidebar 1.1 and section 6b for further details). The combination of both a strong and positive AAO/SAM and SOI (reflecting the moderate-to-strong La Niña) has been suggested as leading to the above-average levels of Antarctic sea-ice observed in the last four months of 2010 (NSIDC, 5 January 2011: http://nsidc.org/arcticseaicenews/).

FIG. 2.41. Global average surface windspeed anomalies over ocean shown for the SSM/I and AMSR-E combined monthly smoothed observations (1988–2007 base period) and six reanalyses annual products (1989–2008 base period for all except ERA-40 which uses 1961–90). All time series are adjusted to have a mean of zero over the common period 1989–2001 to aid comparison. The extent to which inhomogeneities in the observations assimilated by the reanalyses, arising from changes in measurement systems, impact the accuracy of the analyzed surface winds is not yet known.

FIG. 2.40. The North Atlantic Oscillation Index is shown for winter (top) 2009/10 and (bottom) 2010/11 using station data (red) and the Met Office Global Model forecast (blue). (Courtesy of the UK Met Office Hadley Centre.)

2) OCEAN SURFACE WIND SPEED—C. Mears

Surface wind speed over the world's oceans began to be monitored continuously with the launch of the first Special Sensor Microwave Imager (SSM/I) satellite in late 1987. The SSM/I instrument is a microwave radiometer that makes measurements of upwelling microwave radiation to infer the surface roughness of the world's oceans, and thus the surface wind speed (Wentz 1997). Since the first SSM/I instrument, a number of additional microwave imaging sensors, including the Advanced Microwave Scanning Radiometer-EOS (AMSR-E) and Windsat have been launched and intercalibrated to the accuracy necessary for climate studies (Wentz et al. 2007). Globally-averaged winds from satellite-borne radiometers and six reanalysis datasets are plotted in Fig. 2.41. Some reanalysis-generated winds (see Sidebar 2.1) show much less variability than the satellite data (NCEP CFSR, ERA-40), while others show more variability and greater long-term changes. A further complica-

tion is that surface wind speed over the oceans is dominated by short-term variability and regional character (Fig. 2.42), making it difficult to discern long-term trend behavior.

Winds in the tropics, especially the central tropical Pacific, were above normal in 2010, as the tropical Pacific transitioned to La Niña. Negative wind anomalies in the Atlantic around 55°N coincided with the strong negative phase of the North Atlantic Oscillation (Hurrell et al. 2003) during most of 2010.
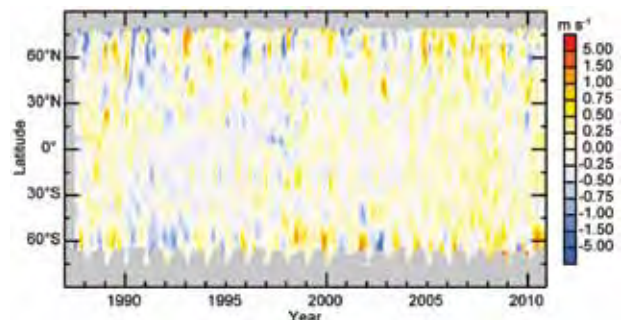
**FIG. 2.42. SSM/I and AMSR-E combined smoothed monthly average surface ocean wind speed anomalies (1988–2007 base period) by latitude for the period June 1987 to December 2010. Gray areas indicate regions where data are unavailable.**

Positive wind anomalies in the South Pacific and Indian Oceans near 55°S are correlated with the intensification of the Southern Annular Mode (Hall and Visbeck 2002) during 2010 (Plate 2.1k).

\

Wind speed and direction have been observed at many thousands of stations around the world. These data are regularly transmitted on an hourly or synoptic basis. Figure 2.43 shows the annual mean wind speed at 11 853 stations with at least five years of data since 1979 from the Integrated Surface Database (ISD-Lite; Lott et al. 2008) hosted at NOAA's National Climatic Data Center (NCDC). While such analysis offers guidance on where to install wind-energy generators, wind data have a variety of problems that limit their usefulness in climate change analysis.
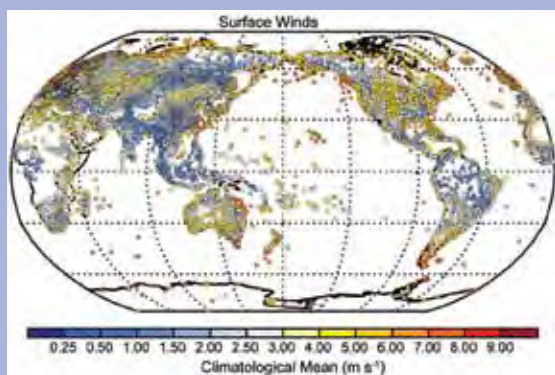
FIG. 2.43. Observed mean wind speed at 11 853 stations with at least five years of observations in Lott et al. (2008) between 1979 and 2010.

These problems include limited periods of record and missing data, due to either operations at a station or data transmission. They also include breaks in time series due to station moves, exposure changes due to modification in nearby obstacles, as well as instrument, observation protocol, or units changes. For instance, new instruments are often more sensitive to very light breezes and therefore have fewer observations of zero wind speed.
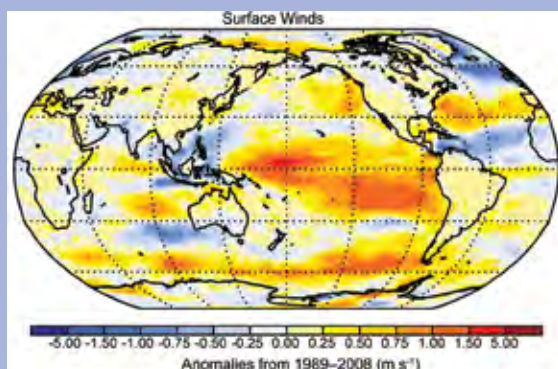

FIG. 2.44. 2010 wind speed anomalies from ERA-Interim reanalysis. Note that the base period used here (1989–2008) differs slightly from that used in Plate 2.1k (1988–2007).

Therefore, to accurately assess wind speed anomalies and particularly trends, careful attention must be paid to the homogeneity of station time series. This was done by Vautard et al. (2010) and McVicar et al. (2008). Their homogeneous wind data, with updates to McVicar et al. (2008) provided by data in Lott et al. (2008), allows an assessment of station wind anomalies for 2010 (Plate 2.1k), but with less than 10% of the stations shown in Fig. 2.43. These data were stitched onto the time series using a First Difference approach to avoid creating discontinuities at the transition (Peterson et al. 1998; Free et al. 2004). For complete global coverage of 2010 wind anomalies, one can use reanalysis (Fig. 2.44).

Observed wind speed over much of the global land areas, as shown in Fig. 2.45, tends to be decreasing (e.g., Roderick et al. 2007). Yet mean reanalysis wind speed does not show this decrease (Fig. 2.46). The difference is hypothesized to be at least partly due to increases in surface roughness associated growth of vegetation over much of the region with adequate long-term observations (Vautard et al. 2010; McVicar and Roderick 2010). These land-surface changes are currently not fully represented in present-day reanalysis systems and it is unclear how roughness changes near observing sites can be translated to higher elevation sites that are important for wind energy.
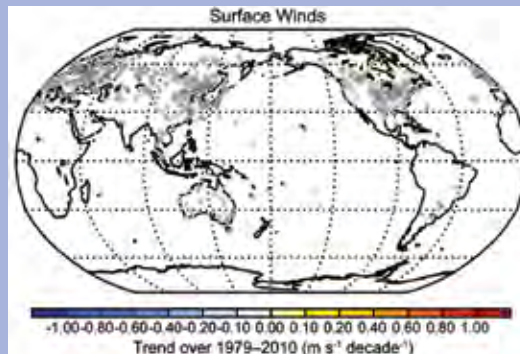
FIG. 2.45. Observed trends in wind speeds at locations with long and fairly homogeneous data records.
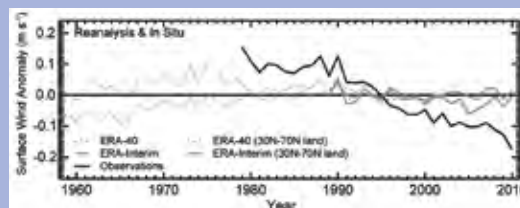

FIG. 2.46. Global average wind speed anomalies over land from reanalysis and observations. The green curves display the wind speed anomalies over land restricted to 30°N–70°N from reanalyses (corresponding to the area covered by the bulk of surface observations). The base period for the anomalies is the 1989–2001 period of overlap from all three datasets.

e. *Earth radiation budget at top-of-atmosphere*—D. P. Kratz, P. W. Stackhouse, Jr., T. Wong, P. Sawaengphokhai, A. C. Wilber, and N. G. Loeb

The net radiation at the top of the atmosphere provides an estimate of the balance between the incoming shortwave flux from the sun with the outgoing reflected shortwave and emitted longwave fluxes from the Earth-atmosphere. Analyses of the Clouds and Earth's Radiant Energy System (CERES; Wielicki et al. 1998) instrument data taken aboard the Terra spacecraft revealed that between 2009 and 2010 the global-annual mean outgoing longwave radiation (OLR) increased by ~0.40 W m^{-2} and the reflected shortwave radiation (RSW) increased by ~0.60 W m^{-2} (Table 2.4). Data from the Solar Radiation and Climate Experiment (SORCE; Kopp et al. 2005) indicated that the annual average total solar irradiance (TSI) also increased by ~0.10 W m^{-2} from 2009 to 2010. Thus, the changes in the combined global-annual averaged OLR and absorbed shortwave (TSI minus RSW) fluxes resulted in a reduction of ~0.90 W m^{-2} in total net radiation into Earth's climate system for 2010 as compared with 2009. The data between July 2010 and December 2010, however, may include modest instrument drift artifacts (below ±0.1%), since the final instrument calibration coefficients for those months are not yet available. Relative to the multiyear dataset average for 2001–09, the 2010 global-annual mean anomaly (Table 2.4) is +0.00 W m^{-2}/+0.50 W m^{-2}/-0.55 W m^{-2} for OLR/RSW/total net radiation, respectively. These results are comparable to the corresponding 2-sigma interannual variability for this period.

Global-monthly mean deseasonalized anomalies since March 2000 have been produced by merging Earth Radiation Budget (ERB) datasets from two
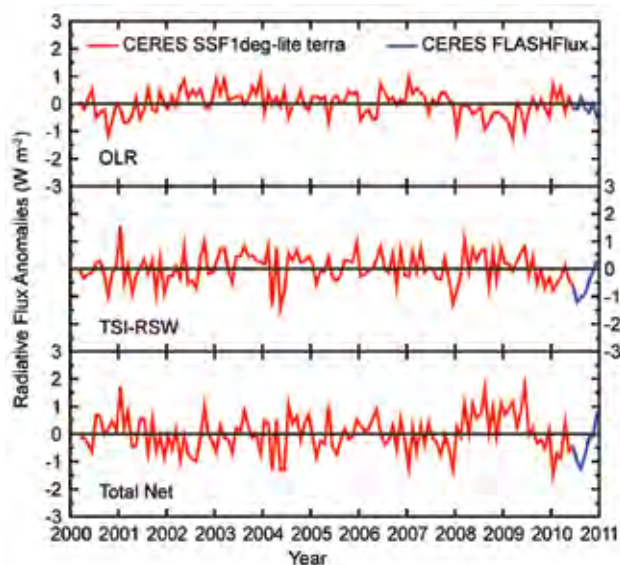
Fig. 2.47. **Global average monthly mean deseasonalized anomalies of top-of-atmosphere earth radiation budget for outgoing longwave radiation (upper panel), absorbed shortwave (TSI minus RSW) (middle panel), and total net (TSI minus RSW minus OLR) (lower panel) from Mar 2000 to Dec 2010. Anomalies are computed relative to the calendar month climatology derived for the Mar 2000 to Dec 2010 period. The time series shows the CERES SSF 1Deg Lite Ed2.5 data (Mar 2000 to Jun 2010) by a red line, and the CERES FLASHFlux data (Jul 2010 to Dec 2010) by a blue line. Mean differences between datasets were removed using available data from the overlap period from Mar 2007 through Feb 2010 and the absolute value of the CERES SSF 1Deg Lite results before deseasonalization (see Table 2.1 for source information).**

sources: (1) the CERES SSF (Single Scanner Footprint) 1x1 Degree Lite [SSF 1Deg Lite Ed2.5 Top-of-Atmosphere (TOA) only version] using the Edition 3 instrument calibration, and (2) the CERES Fast Longwave and Shortwave Radiative Fluxes (FLASHFlux) product (Stackhouse et al. 2006; L'Ecuyer et al. 2008). The results are presented in Fig. 2.47, where the FLASHFlux data have been normalized to the SSF 1Deg Lite data using TOA fluxes from both datasets for the three-year period from March 2007 though February 2010. The 2-sigma monthly uncertainty from this overlap period was ±0.55 W m^{-2}/±0.50 W m^{-2}/±0.70 W m^{-2} for the OLR/RSW/total net radiation, respectively. The OLR showed a general, albeit somewhat irregular,

Table 2.4. Global-annual mean Top-of-Atmosphere radiative flux changes between 2009 and 2010, the 2010 global-annual mean radiative flux anomalies relative to their corresponding 2001-10 mean climatological values, and the 2-sigma interannual variabilities of 2001–10 global-annual mean fluxes (units in W m^{-2}) for the outgoing longwave radiation (OLR), total solar irradiance (TSI), reflected shortwave (RSW) and total net fluxes. All flux values have been rounded to the nearest 0.05 W m^{-2}.

	One year change (2010 minus 2009)	2010 anomaly (relative to climatology)	Interannual variability (2001 to 2010)
OLR	0.40	0.00	±0.55
TSI	0.10	-0.05	±0.20
RSW	0.60	0.50	±0.50
Net	-0.90	-0.55	±0.70

downward oscillation from late 2009 throughout 2010. Changes in the absorbed shortwave (TSI minus RSW) showed a significant decrease in the first several months, followed by a reversal of that decrease in the latter half of 2010. Although dominated by the RSW, the relative month-to-month level of the absorbed shortwave was raised by the recovery of the TSI after a prolonged minimum stretching back to late 2007. The combined OLR and absorbed shortwave resulted in a minimum in the total net TOA flux at midyear, with a recovery to levels at the end of 2010 comparable to the beginning of the year. A smoothed version of the averaged TOA OLR showed a general agreement in fluctuations with a similarly smoothed multivariate ENSO index, where the index peaked positively at the beginning of 2010 before falling. Thus, the change in the ENSO intensity appears to influence strongly the global averaged monthly TOA variability during this time period. Finally, the dynamic nature of the OLR and RSW between 2009 and 2010 produced one-year changes that were comparable to the 2-sigma interannual variability. Further fluctuations are anticipated as the ENSO cycle evolves. Thus, long-term trend analyses are discouraged due to the natural fluctuation in ERB relating to ENSO activity in the short record, the large uncertainty from the data merging process, and instrument drift potential in the FLASHFlux data. A long-term homogeneous data source with in-depth instrument stability analysis is required to reduce uncertainties in future reassessment activity.

f. Atmosphere composition

1) ATMOSPHERIC CHEMICAL COMPOSITION

(i) Carbon dioxide, methane, and carbon monoxide— E. J. Dlugokencky

(A) CARBON DIOXIDE

The contribution of carbon dioxide (CO_2) towards Earth's total terrestrial greenhouse effect is 20%, with non-CO_2 greenhouse gases (GHG; 5%), water vapor (50%), and clouds (25%) comprising the remainder (Lacis et al. 2010). During the past few decades, most of the increase in the atmospheric burden of CO_2 (Fig. 2.48a) has been due to fossil fuel combustion. This is known from multiple lines of observational evidence (Tans 2009). Measurements of atmospheric CO_2 at Mauna Loa, Hawaii, and the South Pole show that the north to south difference is increasing, consistent with increasing CO_2 emissions from fossil fuel combustion, predominantly in the Northern Hemisphere. Strong evidence also comes from measurements of tracers such as ^{14}C in CO_2, which is decreasing as

a result of adding CO_2 from fossil fuel combustion (depleted of ^{14}C), ^{13}C in CO_2, which shows that the added CO_2 is of organic origin, and measurements of a decrease in the ratio of O_2:N_2, which is also consistent with O_2 consumption by fossil fuel combustion. The current rate of increase in atmospheric CO_2 is exceptional when compared to changes on geological time scales, as assessed from measurements of air trapped in ice cores.

Despite the long-term trend in atmospheric CO_2 being driven by fossil fuel emissions, interannual variability in the rate of increase of atmospheric CO_2 is driven by small changes in the net fluxes between the atmosphere and terrestrial biosphere and the atmosphere and oceans. During 2010, globally averaged atmospheric CO_2 at Earth's surface increased by 2.60 ± 0.07 ppm (see Conway et al. 1994 for a description of sampling network and methods); uncertainty 1
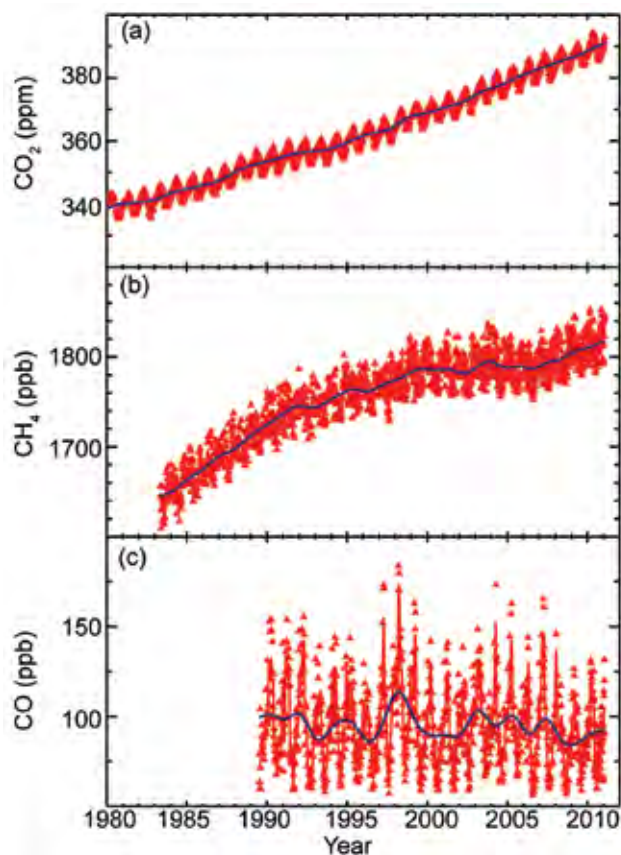
FIG. 2.48. Mixing ratios (dry air mole fraction) of (a) CO_2, (b) CH_4, and (c) CO from measurements of discrete air samples collected approximately weekly at NOAA's Mauna Loa observatory. Symbols are the average of two samples collected in series. Red lines are smooth curves fitted to the data. Blue lines are deseasonalized trend curves.

standard deviation. This is greater than the average rate of increase from 1980 through 2010 of 1.69 ± 0.58 ppm yr^{-1}. It is also larger than the increase in 2009 of 1.62 ± 0.07 ppm.

(B) METHANE

After a decade of near-zero growth, atmospheric methane (CH_4) increased globally in 2007 and 2008 by ~7.5 ppb yr^{-1} (Rigby et al. 2008; Dlugokencky et al. 2009). Bousquet et al. (2010) used two different inversion models to estimate changes in emissions and sinks during 2006 to 2008 and found that global CH_4 emissions exceeded the 1999–2006 average by 19 Tg CH_4 (16 Tg–21 Tg) in 2007 and 13 Tg CH_4 (6 Tg–20 Tg) in 2008. Changes in tropical wetland emissions were the dominant driver in 2007, with a minor contribution from Arctic wetlands. Although the inversion models gave inconsistent results for 2008, the global vegetation model used by Bousquet et al. (2010) implied a tropical source for the excess methane. Bousquet et al. (2010) found that changes in hydroxyl (OH) radical concentrations, the primary oxidant for CH_4, were less than 1%, and had only a small impact on observed CH_4 changes. During both 2009 and 2010 (Fig. 2.48b), globally averaged atmospheric CH_4 provisionally increased by $~5 \pm 2$ ppb yr^{-1}; the causes of this continued increase are not yet known, but it is likely related to increasing emissions from rapidly developing economies in Asia.

(C) CARBON MONOXIDE

Carbon monoxide (CO) is a key species in atmospheric chemistry, particularly in cycling of reactive species like the hydroxyl (OH) and hydroperoxyl (HO_2) radicals. The four major sources of CO to the atmosphere are: biomass burning, mostly from forest clearing and savannah burning in the tropics; combustion of fossil fuels; atmospheric oxidation of natural volatile organic compounds; and atmospheric oxidation of CH_4. There has been no significant long-term CO trend since NOAA/ESRL measurements began in 1990 (Novelli et al. 2003), but CO anomalies occurred during 1997 to 1998, and again in 2002 to 2003 (Fig. 2.48c). These anomalies are likely the result of interannual variability in the rates of tropical and boreal biomass burning (section 2g3). Since the lifetime of CO is only a few months, the CO enhancements quickly disappeared. The preliminary globally averaged CO mole fraction in 2010 is ~83 ppb, slightly larger than in 2009.

(ii) Nitrous oxide and sulfur hexafluoride—J. W. Elkins and G. S. Dutton

Atmospheric nitrous oxide (N_2O) and sulfur hexafluoride (SF_6) have significant man-made sources and are two of six gases selected for emission reduction under the Kyoto Protocol of the United Nations Framework Convention on Climate Change. Atmospheric N_2O currently has the third strongest climate forcing of the long-lived trace gases after carbon dioxide (CO_2) and methane (CH_4), recently surpassing chlorofluorocarbon (CFC)-12, and is considered a major greenhouse gas (Forster et al. 2007; Hofmann et al. 2006).

Current emissions of nitrous oxide are expected to contribute more to future ozone depletion than current emissions of halogenated ozone-depleting substances (ODS) (Ravishankara et al. 2009). Nitrous oxide is produced naturally by both the oxidation of ammonium and the denitrification of nitrate. Significant emissions of nitrous oxide occur during the application of nitrogen fertilizers on agricultural crops (Davidson 2009). This, along with other anthropogenic sources, contribute to an almost 30% imbalance in the budget of atmospheric N_2O, where the global growth rate has averaged 0.75 ± 0.01 ppb yr^{-1}
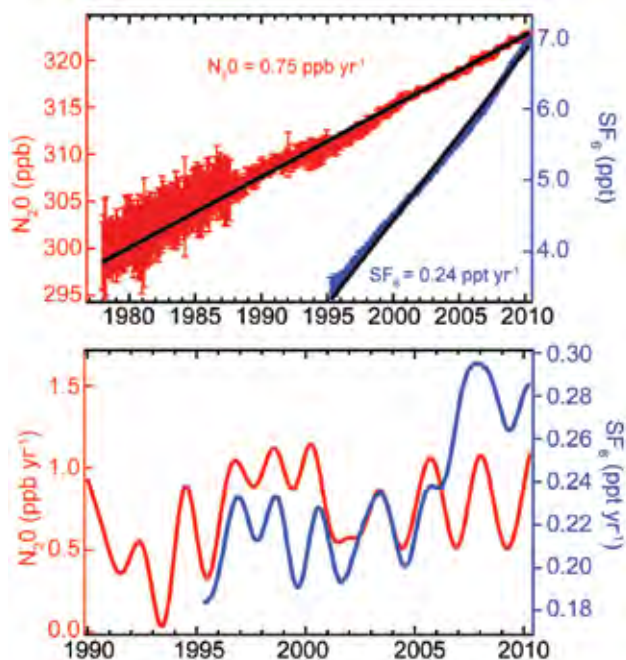
FIG. 2.49. (Top) Global monthly mean mixing ratios of N_2O (red) and SF_6 (blue) with estimates for the linear growth rate from NOAA/ESRL in situ and flask observations, and (bottom) instantaneous growth rates of N_2O and SF_6 derived using a Fast Fourier Transform smoothing algorithm (Thoning et al. 1989) with a two year filter.

since 1977 (Fig 2.49). However, the observed growth rate of N_2O exhibits interannual variability, some of which may be the result of limited global sampling and changes in atmospheric transport (Fig. 2.49, bottom). The mean global atmospheric N_2O mixing ratio for 2010 was 323.16 ± 0.21 ppb. On average, global N_2O concentrations between the two major global networks, NOAA and the Advanced Global Atmospheric Gases Experiment (AGAGE), agree to within 0.2 ppb (Huang et al. 2008).

Sulfur hexafluoride (SF_6) is an important greenhouse gas because it has one of the strongest global warming potentials of all trace gases—23 900 times greater than carbon dioxide (CO_2) with a 100-year time horizon and a very long atmospheric lifetime of 3200 years (Solomon et al. 2007). Sulfur hexafluoride is primarily used as a dielectric insulator for transmission of electricity and emissions are entirely anthropogenic. Its global average concentration for 2010 was 7.02 ± 0.05 ppt (Fig. 2.49, top). The average linear growth rate has been 0.24 ± 0.01 ppt yr^{-1} since 1995. The global atmospheric growth rate increased after 2006 from a mean of 0.22 ± 0.01 ppt yr^{-1} to 0.28 ± 0.02 ppt yr^{-1} (Fig. 2.49, bottom). The increase in emissions could be the result of new electrical capacity in Southeast Asia (Rigby et al. 2010). The decline in the growth rate noted in last year's report appears to have been short-lived. Data from the two networks generally agree very well for atmospheric SF_6, with a mean bias (NOAA minus AGAGE) of around +0.02 ppt with a standard deviation of 0.05 ppt determined from coincident measurements (Rigby et al. 2010). Currently, the global radiative forcing due to SF_6 is small; however, its rapid growth rate (4% per year), high global warming potential, and long atmospheric lifetime mean that SF_6 could contribute significantly to climate forcing by the end of the century.

(iii) Changes in atmospheric abundances of ozone-depleting gases and their replacements—S. A. Montzka and G. Dutton

Long-lived halocarbons affect the radiative balance of the atmosphere because they efficiently absorb terrestrial IR radiation (section 2f1v). Long-lived halocarbons containing bromine (Br) and chlorine (Cl) also influence the radiative atmospheric balance indirectly through their destruction of stratospheric ozone. Because of concern over stratospheric ozone depletion, production of many halocarbons has been restricted in recent years through amendments and adjustments to the 1987 Montreal Protocol on Substances that Deplete the Ozone Layer. As a result, mixing ratios of most of the potent ozone-depleting gases have been declining at Earth's surface; this decline continued in 2010 (Fig. 2.50).

The NOAA/ESRL data show that mixing ratios of some halogenated gases continue to increase globally
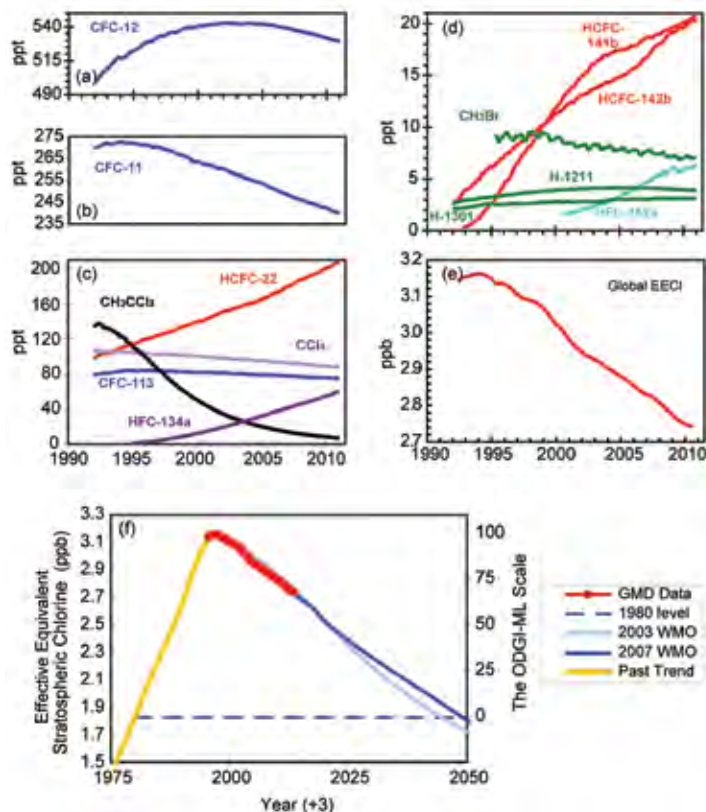
FIG. 2.50.(a, b, c, d) Atmospheric abundances (global mean tropospheric mixing ratios, dry air mole fraction) of the most abundant CFCs, HCFCs, HFCs, chlorinated solvents, and brominated gases, (e) changes in atmospheric Equivalent Effective Chlorine (EECl; ppb), and (f) recent changes in Equivalent Effective Stratospheric Chlorine (EESC; ppb) observed by the NOAA/ESRL global network relative to the secular changes observed in the past, including the level observed in 1980 when the ozone hole was first observed, and a projected future through 2050 (Daniel et al. 2010). EECl is derived as the sum of [Cl + (Br •60)] from observed mixing ratios of ozone-depleting substances appearing in the other four panels. EESC is derived from EECl here by adding three years to the time axis to represent the lag associated with mixing air from the troposphere to the middle stratosphere, where the ozone layer resides. The Ozone Depleting Gas Index for midlatitudes (ODGI-ML) is derived (right hand axis) from rescaling EESC. [Source: Montzka et al. (1996, 1999)]

(Fig. 2.50c,d). The most rapid increases are observed for hydrochlorofluorocarbons (HCFCs) and hydrofluorocarbons (HFCs), which are common replacements for chlorofluorocarbons (CFCs), halons, and other ozone-depleting gases. Increases in HCFCs have recently accelerated owing to enhanced use in developing countries (Montzka et al. 2009). Both HCFCs and HFCs are efficient absorbers of infrared radiation (Table 2.5). While HCFCs contain chlorine and deplete ozone with a reduced efficiency compared to CFCs, HFCs do not participate in ozone-destroying reactions.

Future levels of ozone-depleting halogens in the stratosphere (and, therefore, the threat to stratospheric ozone) can be estimated from weighted sums of Cl and Br in long-lived halocarbons, accounting for the enhanced efficiency for Br to destroy ozone [a factor of 60 is used here (Montzka et al. 2011)]. These sums are derived from surface-based measurements and are expressed as Equivalent Effective Chlorine (EECl; Fig. 2.50e) or Equivalent Chlorine (ECl), depending on if weightings are chosen to be relevant for the midlatitude (EECl) or polar stratosphere (ECl). EECl, for example, provides an estimate of the near-future ozone-depleting power of trace gases, i.e., once air at Earth's surface becomes mixed into the midlatitude stratosphere. An additional metric, Equivalent Effective Stratospheric Chlorine (EESC), provides an estimate of the ozone-depleting power of trace gases in the stratosphere and is often derived from EECl or ECl with the addition of a time lag owing to transport.

The EECl content of the lower atmosphere has declined fairly steadily through 2010 at a mean rate of 27 ppt yr^{-1} since the peak in 1994 (Fig. 2.50e). Despite these substantial changes, full recovery of stratospheric ozone is not expected until the middle to latter part of the 21st century owing to the long lifetimes of many of these chemicals (Table 2.5). A similar conclusion can also be drawn from measurements of trace gases obtained by the AGAGE group. Both NOAA and AGAGE measurements show similar trends in EECl in recent years (Montzka et al. 2011). Progress towards EECl reductions can now be readily assessed with the NOAA Ozone-Depleting Gas Index (ODGI; see Table 2.1; Hofmann and Montzka 2009). This index is derived from EECl (Fig. 2.50f). It is scaled so that a value of 100 represents the EECl (or EESC) abundance at its peak, and zero represents the 1980 level (a reference point during which ozone depletion was thought to have been small). In 2010, the ODGI-Midlatitudes was 67.1. Less progress is evident for the index when the tropospheric data are
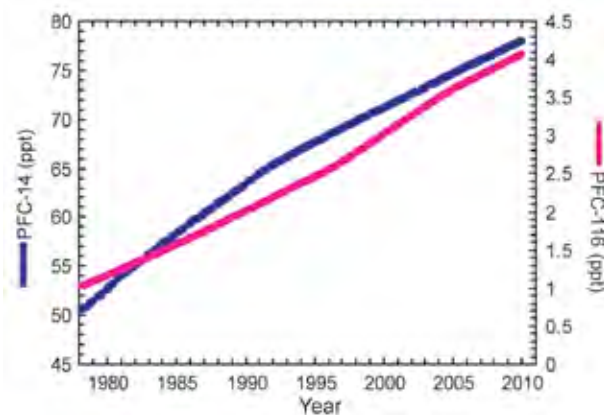
Fig. 2.51. **Global average surface concentrations of PFC-14 and PFC-116 (ppt) from the AGAGE network (Mühle et al. 2010).**

weighted to be relevant for considering Antarctic changes; the ODGI-Antarctica was 82.6 in 2010.

(iv) Perfluorocarbons—J. Mühle and A. L. Ganesan

Perfluorocarbons (PFCs) are extremely long-lived, potent greenhouse gases. PFC-14 (CF_4) and PFC-116 (C_2F_6) have conservative lower limits for atmospheric lifetimes of 50 000 and 10 000 years, respectively, and global warming potentials (100-year time horizon) of 7390 and 12 200, respectively (Ravishankara et al. 1993; Morris et al. 1995; Forster et al. 2007; Montzka et al. 2011). Anthropogenic PFC-14 and PFC-116 were historically emitted as by-products of aluminum production and are now also emitted from the electronics industry. However, the onset and extent of PFC emissions from the electronics industry is poorly known due to limited reporting (Khalil et al. 2003; Worton et al. 2007; EDGAR 2009; Mühle et al. 2010).

A small natural source of PFC-14 from degassing of Earth's crust has been identified (Harnisch and Eisenhauer 1998; Harnisch et al. 2000), which, because of its extraordinarily long atmospheric lifetime, accounts for its significant pre-industrial abundance (Harnisch et al. 1996a, 1996b) of 34.7 ± 0.2 ppt (Mühle et al. 2010), or ~44% of its 2010 abundance.

Global average surface concentrations of PFC-14 and PFC-116, respectively (Fig. 2.51), were 50.8 ± 0.8 ppt and 1.0 ± 0.1 ppt in 1978, 77.7 ± 0.1 ppt and 4.01 ± 0.01 ppt in 2009, and 78.3 ± 0.1 ppt and 4.09 ± 0.02 ppt in 2010 (Mühle et al. 2010). PFC-14 rose at ~1.1 ppt yr^{-1} from the late 1970s to the early 1990s and by ~0.7 ppt yr^{-1} since that time. PFC-116 rose at ~0.09 ppt yr^{-1} from the late-1970s to the mid-1990s followed by an increase to ~0.12 ppt yr^{-1} until the mid-2000s and a subsequent decline to ~0.09 ppt yr^{-1} afterwards (Mühle et al. 2010).

Table 2.5. Mixing ratios, radiative efficiencies and lifetimes of chemicals considered in the AGGI (CO_2 mixing ratios in ppm, N_2O and CH_4 in ppb, all others in ppt).

Industrial Designation or Common Name	Chemical Formula	AGGI	ODGI	Radiative Efficiency (W m^{-2} ppb^{-1})[a]	Mean suface mixing ratio mid-2010 [change from prior year][b]	Lifetime (years)
Carbon Dioxide	CO_2	Y	N	1.41×10^{-5}	388.5[2.2]	
Methane	CH_4	Y	N	3.7×10^{-4}	1799.2[5.0][c]	~9
Nitrous oxide	N_2O	Y	N	3.03×10^{-3}	323.2[0.9]	114[d]
Chlorofluorocarbons						
CFC-11	CCl_3F	Y	Y	0.25	241.0[-2.2]	45
CFC-12	CCl_2F_2	Y	Y	0.32	530.5[-2.5]	100
CFC-113	CCl_2FCClF_2	Y	Y	0.30	75.4[-0.5]	85
Hydrochlorofluorocarbons						
HCFC-22	$CHClF_2$	Y	Y	0.20	204.0[7.3]	11.9
HCFC-141b	CH_3CCl_2F	Y	Y	0.14	20.4[0.6]	9.2
HCFC-142b	CH_3CClF_2	Y	Y	0.20	20.1[0.7]	17.2
Hydrofluorocarbons						
HFC-134a	CH_2FCF_3	Y	N	0.16	57.2[5.0]	13.4
HFC-152a	CH_3CHF_2	Y	N	0.09	6.0[0.2]	1.5
HFC-143a	CH_3CF_3	Y	N	0.13	10.1[1.1][c]	47.1
HFC-125	CHF_2CF_3	Y	N	0.23	8.3[1.0][c]	28.2
HFC-23	CHF_3	Y	N	0.19	23.3[0.7][c]	222
Chlorocarbons						
Methyl Chloroform	CH_3CCl_3	Y	Y	0.06	7.6[-1.5]	5.0
Carbon Tetrachloride	CCl_4	Y	Y	0.13	88.5[-1.0]	26
Methyl Chloride	CH_3Cl	N	Y	0.01	536[-3]	1.0
Bromocarbons						
Methyl Bromide	CH_3Br	N	Y	0.01	7.1[0.0]	0.8
Halon 1211	$CBrClF_2$	Y	Y	0.30	3.9[-0.06]	16.0
Halon 1301	$CBrF_3$	Y	Y	0.32	3.1[0.02]	65
Halon 2402	$CBrF_2CBrF$	Y	Y	0.33	0.46[-0.01]	20
Fully fluorinated species						
Sulfur Hexafluoride	SF_6	Y	N	0.52	7.02[0.28]	3,200
PFC-14	CF_4	N	N	0.10	78.3[0.6]	> 50 000
PFC-116	C_2F_6	N	N	0.26	4.09[0.08]	> 10 000

[a] Radiative efficiencies and lifetimes are taken from Daniel et al. (2007), Montzka et al. (2011), and Prinn et al. (2005).

[b] Mixing ratios are global surface means determined from the NOAA global cooperative sampling network (Hofmann et al. 2006), except for PFC-14 and PFC-116, and HFC-23 in 2009 which were measured by the AGAGE group (Mühle et al. 2010; Miller et al. 2010). Changes indicated in brackets are simply the difference between the 2010 and 2009 annual global surface mean mixing ratios. Units are ppm for CO_2, ppb for CH_4 and N_2O, and ppt for all others.

[c] Preliminary estimate for 2010.

[d] Perturbation lifetime

(v) The combined influence of long-lived trace gases on the radiative balance of the atmosphere —B. D. Hall, J. Butler, and S. A. Montzka

Long-lived trace gases have direct and indirect influences on the energy balance of the atmosphere. The direct radiative forcing (RF) of a trace gas is proportional to its change in atmospheric abundance since the start of the Industrial Revolution around 1750 and how efficiently it absorbs available infrared radiation (its radiative efficiency; Table 2.5). The NOAA Annual Greenhouse Gas Index (AGGI) was developed based upon the direct RF from long-lived trace gases (Hofmann et al. 2006). It represents the RF due to these trace gases in a given year relative to 1990, the Kyoto Protocol baseline year. Indirect effects (e.g., arising from stratospheric ozone depletion or water vapor feedbacks) are not considered in this index. The index is derived from global, surface measurements of carbon dioxide (CO_2), methane (CH_4), nitrous oxide (N_2O), chlorofluorocarbons CFC-12 and CFC-11 (the major long-lived greenhouse gases), and 15 minor greenhouse gases (e.g., HCFCs, HFCs; see Table 2.5). The AGGI offers a relatively straightforward way to assess the increase in direct RF due to long-lived trace gases since 1990.

By mid-2010, the increases in the abundances of these gases over their preindustrial values amounted to a direct RF to the atmosphere totaling approximately 2.80 W m^{-2} (Fig. 2.52). This compares with 2.17 W m^{-2} in 1990. With the AGGI defined as 1.0 in 1990, the preliminary value of the AGGI in 2010 was 1.29. Thus, the accumulation of long-lived trace gases in the atmosphere since 1990 has resulted in a 29% increase in RF due to long-lived gases. The di-
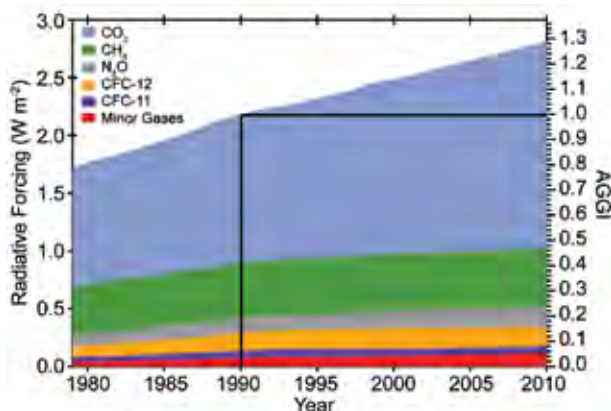
Fig. 2.52. Direct radiative forcing (W m^{-2}) due to long-lived trace gases relative to 1750 (left axis) and the total radiative forcing from long-lived trace gases, relative to 1990, defined as the Annual Greenhouse Gas Index (AGGI; right axis). The value of the AGGI was 1.29 in 2010, an increase of 29% since 1990.
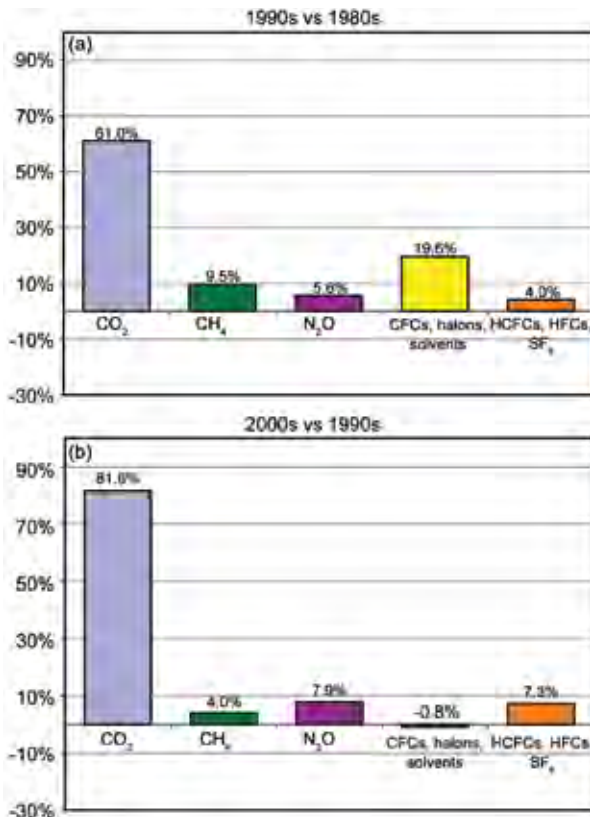
Fig. 2.53. Average relative contributions to changes in direct radiative forcing due to various trace gases through three decades. For example, comparing decadal averages, changes in CO$_2$ are responsible for 61% of the change in radiative forcing between the 1980s and 1990s.

rect RF increased by about 0.043 W m^{-2} each year in the 1980s and by about 0.031 W m^{-2} in the 1990s and 2000s. Currently, carbon dioxide accounts for about 64% of the RF due to long-lived trace gases (Fig. 2.52).

While an increase in the abundance in CO_2 is responsible for the majority of the increase in RF, the relative contributions of CO_2 and other trace gases to increases in RF have changed over time. Nitrous oxide has recently overtaken CFC-12 as the third most important long-lived trace gas contributing to RF (Forster et al. 2007). Chlorofluorocarbons (CFCs) and other ozone-depleting substances played a larger role in the relative changes in the 1980s and 1990s (Fig. 2.53). Through the dual benefits of the Montreal Protocol on Substances that Deplete the Ozone Layer (Velders et al. 2007), the relative contribution of CFCs, halons, carbon tetrachloride (CCl_4), and methyl chloroform (CH_3CCl_3) to changes in RF has decreased in the last decade, partially offseting increases due to other gases.

2) AEROSOLS—A. Benedetti, J. W. Kaiser, and J.-J. Morcrette

The importance of atmospheric aerosols with respect to climate has long been recognized and highlighted in scientific studies (Haywood and Boucher 2000; Kaufman et al. 2002; Yu et al. 2006). Aerosols are often cited as one of the most uncertain factors influencing climate (Solomon et al. 2007), due to both their direct radiative effects and their indirect radiative effects linked to cloud feedbacks. Absorbing aerosols such as black carbon can have a net warming effect, while reflecting aerosols have a cooling impact that can partially offset the warming induced by greenhouse gases.

Aerosol abundance and distributions are influenced by many factors including land cover, surface winds, volcanic activity, biomass burning, and other human activities, and remain a major source of uncertainty in modeling. Progress in aerosol physical parameterizations has improved models, while advances in observing techniques from satellite, aircraft, and ground-based sensors have made it possible to better describe and understand aerosol properties. However, to obtain a more integrated view of the aerosol distribution, and to be able to understand aerosol climatic impacts, it is necessary to integrate the information from models and observations into a common framework. Reanalyses can provide this framework and offer some insight into changes in key climate variables.

ECMWF's operational numerical weather prediction model has recently been extended to include prognostic aerosols and related sources, sinks, and physical processes, underpinned by 4DVAR assimilation of observations of Aerosol Optical Depth (AOD) at 550 nm from the MODIS sensor (Benedetti et al. 2009; Morcrette et al. 2009). Results from an initial aerosol reanalysis were obtained as part of the GEMS (Global and regional Earth-system Monitoring using Satellite and in situ data) project (Hollingsworth et al. 2008) and presented in last year's *State of the Climate* report (Kaiser et al. 2010a). The follow-on project, Monitoring Atmospheric Composition and Climate (MACC) is currently providing an improved aerosol reanalysis for use in climate evaluation and assessment (Simmons 2010). The MACC reanalysis system uses upgraded inventories of biomass burning emissions (GFED V3; van der Werf et al. 2010), an updated aerosol model with improved organic matter modeling and revised dust source, and

a global adaptive bias correction for MODIS aerosol data in the assimilation. These major changes have resulted in a new set of reanalysis data, and highlighted the need for continuous development and research in this area in order to establish high-quality long-term climatologies for aerosols. In parallel to the reanalysis, MACC also runs a Near Real Time Analysis/Forecast (NRTA/F) suite. The model versions used in the NRTA/F and in the reanalysis system are based on the same meteorological cycle with identical dynamical cores and physical processes. However, differences exist in the treatment of the bias correction of the MODIS data and in the definition of the observation error. Moreover the resolution of the initial-guess forecast is higher than in the reanalysis fields. Despite these differences, the spatial patterns of the AOD distribution and their variations with respect to the multiyear average can be attributed to changes in atmospheric state rather than to model changes. The MACC reanalysis will eventually cover the period 2003–11, and will then provide a consistent dataset for a possible trend analysis. Here we compare the global aerosol distribution for 2010 produced by the MACC NRTA/F system with the MACC reanalysis data for years 2003–06.

Figure 2.54 shows the daily mean AOD at 550 nm for 2010 derived from the NRTA/F run for the different species. Dust aerosols show a fairly regular annual cycle with a maximum in the boreal summer. In 2010, the boreal spring peak is also quite pronounced. The annual cycle of sulfate shows consistent boreal spring/summer maxima. Biomass burning aerosols (organic matter and black carbon) peak around September–October, consistently with the seasonality of wildfires in South America and southwestern Africa. Note also the high values of biomass burning AOD starting in August, related to the Russian/Siberian fires. Sea salt AOD does not show a seasonal dependence.

Maps of average AOD for the years 2003–06 (reanalysis) and 2010 (NRTA/F) are shown along with the absolute difference between the two (Fig.
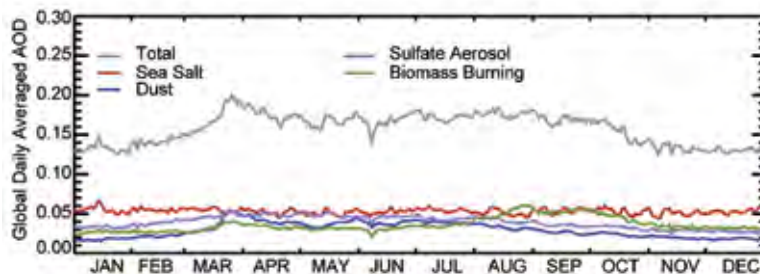
FIG. 2.54. Daily means of globally-averaged forecast aerosol optical depth (AOD) at 550 nm for 2010.
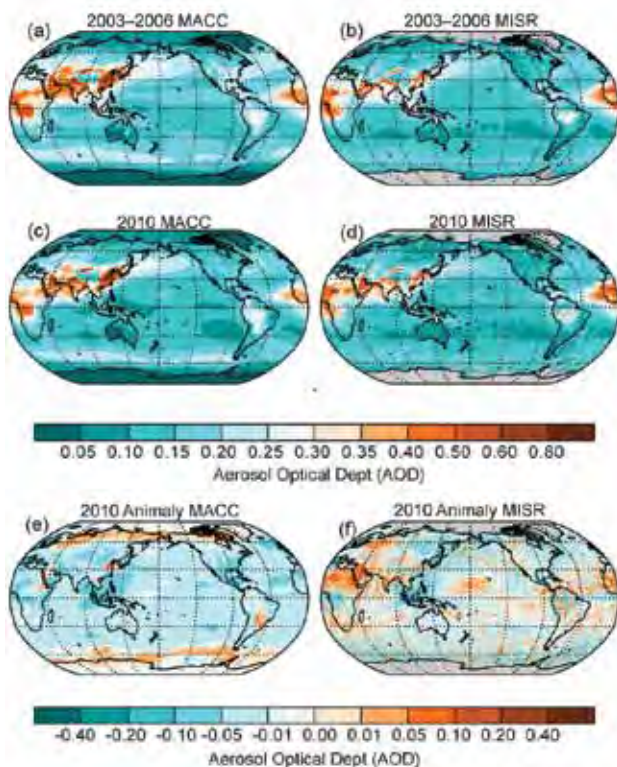
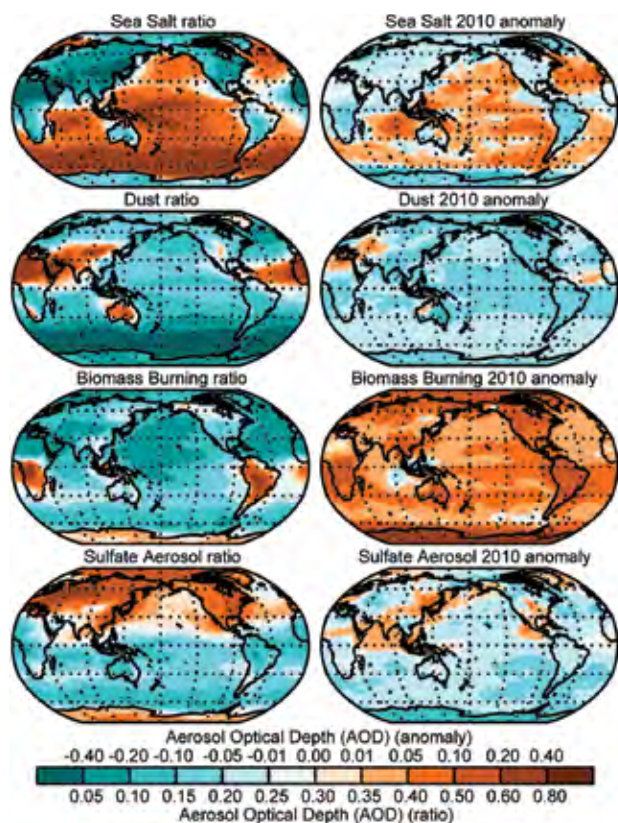**FIG. 2.55. Total aerosol optical depth (AOD) at 550 nm for (top) 2003–06, (middle) 2010, and (bottom) absolute difference between 2010 and the multiyear average. Left panels are derived from MACC data and right panels are from MISR data. (Courtesy of Goddard Earth Sciences Data and Information Services Center, through the GIOVANNI interface; see Table 2.1.)**

FIG. 2.56. 2010 fractional contributions of sea salt, dust, biomass burning, and sulfate aerosols, respectively from top to bottom, defined as the ratio between the aerosol optical depth (AOD) due to a given species and the total AOD (left). Right panels show the differences between the single-species fractional contributions for 2010 and for the 2003–06 base period.

2.55). A general decrease in total AOD is evident, although some areas show an increase in AOD: the high latitudes in the Northern Hemisphere, where the increase can be attributed to the Alaskan fires in spring/early summer and the Russian/Siberian fires in summer; South America, due to the particularly lively biomass burning fall season; and eastern China, most likely due to high values of sulfate aerosols. A decrease in AOD is seen over Indonesia, consistent with a lower-than-average burning season, as also indicated from satellite observations of fire radiative power (section 2g3). This is also confirmed by independent AOD observations from the Multi-angle Imaging SpectroRadiometer (MISR; Kahn et al. 2010), shown in Fig. 2.55. Discrepancies between MISR and the MACC datasets are evident over the Sahara Desert where no data are assimilated and the MACC systems have too little dust. All other regions show good agreement with the reanalysis and NRTA/F systems.

Figure 2.56 shows fractional contributions to the total AOD at 550 nm from the different modeled aerosol species. Sea salt aerosols are the largest con-

tributors in the Southern Ocean and along the storm tracks. The Sahara, with its outflow over the Atlantic, and the Middle East are the areas with the largest contribution from dust to the total AOD. Biomass burning aerosols are dominant over the Amazon, southern Africa, over boreal forests, and over the Southern Hemisphere high latitudes (although total AOD is low at southern latitudes). The maxima in fractional contribution of sulfate aerosols reflect the anthropogenic emission inventory used in the model, with sources in North America, Europe, India, and China. Note the large contribution from sulfate over the Arctic. Differences in single-species fractional contributions between 2010 and the multiyear average (right panels of Fig. 2.56) highlight an increase in sea salt contribution over the tropical oceans. Increased sea salt fractional contribution is also evident around the storm tracks in both hemispheres. The fractional contribution of desert dust for 2010 is lower than the multiyear average everywhere except in the Middle
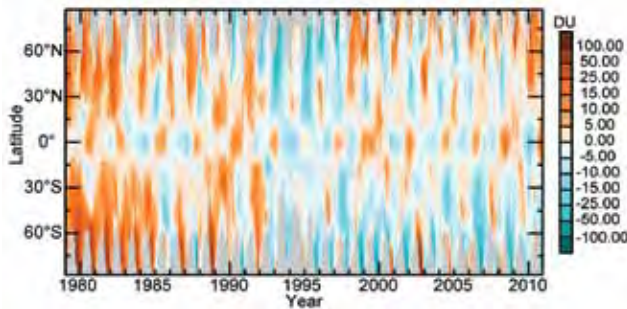
FIG. 2.57. Time variation (1979–2010) of total ozone anomalies. Anomalies are based on the **SBUV/TOMS/OMI MOD V8** merged data record (1978–96; Frith et al. 2004) and **GOME1/SCIAMACHY/GOME2 (GSG)** merged total ozone (mainly GOME2 data in 2010; Weber et al. 2007). Anomalies were calculated from area weighted monthly mean zonal mean data in 5° latitude steps after removing the seasonal mean from the base period 1980–2008, which was derived from the **MSR** analysis (Van der A et al. 2010). Possible corrections from the overlap period (1996–2009) with **MOD V8** were not applied to the **GSG** data set. Grey areas indicate regions where data are unavailable.

East region. Biomass burning aerosol fractional contribution to total AOD is substantially larger in 2010 nearly everywhere, while sulfate shows regional increases in already-polluted areas.

> 3) STRATOSPHERIC OZONE—M. Weber, W. Steinbrecht, R. J. van der A, P. K. Barthia, V. E. Fioletov, R. McPeters, and R. S. Stolarskl

The 2010 annual mean ozone anomaly was positive for most of the Northern Hemisphere, with values of up to 40 DU above the 1980–2008 mean (Plate 2.1l). Similar high positive anomalies were observed in the late 1990s, but more frequently in the 1980s (Fig. 2.57). Above Central Europe, the annual mean was the highest of the last 25 years (Steinbrecht et al. 2011). This is also true for the midlatitude zonal mean (30°N–60°N; Fig. 2.58). The Arctic stratosphere in spring was characterized by very high ozone anomalies exceeding 100 DU in the Eurasian sector in February. The positive anomaly in the Northern Hemisphere persisted throughout the year.

In the tropics, annual mean ozone was close to the long-term mean. During the first half of 2010, ozone anomalies were quite negative (below -15 DU) and changed to positive in the second half (above +15 DU). This is largely attributed to the switch from the easterly phase of the quasi-biennial oscillation (QBO) to the westerly phase (Fig. 2.57; Baldwin et al. 2001). In the Southern Hemisphere, annual ozone was close to the long-term mean at midlatitudes and negative in

the polar region. The depleted polar ozone reflected a deeper than average ozone hole during Antarctic spring (see section 6g). From Fig. 2.57, it is evident that the QBO modulates extratropical and polar ozone as well.

Long-term trends in total ozone (Fig. 2.58) are confined to the extratropics. The midlatitude losses between 1980 and the early 1990s were followed by stable values in the Southern Hemisphere and in-
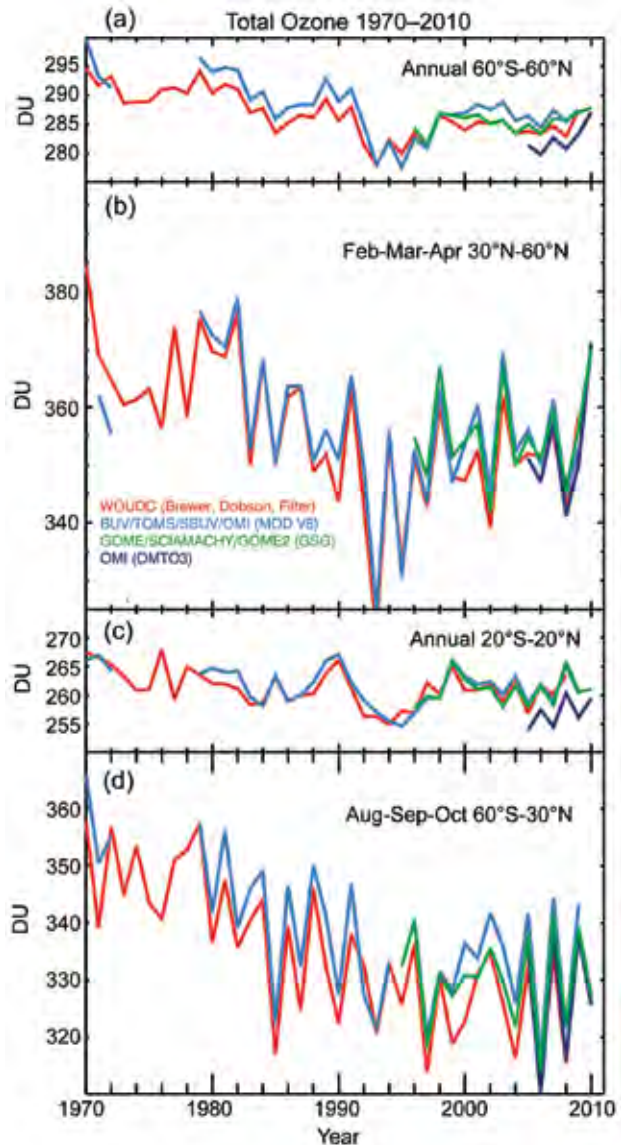
FIG. 2.58. Annual mean total ozone time series of ground-based measurements combining Brewer, Dobson, and filter spectrometer data (red; Fioletov et al. 2002), merged BUV/SBUV/TOMS/OMI MOD V8 (blue; Frith et al. 2004), GOME1/SCIAMACHY/GOME2 GSG (green; Weber et al. 2007), and OMI OMTO3 (OMI-TOMS; Kroon et al. 2008; McPeters et al. 2008) satellite data in the (a) 60°S–60°N, (b) 30°N–60°N, (c) 20°S–20°N, and (d) 30°S–60°S zonal bands.

creases in the Northern Hemisphere. The substantial minimum in the Northern Hemisphere in the early 1990s arose from additional ozone loss associated with the Mount Pinatubo volcanic eruption and a series of unusually cold Arctic winters with reduced ozone transport and enhanced polar ozone loss (e.g., Dhomse et al. 2006). Total ozone is expected to recover because stratospheric halogens leveled off in the late 1990s and are now declining (see Fig. 2.50 and section 2f1iii). However, other factors like the 11-year solar cycle and, in particular, changes in stratospheric circulation patterns [i.e., Brewer-Dobson circulation, teleconnection patterns such as the North Atlantic Oscillation (NAO), and annular modes of internal variability such as the Arctic Oscillation (AO)] contribute to variations on interannual to decadal time scales (Appenzeller et al. 2001; Steinbrecht et al. 2001; Weber et al. 2003; Orsolini et al. 2004; Yang et al. 2005; Dhomse et al. 2006; Stolarski and Frith 2006; Vyushin et al. 2007; Harris et al. 2008).

FIG. 2.59. Top: Jan–Mar (JFM) total ozone area weighted between 45°N and 60°N as measured from ground (Fioletov et al. 2002) and satellites, SBUV/TOMS/OMI MOD V8 data in red, GOME/SCIAMACHY/GOME2 GSG merged data in blue, and OMI OMTO3/OMI-TOMS (Kroon et al. 2008; McPeters et al. 2008) in light brown. The thick black line is the three point triangular smooth of the ground data. Middle panel: Dec–Feb (DJF) Arctic Oscillation (AO) index (blue values correspond to positive AO values). Thick black line is the three point triangular smooth of the AO index. Bottom panel: Equivalent effective stratospheric chlorine (EESC; Newman et al. 2007) drawn with a reversed y-axis.

The very high 2010 total ozone anomaly poleward of about 30°N coincided with an unusually pronounced negative phase of the AO, starting in December 2009 and lasting throughout most of 2010 (Steinbrecht et al. 2011). Winters with large negative AO indices are characterized by the enhancement and deflection of planetary waves towards the polar region. This is associated with an enhanced Brewer-Dobson circulation that transports more ozone into the extratropics, weakens the polar vortex, and reduces polar ozone loss (Hartmann et al. 2000; Randel et al. 2002; Weber et al. 2003). The easterly QBO phase during the first half of 2010 further strengthened the deflection of planetary waves (Baldwin et al. 2001). Winter/spring ozone anomalies in the Northern Hemisphere usually weaken due to photochemical decay, but persist until the end of the following fall (Fioletov and Shepherd 2003); in 2010 this resulted in very high 2010 annual mean ozone in the Northern Hemisphere (Steinbrecht et al. 2011).

Figure 2.59 highlights the long-term evolution of the winter AO, stratospheric halogen load (Equivalent Effective Stratospheric Chlorine, EESC), and northern midlatitude ozone in January–March (JFM) over the last 40 years. Apart from the year-to-year variability, the AO state changed from negative to a positive state in the late 1980s and since then has trended back to negative values. Decadal changes in stratospheric circulation as expressed by the AO appear to go hand in hand with chemical changes (EESC). As the AO is a leading mode of Northern Hemispheric climate variability and couples the stratosphere and troposphere (Thompson and Wallace 2000; Hartmann et al. 2000), stratospheric ozone changes may have contributed on long time scales to changes in the global circulation and climate (Steinbrecht et al. 2011). When attributing different factors to long-term changes in ozone, it is, however, difficult to separate dynamical and chemical contributions (Kiesewetter et al. 2010).

g. Land surface properties

1) ALPINE GLACIERS AND ICE SHEETS—M. S. Pelto

The World Glacier Monitoring Service (WGMS) record of mass balance and terminus behavior (WGMS 2008; WGMS 2009) provides a global index for alpine glacier behavior. Mass balance was negative in 2009 for the 19th consecutive year. Preliminary data for 2010 from Austria, Greenland, Italy, Norway, New Zealand, and the United States indicate it is highly likely that 2010 will be the 20th consecutive year of negative annual balances.

Alpine glaciers have been studied as sensitive

indicators of climate for more than a century, most commonly focusing on changes in terminus position and mass balance (Oerlemans 1994). The worldwide retreat of mountain glaciers is one of the clearest signals of ongoing climate change (Haeberli et al. 2000). The retreat is a reflection of strongly negative mass balances over the last 30 years (WGMS 2008). Glacier mass balance is the difference between accumulation and ablation. A glacier with a sustained negative balance is out of equilibrium and will retreat. The recent rapid retreat has led to some glaciers disappearing (Pelto 2010).

The cumulative mass balance loss of the last 30 years is 12.3 m w.e., the equivalent of cutting a 14 m thick slice off the top of the average glacier (Fig. 2.60). The trend is remarkably consistent from region to region (WGMS 2009). WGMS mass balance results based on 30 reference glaciers with 30 years of record are not appreciably different from the results for all reporting glaciers. The decadal mean annual mass balance was -198 mm in the 1980s, -382 mm in the 1990s, and -654 mm for 2000–09. The declining mass balance trend during a period of retreat indicates alpine glaciers are not approaching equilibrium and retreat will continue to be the dominant terminus response.

In 2010 winter accumulation on Austrian and Italian glaciers was about average, and summer temperature was above the mean in 2010. The result was mass losses on glaciers in the Alps: Sonnblickkees, Austria, -790 mm; Ciardoney, Italy, -830 mm; and Fontana Bianca, Italy, -130 mm. The Swiss Glacier Monitoring Network reported that in 2010 the termini of 86 glaciers were in retreat, six were stationary, and three advanced.

In Norway, terminus fluctuation data from 30 glaciers for 2010 indicate 27 retreating, one stable, and two advancing. The average terminus change was -17 m, compared to -183 m in 2009. Mass balance surveys found deficits on all Norwegian glaciers. Winter 2009/10 was cold but with little snow on the glaciers, 50%–80% of the long-term normal. Summer was warmer than normal in the south and a bit colder than normal in the north. (L. Andreasson 2011, personal communication).

In the North Cascades, Washington (M. Pelto 2011, personal communication), a transition from El Niño to La Niña conditions led to equilibrium mass balances. El Niño winter conditions led to reduced winter snowfall. La Niña conditions developed by summer causing low summer melting, which offset
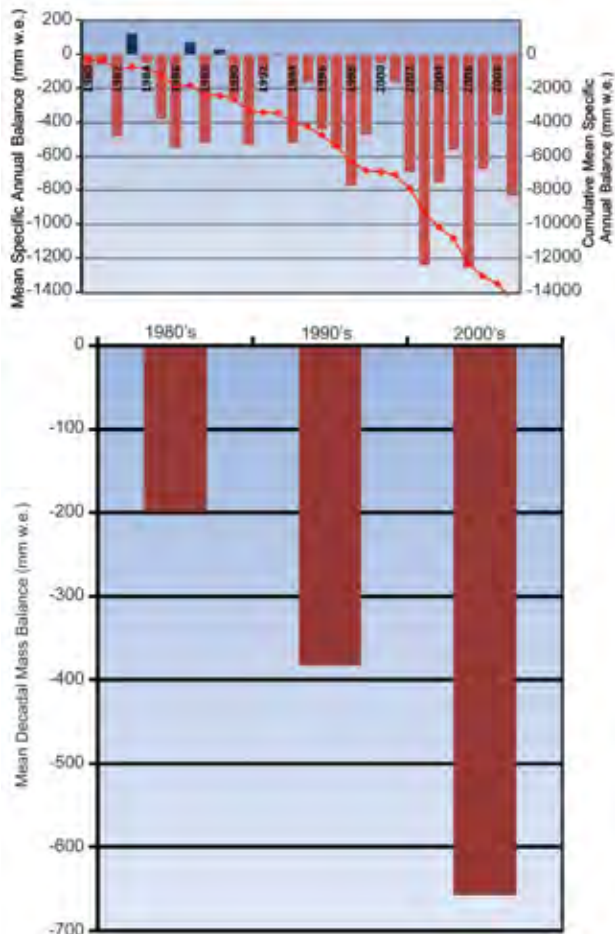
FIG. 2.60. The (top) annual mean and cumulative annual mean balance and (bottom) decadal mean cumulative specific mass balance (mm w.e.) reported for the 30 reference glaciers to the WGMS.

the low accumulation. The result was positive annual balance on four glaciers, negative balance on five glaciers, and an equilibrium balance on one glacier. All 33 glaciers observed retreated in 2010. In southeast Alaska, snowlines were 50 m above average on Lemon Creek and Taku Glacier of the Juneau Icefield indicative of moderate negative balances.

In New Zealand, El Niño led to normal to below-normal temperatures through summer and into fall 2010, leading to snowlines in a near steady state (J. Hendrikx 2011, personal communication). On 50 glaciers surveyed, the average snowline was at the equilibrium snowline elevation, after two strongly negative years in 2008 and 2009.

For information on 2010 ice melt on the Greenland ice sheet and in Antarctica please refer to sections 5f and 6e, respectively.

Stratospheric water vapor modulates Earth's climate, directly through long-wave radiative processes, and indirectly through its influence on stratospheric ozone abundance (Shindell 2001). An increase (decrease) radiatively warms (cools) the troposphere and cools (warms) the stratosphere. Solomon et al. (2010) modeled the radiative forcing of an observed rapid 10% (~0.5 ppmv) post-2000 decrease and found that it slowed the rate of increase in global surface temperature over 2000–09 by about 25% compared to that which would have occurred from well-mixed greenhouse gases. This makes it imperative that stratospheric water vapor be closely monitored.

The main sources of stratospheric water vapor are entry through the tropical tropopause (Brewer 1949) and in situ oxidation of methane (CH_4) and hydrogen (H_2), yielding two water molecules for each CH_4 molecule oxidized (LeTexier et al. 1988). The stratosphere is extremely dry (< 10 ppmv) because water vapor is condensed out as air moves through the extremely cold tropical tropopause region. Other sources include convective overshooting of ice particles and transport across the tropopause into the extratropical lower stratosphere. Both are difficult to globally quantify but are likely minor contributors. The main loss process, polar dehydration during Antarctic winter, annually removes ~2% of the water vapor burden (Douglass and Stanford 1982).

Near-global measurements by satellites began in late 1978 with seven months of Limb Infrared Monitor of the Stratosphere (LIMS) measurements (Gille and Russell 1984) that provided the first insights into the global budget (Jones et al. 1986). Longer-term datasets from satellite-borne instruments have been available since 1984, with the longest records from the Stratospheric Aerosol and Gas Experiment (SAGE II) (1984–2005) and the Halogen Occultation Experiment (HALOE) (1991–2005). The Aura Microwave Limb Souder (MLS), active since 2004, provides a critical extension to HALOE.

Entry into the tropical lower stratosphere varies with the seasonal cycle of temperatures near the tropical tropopause, with minima and maxima during the Northern Hemisphere (NH) winter and summer, respectively (Reed and Vleck 1969). As air enters the stratosphere it is imprinted with a seasonally-dependent water vapor mixing ratio (Fig. 2.61). The seasonality is large, typically 50%–60% of the annual mean. Air masses retain these imprints as they are advected to higher altitudes in the tropics by the Brewer-Dobson circulation (BDC), a phenomenon dubbed "the tropical tape recorder" by Mote et al. (1996). Seasonal signals are gradually eroded through mixing as air moves upward and poleward. Mixing ratios increase with altitude as greater fractions of CH_4 and H_2 are oxidized.

The global distribution and variance are controlled by the seasonal cycle of tropical entry conditions coupled with seasonally-dependent transport by the BDC, with stronger extratropical downwelling during winter. The NH winter downwelling is stronger than in the Southern Hemisphere (SH), and is accompanied by the strongest tropical upwelling with the coldest tropical tropopause. Hence, in January the tropics are extremely dry, especially over the Western Pacific, while the Arctic is significantly moistened by strong downwelling with minimal polar dehydration (Fig. 2.62a). At the lowest stratospheric levels, longitudinal structure reflects the impacts of tropospheric dynamics, while distributions are zonally uniform in the mid- and upper stratosphere. In July (Fig. 2.62b), lower stratospheric mixing ratios over Antarctica are extremely low within the vortex, substantially higher within a zonal band surrounding the vortex, and highest over the Indian subcontinent as the lower stratosphere is moistened by convective uplift within the monsoon. The net result is that the annual mean SH is drier than the NH (Rosenlof et al. 1997).

The determination of multidecadal trends from satellite-based datasets is challenging and uncertain because there are significant discrepancies between coincident measurements by the different sensors (Vömel et al. 2007; Kley et al. 2000; Randel et al. 2004; Lambert et al. 2007). These discrepan-
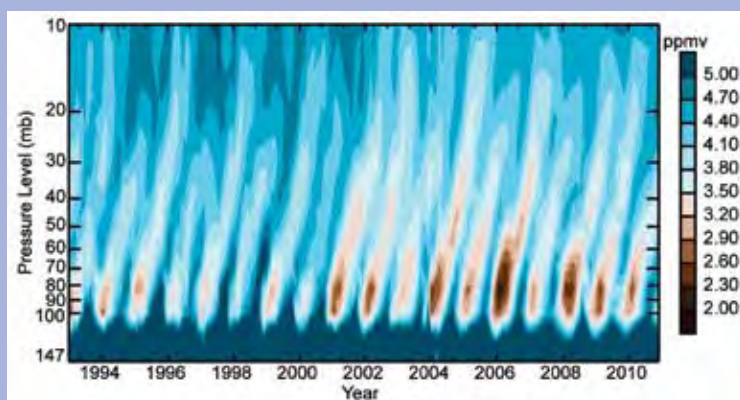
FIG. 2.61. Vertical profiles of tropical (10°N–10°S) stratospheric water vapor mixing ratios from HALOE (1991–2005) and Aura MLS (2004–present). HALOE version 20 mixing ratios were adjusted to better agree with the MLS version 3.3 based on coincident profiles during 2004–05. Adjustments are altitude dependent with a maximum shift of ~0.5 ppmv.
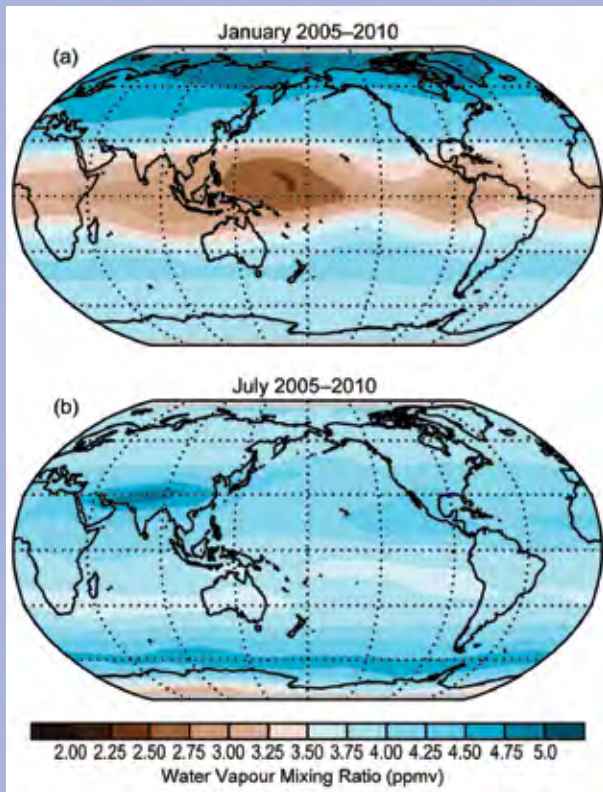
FIG. 2.62. Six-year (2005–10) average global distributions of water vapor at 82 hPa, near the point of stratospheric entry in the tropics, as measured by Aura MLS during (a) January and (b) July, the months of seasonal extremes in water vapor entry mixing ratios.

cies, ranging from 10% to 50% or even greater in some cases, preclude simple compositing to produce longer-term records.

The longest continuous record is in the NH midlatitudes over Boulder, Colorado, (40°N) from balloon-borne frost point hygrometers (FPHs; Fig. 2.63). These data portray net increases over Boulder of 14 ± 2% (0.6 ± 0.1 ppmv) during 1980–2000 (Scherer et al. 2008) and 27 ± 6% (1.0 ± 0.2 ppmv) during 1980–2010 (Hurst et al. 2011). These and other in situ and satellite data in the NH imply a 50% increase in entry-level stratospheric water vapor during 1950–2000 (Rosenlof et al. 2001) while tropopause temperatures decreased (Zhou et al. 2001).

Prominent in both HALOE and NOAA FPH data over Boulder (Fig. 2.63), and in tropical HALOE data (Fig. 2.61), is a ~10% (~0.5 ppmv) decrease after 2000. Randel et al. (2006) attributed this to anomalously cold tropical tropopause temperatures and increased tropical upwelling. Although attribution of this large and rapid decrease supports the idea that tropical tropopause temperatures control stratospheric

water vapor entry (Randel et al. 2004; Fueglistaler and Haynes 2005; Rosenlof and Reid 2008), trends in tropical cold point temperatures cannot explain the long-term increase in the NH midlatitudes. With only ~30% of the observed increase attributable to CH_4 growth (Rohs et al. 2006), the predominant cause(s) remains unidentified. Hurst et al. (2011) noted that water vapor growth over Boulder during 2006–10 strengthened with altitude in the absence of sufficient CH_4 growth, requiring a dominant mechanism other than an increase in water vapor in the tropical lower stratosphere. Identifying the underlying cause(s) of the observed long-term net increase remains elusive despite substantial ongoing efforts.
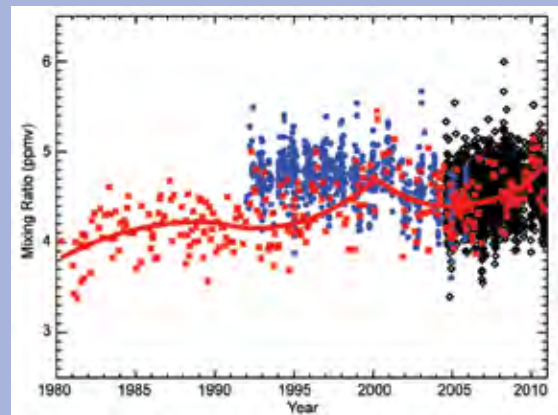
FIG. 2.63. Stratospheric water vapor mixing ratios at 46 hPa over Boulder, Colorado. The NOAA FPH data (red markers) and smooth curves (red) in four discrete trend periods depict a net increase of 27 ± 6% since FPH measurements began in 1980 (Hurst et al. 2011). Data from Aura MLS (black markers) and adjusted data from HALOE (blue markers) are also included. Note the post-2000 decrease in both the FPH and HALOE data, and the post-2006 increase in both the FPH and MLS data.

Balloon launch at Marshall Field Site, Boulder, Colorado
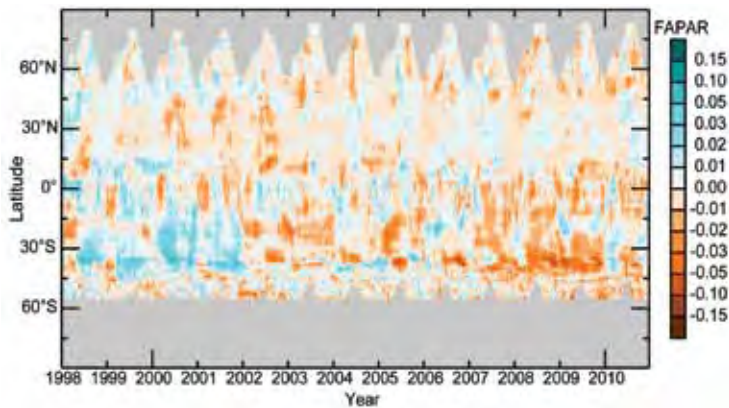
FIG. 2.64. Fraction of Absorbed Photosynthetically Active Radiation (FAPAR) anomalies from the 1998–2010 base period by latitude provided by SeaWiFS (NASA) and MERIS (ESA) sensors. Gray areas indicate regions where data are unavailable.
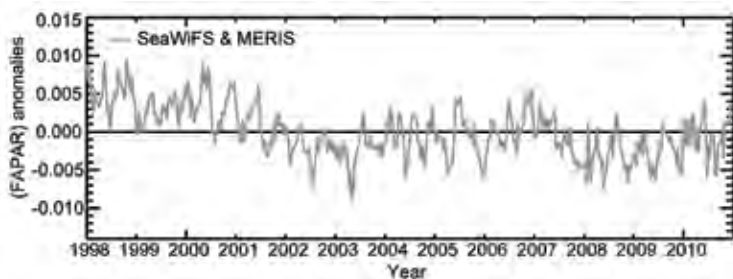
2) FRACTION OF ABSORBED PHOTOSYNTHETICALLY AC-
TIVE RADIATION (FAPAR)—N. Gobron and A. S. Belward

Analysis of a 13-year record of global earth observations has showed considerable variations in vegetation dynamics on regional and continental scales. The state of vegetation has been monitored using estimates of the Fraction of Absorbed Photosynthetically Active Radiation (FAPAR) from 1998 to 2010 (Gobron et al. 2010). These data highlight geographical regions with anomalous vegetation in 2010 with respect to previous years.

In Plate 2.1m, positive anomalies indicate favorable vegetation growing conditions in 2010, while negative values, in brown, imply vegetation stress. The strongest positive anomalies are found in central and eastern Australia, followed by minor positive anomalies over the middle of the United States, India, central Europe, and southern Africa. Strong negative anomalies occurred in Russia and South America.

The situation in Australia contrasts notably with previous years' values and provides quantitative confirmation of the break in the persistent droughts that have affected this region over the last decade. Vegetation activity in 2010 has now returned to levels seen in 2000–01.

FIG. 2.65. Globally averaged Fraction of Absorbed Photosynthetically Active Radiation (FAPAR) anomalies from the 1998–2010 base period.

The most striking negative anomaly occurred in central Russia, where high temperatures and low rainfall have translated into extreme FAPAR negative anomalies. Cropland, grassland, and forests were all affected. In some cases, catastrophic fires occurred, but fire apart, the region as a whole exhibits significantly depressed levels of photosynthetic activity and plant growth. Amazonia was also affected by strong droughts in September 2010 and the effects of this are seen in Plate 2.1m. However, in comparison with previous years and in terms of the annual average, these anomalies are not as strong as in Russia.

Figure 2.64 shows zonally-averaged FAPAR anomalies since 1998. The Southern Hemisphere contrasts markedly with the Northern because of persistent negative anomalies through all seasons from around 2002 up to 2009. This feature ended in 2010, with positive anomalies in the Southern Hemisphere at the beginning and end of the year.

Despite dramatic regional impacts, neither the renewed plant growth vigor in Australia nor the widespread vegetation stress in central Russia were large enough to cause major changes in the global average. When globally averaged (Fig. 2.65), 2010 appears to be part of a gradual return to positive values, though not to the levels seen between 1998 and 2001.

3) BIOMASS BURNING—J. W. Kaiser, A. Heil, and G. R. van
der Werf

Biomass burning occurs in all vegetated terrestrial ecosystems. Humans ignite most fires in the tropics and subtropics, while lightning fires are more common in remote boreal regions. Fires contribute to the buildup of carbon dioxide (CO_2) through deforestation and tropical peatland fires, and from areas that see an increase in the fire frequency. They also emit other greenhouse gases and are a major source of aerosols, carbon monoxide (CO), and oxides of nitrogen (NOx), impacting local and regional air quality. Overall, fires impact 8 out of 13 identified radiative forcing agents (Bowman et al. 2009) and indirectly impact the fluxes of water and energy by modifying vegetation.

Satellite observations of burned area (Giglio et al. 2010) in combination with biogeochemical modeling indicate that carbon emissions from fires were 2.0 Pg

C yr^{-1}, averaged over 1997–2009 (van der Werf et al. 2010; Global Fire Emissions Database, GFED). About a quarter (0.5 Pg C yr^{-1}) is emitted from fires used in the deforestation process or in degraded peatlands and is a net source of CO_2. The remainder is balanced by CO_2 uptake of regrowing vegetation. Deforestation and peat fires in particular show large variability from year to year, partly related to changes in annual deforestation rates and drought conditions in deforestation zones.

In addition to providing updates to GFED, the European Union (EU) Monitoring Atmospheric Composition and Climate (MACC) project assimilates satellite-observed fire radiative power (FRP) to estimate biomass burning trace gases and aerosol emissions (Kaiser et al. 2010b; Global Fire Assimilation System, GFAS). The products are available start-ing in 2003 and are extended in real time. Initial field research (e.g., Wooster et al. 2005) indicated that FRP is universally proportional to biomass consumed. However, a biome dependency has been found and implemented following Heil et al. (2010). The presented GFAS data are based on Moderate Resolution Imaging Spectroradiometer (MODIS) FRP only to ensure consistency of the time series. GFED and GFAS agree within about 25%, as illustrated in Fig. 2.66.

The annual biomass combustion calculated by GFAS for the reference period 2003–09 is shown in Fig. 2.67 and the anomaly for 2010 is shown in Plate 2.1n. The global- and continental-scale budgets are summarized in Table 2.6, alongside GFED emissions, which span a longer timeframe (1997–2009) but cannot be calculated in real time.

Table 2.6. Annual continental-scale biomass burning budgets in terms of burnt carbon (Tg C yr^{-1})							
Dataset		GFED3.1		GFAS1.0			
Time Period		1997–2009		2003–2009		2010	2010 w.r.t. 2003–2009
Quantity		mean	range	mean	range	value	absolute anomaly	relative anomaly
Global		2000	1514–2760	2062	177–2305	1876	-185	-9%
N America	30°N–57°N, 190°E–330°E	62	9–140	98	70–137	106	8	8%
C America	30°N–57°N, 190°E–330°E	43	23–112	67	56–91	53	-14	-21%
SH America	0°–60°S, 190°E–330°E	269	90–570	348	176–456	418	70	20%
Europe and Mediterranean	30°N–75°N, 330°E–60°E	19	8–31	33	30–41	61	28	85%
NH Africa	0°–30°N, 330°E–60°E	478	358–584	425	378–459	332	-94	-22%
SH Africa	0°–35°S, 330°E–60°E	552	478–676	511	485–589	571	60	12%
N Asia	30°N–75°N, 60°E–190°E	148	30–366	214	111–466	105	-110	-51%
SE Asia	10°N–30°N, 60°E–190°E	103	38–170	132	111–161	157	25	19%
Tropical Asia	10°N–10°S, 60°E–190°E	192	21–1065	103	36–217	22	-81	-79%
Australia	10°S–50°S, 60°E–190°E	134	78–185	130	87–175	53	-77	-59%

In 2010, global emissions were 9% below the 2003–09 mean, well within the historic range. The distribution of fire activity, however, was anomalous with more fire activity in Southern Hemisphere (SH) America and Europe, notably European Russia, and less fire activity in Australia, Northern Hemisphere (NH) Africa, Central America, and northern and tropical Asia.

The combustion rate in SH America was 20% above the 2003–09 average, and more than double that of 2009 (Table 2.6; Fig. 2.66). SH America experienced drought conditions during the fire season in the southern Amazon where most fire activity is concentrated in the arc of deforestation. The increase is remarkable because the Brazilian space agency has reported a downward trend in deforestation since 2004 for the Brazilian Amazon (Regalado 2010; http://www.obt.inpe.br/prodes/). Fire data support this trend, except for 2007 and 2010. The Amazon fires in 2010 have been linked to a warm sea surface temperature anomaly of the tropical North Atlantic via the geographical pattern of the accompanying drought, similar to the situation in 2005 (Lewis et al. 2011; Marengo et al. 2008). Both 2007 and 2010 also feature strong transitions from El Niño to La Niña. Finally, part of the increase in 2010 stemmed from fires that were out of control in Bolivia and Peru, while understory fires, maintenance fires, and deforestation fires in areas not covered by the assessment of the Brazilian space agency could have also contributed to the strong fire season.

Western Russia experienced anomalously dry and hot conditions during May to August 2010. They triggered widespread fire activity in an area east of Moscow, where drained organic soils provided ample fuel for prolonged burning of peaty soils. High rates of smoke emissions and atmospheric subsidence led to a severe impact on air quality in July and August 2010. This area is included in Europe in Table 2.6 and
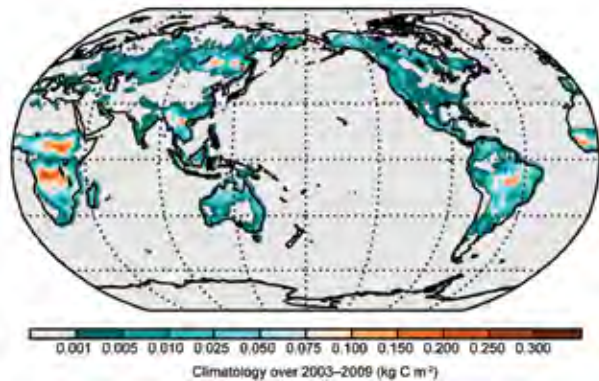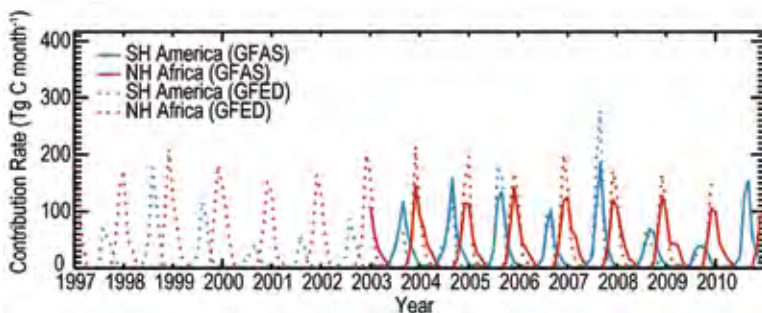

Fig. 2.67. Climatological global biomass burning over the 2003–09 base period as burnt carbon area density (kg C m⁻²).

explains the large positive anomaly; fire activity in Europe excluding Russia was below average.

The low combustion rate in NH Africa with its peak in boreal winter appears to continue a negative trend that is beginning to emerge from the GFED dataset (Fig. 2.66). The negative anomaly in 2010 could also be related to a relatively late fire season, transferring part of the emissions to 2011.

The strongest relationships between the El Niño-Southern Oscillation and fire are usually found in Indonesia and Australia, where El Niño-induced drought in general leads to higher fire activity (vice versa for La Niña), although low rainfall rates in Australia's more arid regions may actually lower fire activity because of reduced fuel availability (van der Werf et al. 2008). In 2010, the transition to La Niña conditions occurred before the fire season started in Indonesia and northern Australia, and anomalous wet conditions strongly inhibited fire rates in both regions (Table 2.6).

The positive aerosol anomaly over SH America and a negative one over Indonesia reported in section 2f2 (Fig. 2.56) is likely to be explained by the fire anomalies reported here.

4) FOREST BIOMASS AND BIOMASS CHANGE—P. Cais, S. Quegan, and S. Saatchi

Biomass stored in forests is a major global carbon stock whose dynamics affect climate both through emissions when forest is cleared or degraded and by taking up carbon dioxide (CO_2) when forest is growing. Key sources of information on global biomass and its change in each country are the periodic Global Forest Resource Assessment (FRA) reports of the Food and Agriculture

Fig. 2.66. Monthly carbon combustion rate (kg C mo⁻¹) in Northern Hemisphere Africa (red) and Southern Hemisphere America (blue) by GFED (dashed line) and GFAS (solid line).

Organization (FAO 2006, 2010), which are typically based on inventory data. The uncertainties in the country data are not reported and are likely to be highly variable, particularly for countries without a well-developed forest monitoring infrastructure (as is the case in many tropical forest countries). Individual plot data are not distributed, but the data underlying the individual country estimates in the FRA can be accessed through FAO. Revisit of inventories allows measurement of biomass changes over periods of several years.

The key findings of FAO (2010) are: (1) that the global forest area extent is 40 M km^2, storing a total biomass of 290 Pg C; (2) that the rate of tropical deforestation since 2000, 0.13 M km^2 yr^{-1}, seems to have decreased compared to the 1990s rate of 0.16 M km^2 yr^{-1}; Brazil and Indonesia, which had the highest forest loss rates in 1990s, have reduced deforestation in the 2000s; and (3) that large-scale forest plantation partly counterbalances tropical forest loss. Biomass stocks are decreasing in tropical countries because of deforestation, but increasing in temperate countries due to forest growth, and increased forest stand density in Europe and in the United States. China also has a major reforestation program. Forest in European Russia seems to be gaining carbon, but this is counterbalanced in Asian Russia by increased fire disturbance losses (Shvidenko et al. 2010).

Carbon dioxide emissions from land use change (LUC; mainly tropical deforestation) were revised to 2009 by Friedlingstein et al. (2010) using data on forest cover reported by FAO (2010) incorporated in a LUC emission model (Houghton 2003). The average LUC emissions estimate for the period 2000–09 is 1.1 ± 0.7 Pg C yr^{-1}, which is lower than the previous estimate of 1.5 ± 0.7 Pg C yr^{-1} with the same LUC emission model when driven by data from FAO (2006), mainly because of replacement of the originally anticipated rates of deforestation in tropical Asia by actual values. The downward revision of LUC emissions to 2009 by Friedlingstein et al. (2010) is also consistent with satellite observations over the Brazilian Amazon indicating a slowdown of deforestation in that region (Regalado 2010). There are two major sources of uncertainty in these estimates: the area of forest lost and the average biomass of this forest. Differences in the assumed value of the average biomass gave rise to differences of 1 Pg C yr^{-1} in the range of estimates of emissions from tropical deforestation (Houghton 2005). Satellite estimates of deforestation also tend to be significantly lower than inventory-based estimates (Achard et al. 2004; DeFries et al. 2002). A recent benchmark map developed from ground and satellite observations provides spatially refined and methodologically comparable carbon stock estimates for forests across 75 developing countries in tropical regions (Fig. 2.68). The map improves upon previous assessments based on often old and incomplete national forest inventory data and earlier spatial products. With systematic quantification of the errors, the map improves and constrains the pantropical estimate of total tropical forest biomass carbon (247 Gt C at 10% tree cover), and similarly national-scale carbon stocks (Saatchi et al. 2011). With the uncertainties quantified spatially along with biomass values, estimates of emission from tropical forests can improve significantly.
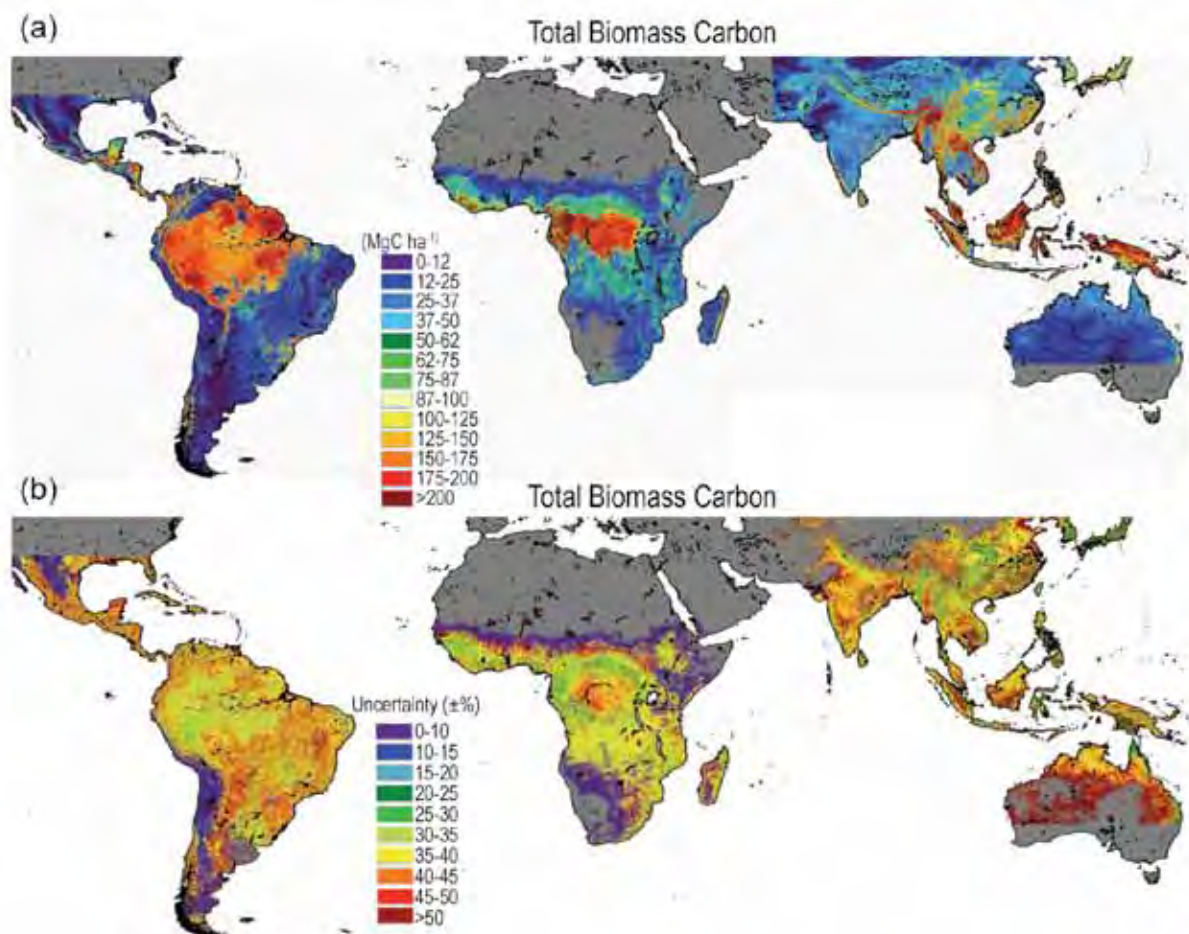
Fig. 2.68. Benchmark map of magnitude and uncertainty of forest carbon stock in tropical regions. (a) Forest carbon stock defined as 50% of **AGB+BGB** is mapped at 1-km pixel resolution and colored based on 12 Mg C ha^{-1}–25 Mg C ha^{-1} range to show the spatial patterns. (b) The uncertainty of the benchmark map is estimated using error propagation through spatial modeling approach. The uncertainty is given in terms ±% and it includes all errors associated with prediction from spatial modeling, sampling errors associated with variability of forest AGB at 1-km grids, estimation of Lorey's height from **ICESAT GLAS** Lidar used to sample the forest structure over all tropical forests, estimation of AGB from Lorey's height using inventory data from 493 plots distributed over three continents, and errors associated with **BGB** estimation from allometry relating **AGB** and **BGB** (Saatchi et al. 2011).